國立交通大學

電子工程學系電子研究所

博士論文

一種新穎自行開發之快速精準量子模擬器用於三維度高應力下矽電洞能帶結構及反置層遷移率之研究

A New In-House Fast Sophisticated Quantum Simulator for Silicon Hole Band Structure and Inversion-Layer Mobility under Three-Dimensional GPa-Level Stresses

研究生：　李建志

指導教授：　陳明哲 博士

中華民國 一○一年 十一 月

一種新穎自行開發之快速精準量子模擬器用於三維度高應力下矽電洞能帶結構及反置層遷移率之研究

A New In-House Fast Sophisticated Quantum Simulator for Silicon Hole Band Structure and Inversion-Layer Mobility under Three-Dimensional GPa-Level Stresses

研 究 生: 李建志　Chien-Chih Lee

指導教授: 陳明哲 博士　Dr. Ming-Jer Chen

國立交通大學
電子工程學系 電子研究所
博士論文

A Dissertation
Submitted to Department of Electronics Engineering &
Institute of Electronics
College of Electrical and Computer Engineering
National Chiao Tung University
in Partial Fulfillment of the Requirements
for the Degree of Doctor of Philosophy
in
Electronics Engineering
November 2012
Hsinchu, Taiwan, Republic of China

中華民國 一0一 年 十一 月

一種新穎自行開發之快速精準量子模擬器用於三維度高應力下矽電洞能帶結構及反置層遷移率之研究

研究生: 李建志　　　　　指導教授: 陳明哲 博士

國立交通大學

電子工程學系 電子研究所博士班

摘要

對於持續微縮的電子元件，除了將會面對額外的量子侷限效應（不論是電場造成的量子侷限或是空間造成的量子侷限）之外，亦會面對複雜的機械應力（不論是有意或是無意的任何方向應力）。這兩個現象皆會對價電子能帶結構造成關鍵的影響，進而大大地改變電洞的電特性。換句話說，這將會在理論工作上造成額外的複雜程度和沉重的計算負擔。但是因為電洞特性的計算，例如電洞遷移率，完全根據價電子能帶結構來進行計算，所以並不意外，令人滿意的電性計算結果需要精細和高品質的價電子能帶結構計算來達成。此論文聚焦在電子元件 p 型反置層中的電洞特性，而我們自行開發的模擬器是根據六能帶 $k \cdot p$ 薛丁格·波松方程自洽方法來達成。

此論文主要的目的是：研究在顯著的量子侷限效應和複雜的應力影響下矽的反置層電洞特性。而根據此主題，論文的組織結構如下。首先，我們將介紹在 p 型反置層中價電子能帶結構。接下來，聚焦於 *p*-NEP 的數值計算方法和物理模

型，然而根據 *p*-NEP 的數值演算方法，電腦處理器計算時間會非常地漫長。因此，我們提出一個新穎的演算加速器，能本質地提升六能帶 $k \cdot p$ 薛丁格·波松的自洽模擬速度。此演算加速器是經由一個三角位能井為主的六能帶 $k \cdot p$ 模擬器，一個電洞等效質量近似技巧，和一個與導帶電子版本相近的薛丁格·波松自洽計算器所組成。加速器會輸出一個接近實際量子侷限靜電位能的初始解，且對不同的溫度、不同基板參雜濃度、反置層電洞濃度和表面晶格方向皆可行。其他論文發表的計算是支持我們(001)和(110)基板晶格方向的計算結果。全部的電腦處理器計算時間被減少到接近 8%沒有加速器的計算時間。加速器更普遍的應用也會在此說明。

接著，根據三組互異並以塊材為導向的 Luttinger 參數 γ_1, γ_2, 和 γ_3，以塊材為導向的 Luttinger 參數在六能帶 $k \cdot p$ 薛丁格·波松方程自洽方法的可行性被確認。以塊材為導向的 Luttinger 參數計算，(110)基板方向 p 型場效電晶體之實際電洞子能帶結構可以被良好地重現，並與最近 Takahashi 等人的 Shubnikov-de Haas (SdH)迴旋共振實驗比較。

更進一步，沿著三個晶格方向的單軸 GPa 等級應力造成的電洞遷移率變化可以分為四個分別的貢獻來討論：一、聲子震盪限制，二、表面粗糙限制，三、散射時間限制，四、傳導質量限制下的遷移率變化。在同一討論中，我們致力研究應力相關的三個材料參數，也是所謂的 Bir-Pikus 形變電位參數 a_υ, b, 和 d。並且，在數值上有著廣闊的分布。為了克服如此明顯的不一致性，我們詳盡地計算電洞反置層遷移率，發現了沿著單軸<110>方向的壓縮應力對電洞遷移率增加而言，a_υ 影響微弱，b 影響適中，而 d 影響劇烈。以上的結論提供了指引透過實驗決定主要參數 d，次要參數 b，及一般使用的 a_υ數值。另外，*p*-NEP 的使用者介面（ＵＩ）和模擬程序會示範操作，模擬的子能帶結構、臨界電壓、電容和閘極直接穿隧電流會被討論。最後，我們將總結研究結論。

關鍵字：量子侷限效應、機械應力、價電子能帶結構、六能帶 $k \cdot p$ 薛丁格·波松方程自洽、Luttinger 參數、Bir-Pikus 形變電位參數、電洞遷移率。

A New In-House Fast Sophisticated Quantum Simulator for Silicon Hole Band Structure and Inversion-Layer Mobility under Three-Dimensional GPa-Level Stresses

Student: Chien-Chih Lee Advisor: Dr. Ming-Jer Chen

Department of Electronics Engineering and Institute of Electronics
National Chiao Tung University
Hsinchu, Taiwan

Abstract

The continuously scaled electronic devices encounter not only the extra quantum confinement (no matter from the field confinement or from the space confinement) but also the complicated mechanical stresses (no matter the intentional or unintentional stressors along the arbitrary directions). Both of these two phenomena cause the crucial impacts on the valence-band structure which can greatly alter the hole electrical properties. In other words, these lead to the extra complexities and the heavy computation burden in the theoretical work. Since the evaluation of the hole electrical properties such as hole mobility fully rely on the valence subband structures, with no surprise the precise and fine quality of valence subband structures are urgently required to achieve the satisfactory calculations. With the six-band $k \cdot p$ Schrödinger-Poisson self-consistent method this dissertation will focus on the hole electrical properties in *p*-type inversion layer of the electronic devices via the self-developed simulator, *p*-NEP (abbreviation of p-type *Nano Electronics Physics*).

The main purpose of the dissertation is to investigate the hole electrical

properties in silicon inversion layer beneath on the significant quantum confinement and the complicated mechanical stresses. Based on this main topic, the organization of this dissertation is described below.

First, an introduction to the valence band structures in p-type inversion layer is described. Then, the dissertation is focused on the numerical techniques and physical models of *p*-NEP. However, according to the algorithm of *p*-NEP, the CPU time is extraordinarily long. To overcome the issue, we present a novel computational accelerator to intrinsically boost a self-consistent six-band $k \cdot p$ Schrödinger-Poisson simulation. This accelerator comprises a triangular potential based six-band $k \cdot p$ simulator, a hole effective mass approximation (EMA) technique, and an electron analogue version of the self-consistent Schrödinger and Poisson's equations solver. The outcome of the accelerator furnishes the initial solution of the confining electrostatic potential and is likely to be close to the realistic one, valid for different temperatures, substrate doping concentrations, inversion hole densities, and surface orientations. The results on (001) and (110) substrates are supported by those published in the literature. The overall CPU time is reduced down to around 8% of that without the accelerator. The application of the proposed accelerator to more general situations is projected as well.

Secondly, according to three distinct sets of the bulk oriented Luttinger parameters γ_1, γ_2, and γ_3, the validity of the bulk oriented Luttinger parameters in the six-band $k \cdot p$ Schrödinger-Poisson self-consistent method is confirmed. With the the bulk oriented Luttinger parameters, the *realistic* hole subband structures in (110) p-MOSFETs can be well reproduced in comparison with the recent Shubnikov-de Haas (SdH) oscillation experiment by Takahashi, et al.

Thirdly, the hole mobility change for GPa-level uniaxial stresses along each of

three crystallographic directions are distinguished into four contributing componds: (i) phonon-limited, (ii) surface-roughness-limited, (iii) scattering-time-limited, and (iv) conductive-mass-limited mobility changes. It is also dedicated to three key strain-related material parameters, namely the Bir-Pikus deformation potentials a_{υ}, b, and d, which are widespread in magnitude. To improve such large discrepancies, we conduct sophisticated calculations on <110>/(001) and <110>/(110) hole inversion-layer mobility. We find that, to affect the calculated hole mobility enhancement, a_{υ} is weak, b is moderate, and d is strong, particularly for the uniaxial compressive stress along the <110> direction. This provides guidelines for an experimental determination of the primary factor, d, and the secondary factor, b, with the commonly used values for a_{υ}. The user interface (UI) and simulation process of *p*-NEP are further demonstrated. The resulting subbnad structures, threshold voltage, capacitance, and gate direct tunneling current are all addressed. Finally, we summarize the conclusions of our works.

Keyword: quantum confinement, mechanical stress, valence-band structure, six-band $k \cdot p$ Schrödinger-Poisson self-consistent method, Luttinger parameters, Bir-Pikus deformation potentials, hole mobility.

謝誌

在漫漫求學長路上，能有幸完成此博士論文，首先必須感謝我的內人，如怡，以及父親，裕瑞、母親，雯彣、及弟弟，建穎。因為每當遭遇了看似過不了的難關時，他們的精神支持總是給予最大的力量，讓我一躍而過。還有我的岳父，清任及岳母，美惠，感謝他們信任及關心，並也感謝每一位親愛家人的由衷關心。最重要的是要感謝我的指導教授，陳明哲老師，他對學術的真誠熱情激發了每位學生的潛能，更重要的是對每位學生無私的關心。老師的一句話「歸零」，直到現在都還深深影響著我，每當在研究或生活上遇到難解的問題時，都會先讓心態歸零清空，然後再來解決問題，這給予我莫大的幫助。

非常感恩口試委員，胡振國教授、鄭舜仁教授、林鴻志教授、簡昭欣教授、余宗興經理、以及吳忠政處長的百忙中抽空指導，每一位口試委員所提出的精闢見解皆有助我釐清盲點和提升視野，獲益良多。

另外，要感謝師母侯錦珊女士、實驗室呂明霈、林大文學長總是在我沒有頭緒時，提出了精闢的方向。感謝實驗室學弟妹寬豪、霖祥、宛勵的相助，及韋漢、立鳴、宮強和每位學弟妹同仁的技術支援和戰友情誼。也要感謝在德國的友人：Thomas Seyller 教授、Peter Wehrfritz、Beate 和 Matthias 讓我在異地仍感受到溫暖。

最後，要把此論文獻給還待在老婆肚子中的兒子，親愛的外公外婆，以及在上天眷顧著我們的爺爺和奶奶。因為，於戰亂而離鄉背井的大時代裡，沒有他們在台灣這片土地上的艱辛開拓，就沒有我們現在的一絲一毫成就。

Table of Contents

Table Captions

Chapter 2

Chapter 4

Chapter 5

Figure Captions

Chapter 1

Chapter 2

Chapter 3

Chapter 4

Chapter 5

Chapter 6

Chapter 1

Introduction to Valence-Band Structure in *p*-type Inversion Layer

1.1 Overview

As widely recognized, the method of so-called "effective mass theory" can describe the carriers moving in the perturbed periodic crystal field by introducing a mass tensor into Schrödinger equation. Through the cyclotron resonance experiments [1],[2],[3], the mass tensors of conduction band and valence band can be determined with some accuracy. However, different conduction and valence bands in diamond and zinc blende structure semiconductors such as silicon are found: (i) the top valence band locates at the Γ point of the first Brillouin zone, in contrast to the conduction band minimum near the first Brillouin zone edge along <100> directions, and (ii) within the perturbed energy range around Γ point, the conduction band structures have the more perfectly parabolic property than the obviously anisotropic and non-parabolic properties existing in the valence band structures as shown in Fig. 1.1 for heavy-, light-, and split-off-hole bands. Furthermore, the extra degeneracy at Γ point and the spin-orbit coupling, or even the applied mechanical strain all bring the additional complexities in the valence band structures. In order to deal with the above complexities in the realistic valence band structures, Luttinger and Kohn [4] and Bir and Pikus [5] separately proposed the experiment associated Luttinger six-band $k \cdot p$ Hamiltonian and Bir-Pikus deformation potentials which importantly push forward the theoretical study on the strained valence band structures of diamond and zinc blende structure semiconductors.

Nowadays, the highly scaled electronic devices encounter not only the extra quantum confinement (no matter from the field confinement or from the space confinement) but also the complicated mechanical stresses (no matter the intentional or unintentional stressors from arbitrary directions). Both of these two phenomena cause the crucial impacts on the valence band structures which greatly alter the hole electrical properties. In other words, these lead to the extra complexity and the heavy computation burden in the theoretical work. To conclude the existing calculation methods to deal with the subband structure (due to the extra quantum confinement) in p-type inversion layer, Fig. 1.2 addresses several algorithms [6]-[11], e.g. the constant effective mass as the conduction band counterpart, the six-band $k \cdot p$ method, and the pseudopotential method in combination with the Monte Carlo numerical technique [12], the iterative numerical technique [13], even or the analytical triangular potential technique. Then, we systematically explain the trade-off between these algorithms with the calculation efficiency and precision in Fig. 1.3. Since the evaluation of the hole electrical property such as hole mobility fully relies on the valence subband structures, with no surprise the precise and fine quality of valence subband structures are urgently required to achieve the satisfactory calculations. With the six-band $k \cdot p$ Schrödinger-Poisson self-consistent method as originally demonstrated by Bangert, von Klitzing and Landwehr [6] and by Ohkawa and Uemura [7], this dissertation will focus on the hole electrical properties in *p*-type inversion layer of the electronic devices via the self-developed simulator, *p*-NEP.

1.2 Dissertation Organization

The main purpose of the dissertation is to investigate the hole electrical properties of the silicon inversion layer beneath in the presences of both the significant quantum confinement and the complicated mechanical stresses. Based on this main topic, the organization of this dissertation is described below.

First, an introduction to the valence band structures in p-type inversion layer is described in Chapter 1. Then, Chapter 2 of the dissertation is focused on the numerical techniques and physical models of *p*-NEP. About the numerical technique, the six-band $k \cdot p$ Schrödinger-Poisson self-consistent method is used to obtain the precise valence subband structures, inversion carrier distribution, and self-consistent potential profile. Concerning the physical models, (i) the phonon scattering rate, surface roughness scattering rate, and Kubo-Greenwood formula are used to achieve the elaborate transport calculation; (ii) the WKB approximation method is used to evaluate hole gate direct tunneling; and (iii) because of the highlighted three dimensional mechanical stresses in the dissertation, the stress-to-strain tensor is included as well. In general, *p*-NEP is a flexible simulator containing the functions of above calculations with the alternative materials (silicon, germanium, and gallium arsenide), the alternative wafer orientations ((001), (110), and (111)), the alternative temperature conditions (2K to 400K), the alternative stress conditions (GPa-level uniaxial and biaxial stresses), and the alternative substrate doping concentrations ($1\text{x}10^{15}$ to $6\text{x}10^{18}$ cm^{-3}).

However, according to the algorithm of *p*-NEP, the computation burden is still extremely heavy to remain the tolerable computation error. Thus, Chapter 3 presents a novel computational accelerator to intrinsically boost the self-consistent six-band $k \cdot p$ Schrödinger-Poisson simulation. This accelerator comprises a triangular potential based six-band $k \cdot p$ simulator, a hole effective mass approximation (EMA) technique, and an electron analogue version of the self-consistent Schrödinger and Poisson's equations solver. The outcome of the accelerator furnishes the initial solution of the confining electrostatic potential and is likely to be close to the realistic one, valid for different temperatures, substrate doping concentrations, inversion hole densities, and surface orientations. The results on (001) and (110) substrates are supported by those published in the literature. The overall CPU time is reduced down to around 8% of that without the accelerator. The application of the proposed accelerator to more general situations is projected as well.

Secondly, according to three distinct sets of the bulk oriented Luttinger parameters γ_1, γ_2, and γ_3, the validity of the bulk oriented Luttinger parameters in the six-band $k \cdot p$ Schrödinger-Poisson self-consistent method is confirmed in Chapter 4. With the bulk oriented Luttinger parameters, the *realistic* hole subband structures in (110) p-MOSFETs can be well reproduced in comparison with the recent Shubnikov-de Haas (SdH) oscillation experiment by Takahashi, et al.

Thirdly, the hole mobility change for GPa-level uniaxial stresses along each of three crystallographic directions are distinguished into four contributions: (i) the phonon-limited, (ii) the surface-roughness-limited, (iii) the scattering-time-limited, and (iv) the conductivity-effective-mass-limited mobility changes in Chapter 5. In the same chapter, it is also dedicated to three key strain-related material parameters, namely the Bir-Pikus deformation potentials a_υ, b, and d, which are widespread in magnitude. To improve such large discrepancies, we conduct sophisticated calculations on <110>/(001) and <110>/(110) hole inversion-layer mobility. We find that, to affect the calculated hole mobility enhancement, a_υ is weak, b is moderate, and d is strong, particularly for the uniaxial compressive stress along the <110> direction. This provides guidelines for an experimental determination of the primary factor, d, and the secondary factor, b, with the commonly used values for a_υ. In Chapter 6, the user interface (UI) and simulation process of *p*-NEP are demonstrated. The resulting subbnad structures, threshold voltage, capacitance, and gate direct tunneling current are discussed. Finally, in Chapter 7 we summarize the conclusions of our works.

References

[1] G. Dresselhaus, A. F. Kip, and C. Kittel, "Observation of cyclotron resonance in germanium crystals," *Phys. Rev.*, vol. 92, no. 3, p. 827, Nov. 1953

[2] B. Lax, H. J. Zeiger, R. N. Dexter, and E. S. Rosenblum, "Directional properties of the cyclotron resonance in germanium," *Phys. Rev.*, vol. 93, no. 6, pp. 1418-1420, Mar. 1954.

[3] R. N. Dexer, H. J. Zeiger, and B. Lax, "Anisotropy of cyclotron resonance of holes in germanium," *Phys. Rev.*, vol. 95, no. 2, pp. 557-558, Jul. 1954.

[4] J. M. Luttinger and W. Kohn, "Motion of electrons and holes in perturbed periodic fields," *Phys. Rev.*, vol. 97, pp. 869-883, Feb. 1955.

[5] G. L. Bir and G. E. Pikus, "Theory of the deformation potential for semiconductors with a complex band structure," *Sov. Phys. Solid State*, vol. 2, pp.2287-2300, Sept. 1960.

[6] E. Bangert, K. von Klitzing, and G. Landwehr, "Self-consistent calculations of electric subbands in p-type silicon inversion layers," in *Proceedings of the Twelfth International Conference on the Physics of Semiconductors*, *Stuttgart*, edited by M. H. Pilkuhn (Teubner, Stuttgart, 1974), pp. 714-718.

[7] F. J. Ohkawa and Y. Uemura, "Hartree approximation for the electronic structure of a p-channel inversion layer of silicon M. O. S.," *Prog. Theor. Phys.*, no. 57, pp. 164-175, 1975.

[8] B. K. Ridley, Quantum Processes in Semiconductors, 3rd. ed. Oxford, U.K.: Clarendon , 1993, ch. 1.

[9] H. Nakatsuji, Y. Kamakura, and K. Tangiguchi, "A study of subband structure and transport of two-dimensional holes in strained-Si p-MOSFETs using full-band modeling," in *IEDM Tech. Dig.*, 2002, pp. 727-730.

[10] T. Low, Y. T. Hou, and M. F. Li, "Improved one-band self-consistent effective mass methods for hole quantization in p-MOSFET," *IEEE Trans. Electron Devices*, vol. **50**, no. 5, pp. 1284-1289, May 2003.

[11] M. V. Fischetti, Z. Ren, P. M. Solomon, M. Yang, and K. Rim, "Six-band $k \cdot p$ calculation of the hole mobility in silicon inversion layers: Dependence on surface orientation, strain, and silicon thickness," *J. Appl. Phys.*, vol. 94, no. 2, pp. 1079-1095, Jul. 2003.

[12] C. Jacoboni and P. Lugli, The Monte Carlo Method for Semiconductor Device Simulation, Springer-Verlag/Wien-New York, 1989.

[13] S. E. Laux and F. Stern, "Electron states in narrow gate-induced channels in Si," *Appl. Phys. Lett.*, vol. 49, no. 2, pp. 91-93, Jul. 1986.

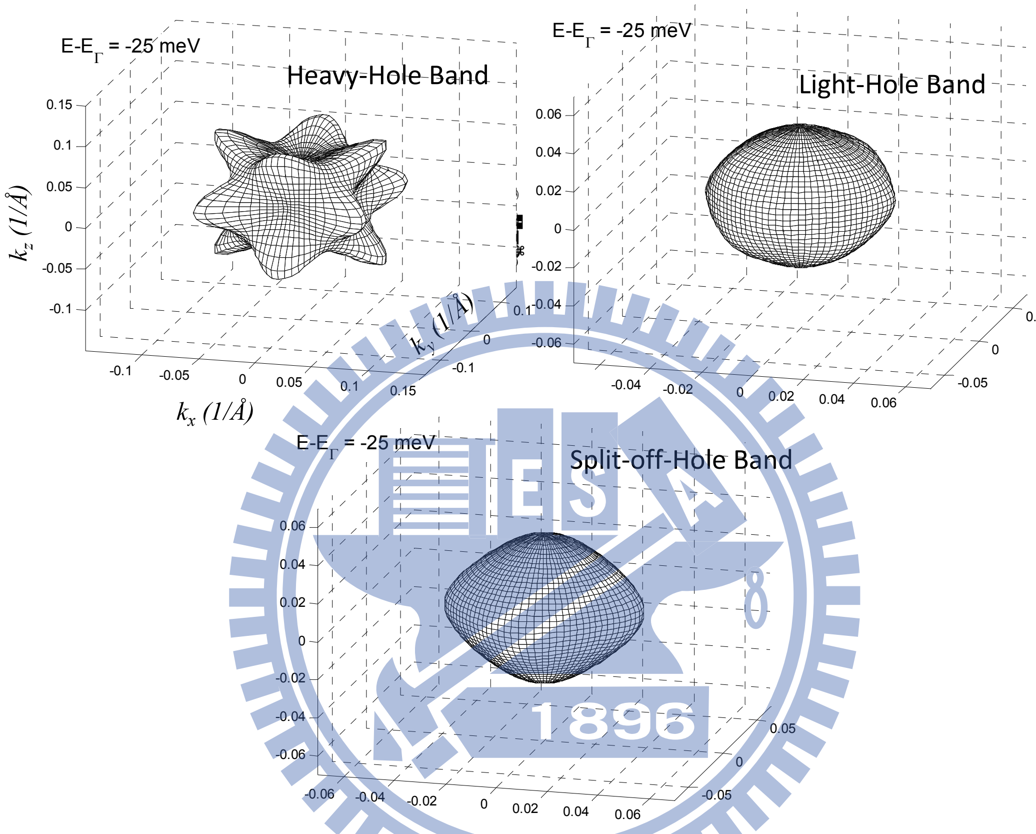

Fig. 1.1 Constant energy surfaces of heavy-hole, light-hole, and split-off-hole bulk valence bands in k-space at E-E_Γ=25 meV.

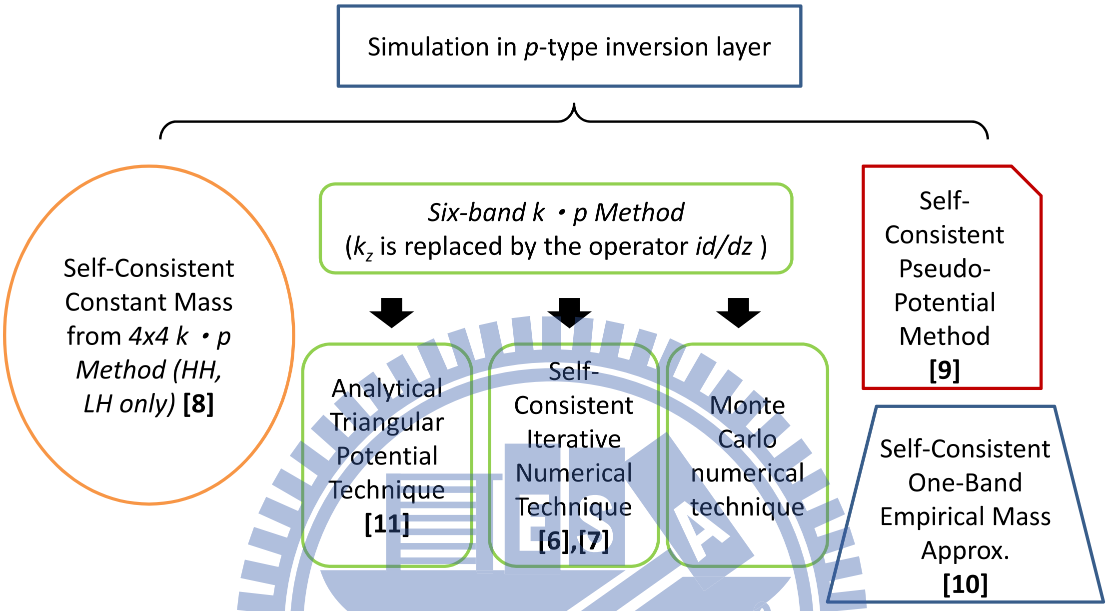

Fig. 1.2 Comparison of existing algorithms [6]-[11], e.g. the constant effective mass as the conduction band counterpart, the six-band $k \cdot p$ method, and the pseudopotential method in combination with the Monte Carlo numerical technique, the iterative numerical technique, or the analytical triangular potential technique.

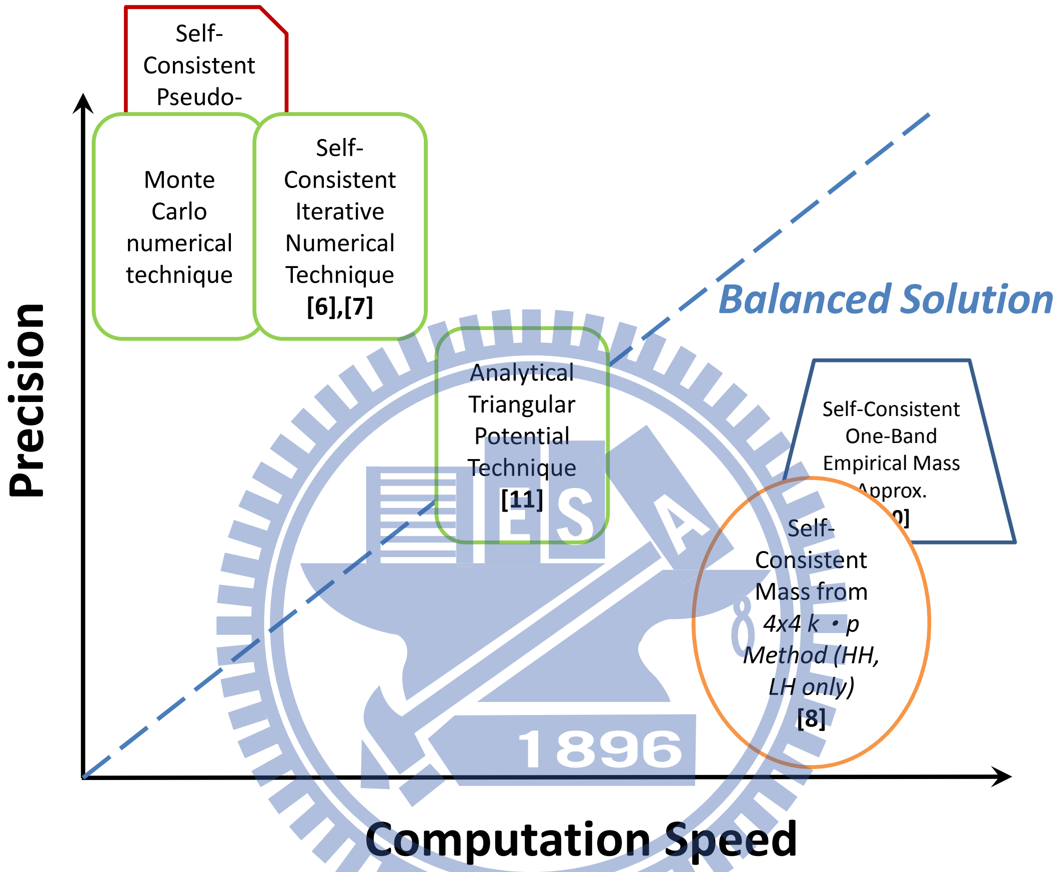

Fig. 1.3 Demonstration of the trade-off of the calculation efficiency and precision between above-mentioned algorithms.

Chapter 2

Simulation Tool: *p*-NEP

2.1 Introduction

Herein, we will introduce our self-consistent solver, named as *p*-NEP, of coupled Poisson and Schrödinger's equations in a six-band k・p valence-band structure. It can apply to different surface orientations such as (001), (110), (111), and (11x) in general. And the strain Hamiltonian has already been incorporated into the solver. In Section 2.2, the detailed numerical techniques of *p*-NEP will be explained. Next, the physical models in order to calculate hole inversion mobility and gate direct tunneling current beneath under different stress conditions will be displayed in Section 2.3. Finally, the functions and operational range of *p*-NEP will be discussed and listed in a table.

2.2 Numerical Techniques

2.2.1 Time-independent Schrödinger and Poisson's Equations: Matrix Techniques

It is well-recognized that the time-independent Schrödinger equation in the quantum mechanics can be expressed in terms of a matrix equation:

$$-\frac{\hbar^2}{2m}\nabla^2\Psi + V\Psi = E\Psi \quad . \tag{2.2.1.1}$$

This approach is widely adopted in the band-structure simulation when it is focused on bound or quasi-bound states in a spatially varying potential V inside the highly scaled semiconductor devices. Let us assume that the wave-function Ψ is confined in a small region of ***W***. We divide this region into ℓ intervals of the equal-distance $\Delta x = W/\ell$. The *i*th mesh point is indexed as x_i. In general, the wave-function Ψ we are looking for can be expanded by an orthogonal basis set $\{\psi_n\}$

$$\Psi = \sum_n a_n \psi_n \,, \tag{2.2.1.2}$$

where the ψ_n is the normalized wave-function at the mesh point x_n and the existing probability of ψ_n is exactly zero outside the interval *n*. According to Eq. (2.2.1.1), the Schrödinger equation in the confined direction can be written numerically as

$$-\frac{\hbar^2}{2m}\left[\frac{\Psi(x-\Delta x) - 2\Psi(x) + \Psi(x+\Delta x)}{\Delta x^2}\right] + V(x)\Psi(x) = E\Psi(x) \,. \tag{2.2.1.3}$$

Substituting Eq. (2.2.1.2) into Eq. (2.2.1.3), we get a set of ℓ equations (we are assuming $a_0 = a_{\ell+1} = 0$, i.e., the wave-function is localized in the space ***W***). After taking the outer product of $\psi_1, \psi_2, \psi_3, \ldots \psi_\ell$,the matrix form of the one dimensional Schrödinger equation is presented by

$$\begin{bmatrix} A_{(x_1)} & B & 0 & \cdots & 0 \\ B & A_{(x_2)} & B & & 0 \\ 0 & B & A_{(x_3)} & B & \vdots \\ \vdots & & & \ddots & 0 \\ 0 & \cdots & 0 & B & A_{(x_\ell)} \end{bmatrix} \bullet \begin{bmatrix} a_1\psi_1 \\ a_2\psi_2 \\ \vdots \\ \vdots \\ a_n\psi_\ell \end{bmatrix}_{\ell\times 1} = 0 \tag{2.2.1.4}$$

with

$$A_{(x_i)} = \frac{\hbar^2}{m(\Delta x)^2} + V(x_i) - E\,, \tag{2.2.1.5}$$

$$B = -\frac{\hbar^2}{2m(\Delta x)^2}. \tag{2.2.1.6}$$

Obviously, Eq. (2.2.1.4) turns the complex differential Schrödinger equation into a common eigen-value problem and we will get the ℓ eigen-values corresponding to the ℓ eigen-function. The smallest eigen-value refers to the ground state while the others refer to the excited states.

For solving the Poisson equation with the matrix technique, there is a well-known numerical analysis of the Newton-Raphson method (or Newton-Fourier method) for finding successively better approximations to the zeros (or roots) of a real-value function. Newton's method can converge remarkably quickly; especially if the iteration begins "sufficiently near" the desired root. First, we start with an initial value, for example v_0, and look for the corresponding function of $\boldsymbol{R}$. And then, the function is approximated by its sloped line, and one computes the V-intercept of this tangent line (which is easily done with elementary algebra). This V-intercept will typically be a better approximation to the function's root than the original guess, and the method can be iterated. This iteration process can be expressed as

$$V_n = V_{n-1} - \Delta V \tag{2.2.1.7}$$

$$\Delta V = \frac{R}{\left(\frac{\partial R}{\partial V}\right)} \tag{2.2.1.8}$$

Now, we write the 1D Poisson's equation for $N \times N$ matrix case as below:

$$\frac{\partial^2 V}{\partial z^2} = -\frac{\rho}{\varepsilon} \tag{2.2.1.9}$$

$$\begin{bmatrix} -\frac{2}{\Delta z^2} & \frac{1}{\Delta z^2} & 0 & \cdots & 0 \\ \frac{1}{\Delta z^2} & -\frac{2}{\Delta z^2} & \frac{1}{\Delta z^2} & & 0 \\ 0 & \frac{1}{\Delta z^2} & -\frac{2}{\Delta z^2} & \frac{1}{\Delta z^2} & \vdots \\ \vdots & & & \ddots & 0 \\ 0 & \cdots & 0 & \frac{1}{\Delta z^2} & -\frac{2}{\Delta z^2} \end{bmatrix}_{N\times N} \bullet \begin{bmatrix} V_1 \\ V_2 \\ \vdots \\ \vdots \\ V_N \end{bmatrix}_{N\times 1} = \begin{bmatrix} \rho_1 \\ \rho_2 \\ \vdots \\ \vdots \\ \rho_N \end{bmatrix}_{N\times 1} \tag{2.2.1.10}$$

and let $AV = \rho$, where $\boldsymbol{A}$ is second-order differential matrix, ρ is carrier charge density:

$$A = \begin{bmatrix} -\frac{2}{\Delta z^2} & \frac{1}{\Delta z^2} & 0 & \cdots & 0 \\ \frac{1}{\Delta z^2} & -\frac{2}{\Delta z^2} & \frac{1}{\Delta z^2} & & 0 \\ 0 & \frac{1}{\Delta z^2} & -\frac{2}{\Delta z^2} & \frac{1}{\Delta z^2} & \vdots \\ \vdots & & & \ddots & 0 \\ 0 & \cdots & 0 & \frac{1}{\Delta z^2} & -\frac{2}{\Delta z^2} \end{bmatrix}_{N\times N} \tag{2.2.1.11}$$

$$V = \begin{bmatrix} V_1 \\ V_2 \\ \vdots \\ \vdots \\ V_N \end{bmatrix}_{N\times 1} \tag{2.2.1.12}$$

$$\rho = \begin{bmatrix} \rho_1 \\ \rho_2 \\ \vdots \\ \vdots \\ \rho_N \end{bmatrix}_{N\times 1} . \tag{2.2.1.13}$$

Finally, we apply Newton-Raphson method to solve Poisson and Schrődinger equations self-consistently. Therefore, we can hence express the Poisson equation as follows:

$$AV - \rho = R \tag{2.2.1.14}$$

and differentiate the Eq. (2.2.1.13) by V, we can obtain the following:

$$A - \frac{\partial \rho}{\partial V} = \frac{\partial R}{\partial V} = NR \tag{2.2.1.15}$$

and Eq. (2.2.1.8) can be rewritten as

$$\Delta V = \frac{R}{\frac{\partial R}{\partial V}} = \frac{R}{NR} \tag{2.2.1.16}$$

2.2.2 Six-Band $k \cdot p$ Schrödinger-Poisson Self-Consistent Method

By following the theoretical work by Bangert, von Klitzing and Landwehr [1] and by Ohkawa and Uemura [2], a six-band silicon $k \cdot p$ method, along with the solving of Schrödinger and Poisson's equations in a self-consistent potential well beneath the gate oxide of bulk p-MOSFET, will be employed here. In this simulation framework, we solve the wave equation iteratively:

$$\left[-H_{kp}\left(k_x, k_y, k_x = -i\frac{d}{dz}\right) + eV(z)\right] \cdot \xi_{k_x,k_y}(z) = E\left(k_x, k_y\right) \cdot \xi_{k_x,k_y}, \tag{2.2.2.1}$$

Here, e is the free electron charge, the confining electrostatic potential $V(z)$ refers to the solution of Poisson equation from the initial or previous iterative loop; and the $k \cdot p$ Hamiltonian H_{kp} is the Luttinger-Kohn Hamiltonian H_{LK} [3] plus the strain Hamiltonian H_{strain} [4]. Those expressions are given in [5]. Therefore, the 6×6 Hamiltonian is given by

$$H_{kp}=H_{LK}+H_{strain}=\begin{bmatrix} -P-Q & L & -M & 0 & \frac{1}{\sqrt{2}}L & -\sqrt{2}M \\ L^{+} & -P+Q & 0 & -M & \sqrt{2}Q & -\sqrt{\frac{3}{2}}L \\ -M^{+} & 0 & -P+Q & -L & -\sqrt{\frac{3}{2}}L^{+} & -\sqrt{2}Q \\ 0 & -M^{+} & -L^{+} & -P-Q & \sqrt{2}M^{+} & \frac{1}{\sqrt{2}}L^{+} \\ \frac{1}{\sqrt{2}}L^{+} & \sqrt{2}Q^{+} & -\sqrt{\frac{3}{2}}L & \sqrt{2}M & -P-\Delta & 0 \\ -\sqrt{2}M^{+} & -\sqrt{\frac{3}{2}}L^{+} & -\sqrt{2}Q^{+} & \frac{1}{\sqrt{2}}L & 0 & -P-\Delta \end{bmatrix}, \tag{2.2.2.2}$$

where

$$\begin{aligned} P&=P_k+P_\varepsilon \\ Q&=Q_k+Q_\varepsilon \\ L&=L_k+L_\varepsilon \\ M&=M_k+M_\varepsilon \end{aligned}\quad , \tag{2.2.2.3}$$

$$\begin{aligned} P_k&=\frac{\hbar^2}{2m_0}\gamma_1\left(k_x^2+k_y^2+k_z^2\right) \\ Q_k&=\frac{\hbar^2}{2m_0}\gamma_2\left(k_x^2+k_y^2-2k_z^2\right) \\ L_k&=\frac{\hbar^2}{m_0}\sqrt{3}\gamma_3\left(k_x-ik_y\right)k_z \\ M_k&=-\frac{\hbar^2}{2m_0}\sqrt{3}\left[\gamma_2\left(k_x^2-k_y^2\right)-2i\gamma_3k_xk_y\right]; \\ P_\varepsilon&=-a_v\left(\varepsilon_{xx}+\varepsilon_{yy}+\varepsilon_{zz}\right) \\ Q_\varepsilon&=-\frac{b}{2}\left(\varepsilon_{xx}+\varepsilon_{yy}-2\varepsilon_{zz}\right) \\ L_\varepsilon&=-d\left(\varepsilon_{xz}-i\varepsilon_{yz}\right) \\ M_\varepsilon&=\frac{\sqrt{3}}{2}b\left(\varepsilon_{xx}-\varepsilon_{yy}\right)-id\varepsilon_{xy} \end{aligned}\quad . \tag{2.2.2.4}$$

the P_k, Q_k, L_k, and M_k are the $k\cdot p$ terms and the P_ε, Q_ε, L_ε and M_ε are the strain terms and Δ is the split-off energy. The Luttinger parameters are γ_1, γ_2, and γ_3, and the Bir-Pikus deformation potentials are a_υ, b, and d.

In the numerical calculation, the wave vector, k_z, is replaced by the operator,

$-i\frac{d}{dz}$, and the quantization z-direction length (20 nm in this work) in the simulation is divided into a mesh of N_z points (N_z=101 in this work). Contrary to the quantization region, the z-direction length of the bulk region is equal to maximum depletion width plus 400 nm additionally. Thus, focused on the quantization region, Eq. (2.2.2.1) becomes the $6N_z \times 6N_z$ eigenvalue problem. Precisely speaking, this $6N_z \times 6N_z$ eigenvalue matrix can be expressed as the tridiagonal block form

$$\begin{bmatrix} \cdot & \cdot & \cdot & \cdot & \cdot & \cdot & \cdot \\ \cdot & D^- & D^0_{l-1} & D^+ & 0 & 0 & \cdot \\ \cdot & 0 & D^- & D^0_l & D^+ & 0 & \cdot \\ \cdot & 0 & 0 & D^- & D^0_{l+1} & D^+ & \cdot \\ \cdot & \cdot & \cdot & \cdot & \cdot & \cdot & \cdot \end{bmatrix} \begin{bmatrix} \cdot \\ \xi^{l-1}_{k_x,k_y} \\ \xi^{l}_{k_x,k_y} \\ \xi^{l+1}_{k_x,k_y} \\ \cdot \end{bmatrix} = E(k_x,k_y) \begin{bmatrix} \cdot \\ \xi^{l-1}_{k_x,k_y} \\ \xi^{l}_{k_x,k_y} \\ \xi^{l+1}_{k_x,k_y} \\ \cdot \end{bmatrix}, \tag{2.2.2.5}$$

where each ξ_{k_x,k_y} is a six-component column vector. D^+, D^0 and D^- are 6×6 block-diagonal difference operators expressed as below

$$\begin{aligned} &H_{kp}=H_0+H_1\cdot k_z+H_2\cdot k_z^2, \\ &D^+=\frac{H_1}{2i\Delta z}-\frac{H_2}{(\Delta z)^2}, \\ &D^0=H_0+\frac{2H_2}{(\Delta z)^2}, \\ &D^-=-\frac{H_1}{2i\Delta z}-\frac{H_2}{(\Delta z)^2}. \end{aligned} \tag{2.2.2.6}$$

The solving of Eq. (2.2.2.5) yields the same number of the eigenvalue matrices, $E(k_x,k_y)$, as well as the wavefunction $\xi_{kx,ky}(z)$. With the known equilibrium Fermi level E_f, the distribution of the total hole density per area $P_{inv}(z)$ can be obtained as follows

$$P_{inv}(z)=\frac{1}{(2\pi)^2}\int\sum_i\left|\xi_0^i(z)\right|^2\cdot\left(1+\exp\left(\frac{E^i(k_x,k_y)-E_f}{k_BT}\right)\right)dk_x dk_y\,, \tag{2.2.2.7}$$

where i is the subband index and $\xi_0^i(z)$ is the wavefunction at the subband minimum. Then, to substitute Eq. (2.2.2.7) into the Poisson equation,

$$\frac{d^2}{dz^2}V(z) = -\frac{e^2}{\epsilon_s}\left(P_{inv}(z) + P_{dep}(z) - N_e(z)\right), \tag{2.2.2.8}$$

where $P_{dep}(z)$ and $N_e(z)$ are the density of depleted ionized donors and free electrons in the depletion layer, the new surface potential $V(z)$ can be obtained by the Newton-Raphson method, followed by the next iterative loop via Eq. (2.2.2.1).

2.3 Physical Models

2.3.1 Kubo-Greenwood Formula

The outcomes of the solver *p*-NEP contain the hole subband energy level, the Fermi level, the wave function, the DOS function, and the strained *E*-*k* structure. Then, the hole inversion-layer mobility can be calculated using the Kubo-Greenwood formula [6]-[8]:

$$\mu_{xx} = \frac{e}{4\pi^2 k_B T P_{inv}} \sum_{\mu} \int d^2\boldsymbol{k}\, v_x^{\mu}(\boldsymbol{k}) \times v_x^{\mu}(\boldsymbol{k}) \times \tau_{total}^{\mu}(\boldsymbol{k}) \times f_0(\boldsymbol{k})\left(1 - f_0(\boldsymbol{k})\right) \tag{2.3.1.1}$$

where e is the free electron charge, P_{inv} is the total hole density per unit area which sums $P_{inv}(z)$ along the z-direction, v_x^{μ} is the group velocity of subband μ along *x* direction, and f_0 is the Fermi-Dirac distribution function in equilibrium. Under the momentum relaxation time approximation, the total scattering time τ_{total}^{μ} of subband μin (1) can relate to acoustic phonon scattering, optical phonon scattering, and surface roughness scattering through the expression: $\frac{1}{\tau_{total}^{\mu}(\boldsymbol{k})} = \frac{1}{\tau_{ac}^{\mu}(\boldsymbol{k})} + \frac{1}{\tau_{op}^{\mu}(\boldsymbol{k})} + \frac{1}{\tau_{sr}^{\mu}(\boldsymbol{k})}$. In this dissertation, eighteen lowest subbands were used in the mobility calculation.

2.3.2 Acoustic Phonon Scattering

We followed the isotropic treatment by Fischetti *et al.* [9] concerning acoustic phonon scattering, but did not take into account the inelastic and dielectric screening effects of acoustic phonons in this work. The critical parameter, namely, the acoustic deformation potential D_{ac}, is strongly connected to Bir-Pikus deformation potentials [4],[10],[11]. According to Lawaetz [11], D_{ac} can be formulated as

$$D_{ac}^2 = a_v^2 + c_l/c_t\left(b^2 + \frac{1}{2}d^2\right);$$

$$c_l = \frac{(3c_{11}+2c_{12}+4c_{44})}{5};$$

$$c_t = \frac{(c_{11}-c_{12}+3c_{44})}{5}, \qquad (2.3.2.1)$$

where c_l and c_t are the average longitudinal and transverse elastic coefficients, respectively. $c_{11}, c_{12},$ and c_{44} are the elastic coefficient elements whose values are listed in Table II. The elastic acoustic phonon scattering rate model used in this work is

$$\frac{1}{\tau_{ac}^{\mu}(\boldsymbol{k})} = \frac{2\pi k_B T D_{ac}^2}{\hbar\rho v_l^2}\sum_{\upsilon} F_{\upsilon\mu}\, DOS_{\upsilon}\left(E_{\mu}(\boldsymbol{k})\right), \qquad (2.3.2.2)$$

where $F_{\upsilon\mu}$ is equal to $\int\left|\xi_0^{\mu}(z)\cdot\xi_0^{\nu*}(z)\right|^2 dz$, the wavefunction $\xi_0(z)$ overlap integral between the initial subband μ and the final subband ν. ρ and v_l denote the crystal density and the longitudinal sound velocity, respectively. Both intra- and inter-subband acoustic phonon scattering were considered in this work.

2.3.3 Optical Phonon Scattering

Optical phonon scattering involves the absorption and emission of optical phonons with the exchange of energy (61.2 meV in this dissertation). According to Wiley [12] and Costato and Reggiani [13], the optical deformation potential D_{op} can have the following formalism:

$$D_{op}^2 = \frac{c_l+2c_t}{\rho \bar{v}_s^2}\left(\frac{d_0}{a_0}\right)^2, \tag{2.3.3.1}$$

where a_0 is the lattice constant, d_0 is the deformation potential of optical phonons, and $\bar{v}_s$ is the average sound velocity consisting of the longitudinal and transverse sound velocity, v_l and v_t, respectively, with the formulation of $\bar{v}_s^2 = (v_l^2 + 2v_t^2)/3$. Then, the isotropic absorbing and emitting optical phonon scattering rate can be written as

$$\begin{aligned} \frac{1}{\tau_{op}^{\mu}(\boldsymbol{k})} = \frac{\pi D_{op}^2}{\rho\omega_{op}} \sum\nolimits_v F_{v\mu}\, DOS_v\big(E_\mu(\boldsymbol{k}) \mp \hbar\omega_{op}\big) \\ \times \frac{1-f_0\big(E_\mu(\boldsymbol{k})\mp\hbar\omega_{op}\big)}{1-f_0\big(E_\mu(\boldsymbol{k})\big)} \times \left(n_{op}+\frac{1}{2} \pm \frac{1}{2}\right), \end{aligned} \tag{2.3.3.2}$$

ω_{op} : optical phonon frequency,

n_{op} : Bose occupation factor of optical phonons

Eq. (2.3.3.2) features both intra- and inter-subband optical phonon scattering but with no screening effect in this work.

2.3.4 Surface Roughness Scattering

To deal with surface roughness scattering, we first followed Pham, *et al.* [14] and De Michielis, *et al.*, [15] to take only the intra-subband scattering. Then, the screening effect in the dielectric function as formulated by Yamakawa *et al.*[16] and Gámiz, *et al.* [17] was incorporated into the surface roughness scattering rate expression in the context of the exponential autocovariance function:

$$\frac{1}{\tau_{sr}^{\mu}(\boldsymbol{k})} = \frac{2\pi^2\Delta^2\lambda^2}{\hbar} \sum\nolimits_v \frac{(\Gamma_{eff}^{\mu,v})^2}{(2\pi)^2} \int \delta\left(E_v(\boldsymbol{k}') - E_\mu(\boldsymbol{k})\right) \times \frac{(1-\cos\theta)}{\epsilon(q)\times\left(1+\frac{q^2\lambda^2}{2}\right)^{1+n}}\, d^2\boldsymbol{k}', \tag{2.3.4.1}$$

Δ : rms height of the amplitude of the surface roughness,

λ : correlation length of the surface roughness,

q : $q = |\boldsymbol{k}' - \boldsymbol{k}|$,

θ : angle between $\boldsymbol{k}'$ **and** $\boldsymbol{k}$,

n : adjustable factor (= 1/2 in this work),

$\boldsymbol{\Gamma}_{eff}^{\mu,\nu}$: $\boldsymbol{\Gamma}_{eff}^{\mu,\nu} = \int \left(\xi_0^{\nu*}(z) \cdot \xi_0^{\mu}(z) \cdot \frac{deV(z)}{dz} + E_\nu^{(0)} \cdot \xi_0^{\nu*}(z) \cdot \frac{d\xi_0^{\mu}(z)}{dz} - E_\mu^{(0)} \cdot \frac{d\xi_0^{\nu*}(z)}{dz} \cdot \xi_0^{\mu}(z) \right) dz$,

$E_\nu^{(0)}$: energy minimum of subband ν

$\epsilon(q)$: static wave-vector-dependent dielectric function,

$\epsilon(q) = 1 + \frac{e^2}{2\epsilon_{Si}\epsilon_0} \frac{F(q)}{q} \int \frac{\delta\left(E_\nu(\boldsymbol{k}') - E_\mu(\boldsymbol{k})\right) d^2\boldsymbol{k}'}{(2\pi)^2}$;

$F(q) = \sum_\nu \int dz \int dz' |\xi_0^\nu(z)|^2 |\xi_0^\nu(z)|^2 e^{-q|z-z'|}$.

Importantly, Eq. (2.3.4.1) has the ability to adequately handle the angular dependence of surface roughness scattering, as shown in Fig. 2.1 in terms of the calculated unscreened scattering rate versus hole energy for both (001) and (110) substrates. It can also be seen from the figure that the scattering angular is more pronounced for GPa-level stress, especially on the (001) substrate.

2.3.5 WKB Based Hole Gate Direct Tunneling

According to the literatures [18]-[20],the isotropic hole direct tunneling current density contributed by the μth subband with WKB approximation can be written as

$$J_\mu = e \int_{E_\mu^{(0)}}^{\infty} F_i^\mu \cdot P_{inv}^\mu(E) \cdot T_{WKB}^\mu(E) \cdot T_R^\mu(E) dE, \qquad (2.3.5.1)$$

$$J_g = \sum_\mu J_\mu , \qquad (2.3.5.2)$$

where e denotes the elemental charge, F_i^μ is impact frequency of hole' wave packet on interface, $P_{inv}^\mu(E)$ is the inversion hole density of subband μ per energy per area, $T_{WKB}^\mu(E)$ is the transmission probability through insulator of WKB part, $T_R^\mu(E)$ is the transmission probability through insulator of reflection part. There are eighteen subbands taken into account in our calculation. The impact frequency is described as

$$F_i^{\mu} = \mathrm{eF_S}/2\left(2m_{QN}^{\mu}E_{\mu}^{(0)}\right)^{-\frac{1}{2}}\ , \tag{2.3.5.3}$$

Worth noting that the constant quantized effect mass m_{QN}^{μ} in Eq. (2.3.5.3) approximately obtained by the triangular potential method will be discussed in Chapter 3. For the inversion hole density, we calculate it through

$$P_{inv}^{\mu}(E) = DOS_{\mu}(E) \times f_0(E). \tag{2.3.5.4}$$

Two terms to be considered in the transmission probability through oxide layer, the first one is WKB part, which can be modeled as

$$\begin{aligned} T_{WKB}^{\mu}(E) &= \exp\left[-\frac{2}{\hbar}\left|\int_0^{T_{ox}}\sqrt{2m_{oxh}\big(E - eV(z)\big)dz}\right|\right] \\ &= \exp\left(\frac{4\sqrt{2m_{oxh}}\left(\varphi_{cath}^{3/2} - \varphi_{an}^{3/2}\right)}{3e\hbar|F_{ox}|}\right), \end{aligned} \tag{2.3.5.5}$$

$$\varphi_{cath} = e\chi_h - e|F_{ox}|T_{ox} - E,$$

$$\varphi_{an} = e\chi_h - E,$$

where φ_{cath} is the barrier height of the tunneling hole with total energy E at cathode side or gate/oxide interface, and φ_{an} is that at anode side or oxide/n-well interface with χ_h is the barrier height of oxide/Si interface. m_{oxh} is an important parameter featuring the quantum transport in oxide. The WKB approximation is only valid when the wavefunction phase change is much smaller than the amplitude change, In other words, the barrier potential of oxide must be very sharp and high enough to ensure the validity of WKB method. Another transmission probability is $T_R^{\mu}(E)$, which is given as

$$T_R^{\mu}(E) = \frac{4v_{si,\perp}^{\mu}(E)v_{ox}(\varphi_{an})}{v_{si,\perp}^{\mu}{}^{2}(E) + v_{ox}^2(\varphi_{an})} \times \frac{4v_{si,\perp}^{\mu}(E + e|F_{ox}|T_{ox})v_{ox}(\varphi_{cath})}{v_{si,\perp}^{\mu}{}^{2}(E + e|F_{ox}|T_{ox}) + v_{ox}^2(\varphi_{cath})}, \tag{2.3.5.6}$$

where $v_{si,\perp}^{\mu}(E)$ and $v_{si,\perp}^{\mu}(E + q|F_{ox}|T_{ox})$ are the group velocities of the holes incident and leaving oxide. The semi-classical forms can be simply depicted as

$$v_{si,\perp}^{\mu}(E) = v_{si,\perp}^{\mu}(z = 0) = \sqrt{\frac{2E_{\mu}^{(0)}}{m_{QN}^{\mu}}}\ ;$$

$$v^{\mu}_{si,\perp}(E+e|F_{ox}|T_{ox}) = \sqrt{\frac{2\left(E_{\mu}^{(0)}+q|F_{ox}|T_{ox}\right)}{m_{gate}}}. \tag{2.3.5.7}$$

Moreover, $v_{ox}(\varphi_{an})$ and $v_{ox}(\varphi_{cath})$ are the magnitudes of the purely imaginary group velocities of holes at the cathode and anode side within the oxide. The semi-classical form can be expressed as

$$v_{ox}(E) = \frac{1}{\hbar}\frac{dE_{ox}}{dk_{ox}} = \sqrt{\frac{2E_{ox}}{m_{oxh}}}, \tag{2.3.5.8}$$

where E_{ox} is the virtual energy in the classical forbidden region of oxide.

2.3.6 Stress-to-Strain Tensor

The stress effect on the warping valance band fundamentally is complex. Instead, we can use approximate simplification to deal with the mechanics of materials such as a general form originating from Hooke's law as below [21]

$$\varepsilon_{xx} = \frac{1}{E}\left[\sigma_{xx} - \nu\left(\sigma_{yy}+\sigma_{zz}\right)\right], \tag{2.3.6.1}$$

$$\varepsilon_{yy} = \frac{1}{E}\left[\sigma_{yy} - \nu\left(\sigma_{xx}+\sigma_{zz}\right)\right], \tag{2.3.6.2}$$

$$\varepsilon_{zz} = \frac{1}{E}\left[\sigma_{zz} - \nu\left(\sigma_{xx}+\sigma_{yy}\right)\right], \tag{2.3.6.2}$$

$$\gamma_{xy} = \frac{1}{G}\tau_{xy},\quad \gamma_{xz} = \frac{1}{G}\tau_{xz},\quad \gamma_{yz} = \frac{1}{G}\tau_{yz}, \tag{2.3.6.3}$$

where σ_{ii} refers to the normal stress component acting on the planes perpendicular to i-direction, while τ_{ij} indicates the shear stress components oriented in the j-direction acting on the planes perpendicular to i-direction, γ_{ij} denotes shear strain, ε_{xx} is average shear strain and is defined as one half the γ_{ij}. E, ν and G represent the Young's modules, Poisson's ratio and shear modulus of elasticity, respectively. We therefore establish the elastic strain-stress matrix as follows [22]

$$\begin{bmatrix} \varepsilon_{xx} \\ \varepsilon_{yy} \\ \varepsilon_{zz} \\ 2\varepsilon_{yz} \\ 2\varepsilon_{zx} \\ 2\varepsilon_{xy} \end{bmatrix} = \begin{bmatrix} S_{11} & S_{12} & S_{12} & 0 & 0 & 0 \\ S_{12} & S_{11} & S_{12} & 0 & 0 & 0 \\ S_{12} & S_{12} & S_{11} & 0 & 0 & 0 \\ 0 & 0 & 0 & S_{44} & 0 & 0 \\ 0 & 0 & 0 & 0 & S_{44} & 0 \\ 0 & 0 & 0 & 0 & 0 & S_{44} \end{bmatrix} \begin{bmatrix} \sigma_{xx} \\ \sigma_{yy} \\ \sigma_{zz} \\ \tau_{yz} \\ \tau_{zz} \\ \tau_{xy} \end{bmatrix}, \tag{2.3.6.4}$$

where S_{11},S_{12} and S_{44} are the elastic stiffness constants. Then, the inverse matrix in Eq. (2.3.6.4) refers to the strain-to-stress tensor written by

$$\begin{bmatrix} \sigma_{xx} \\ \sigma_{yy} \\ \sigma_{zz} \\ \tau_{yz} \\ \tau_{zx} \\ \tau_{xy} \end{bmatrix} = \begin{bmatrix} c_{11} & c_{12} & c_{12} & 0 & 0 & 0 \\ c_{12} & c_{11} & c_{12} & 0 & 0 & 0 \\ c_{12} & c_{12} & c_{11} & 0 & 0 & 0 \\ 0 & 0 & 0 & c_{44} & 0 & 0 \\ 0 & 0 & 0 & 0 & c_{44} & 0 \\ 0 & 0 & 0 & 0 & 0 & c_{44} \end{bmatrix} \begin{bmatrix} \varepsilon_{xx} \\ \varepsilon_{yy} \\ \varepsilon_{zz} \\ 2\varepsilon_{yz} \\ 2\varepsilon_{zx} \\ 2\varepsilon_{xy} \end{bmatrix}. \tag{2.3.6.5}$$

The corresponding relationships between strain and stress under longitudinal, transverse, and out-of-plane stresses in (001) and (110) p-MOSFETs are shown in Fig. 2.2 and 2.3.

2.4 Functions of *p*-NEP

We develop a simulator, *p*-NEP via the six-band $k \cdot p$ Schrödinger-Poisson self-consistent method which can furnish the fundamental information in the first step as follows:

$E(k_x, k_y, k_z)$:bulk valence band structures of heavy hole, light hole, and split-off hole,

$E_\mu^{(0)}$: quantum-confined subband energy level (minimum point) of subband μ,

$E_\mu(k_x, k_y)$: quantum-confined subband structures on k_x-k_y plane of subband μ,

$\xi_0^\mu(z)$: wavefunction at minimum of subband μ,

$DOS_\mu(E)$: density of states of subband μ,

E_f : equilibrium Fermi level,

$P_{inv}^{\mu}(z)$： inversion hole density distribution of subband μ,

$P_{dep}(z)$： density of depleted ionized donors,

$V(z)$： confining electrostatic potential.

Then, the above fundamental outcomes can evaluate the capacitance, threshold voltage, hole mobility, and gate direct tunneling current in the second step by the physical models already discussed before. As to other simulators, the functions and operational range of the updated *p*-NEP are listed in Table 2.1 and 2.2, respectively. Note that the operational range is not equal to the limitation range. The operational range in this table has been verified by the convergent error and reasonable outcomes. The corresponding simulation results will be demonstrated in Chapter 6.

References

[1] E. Bangert, K. von Klitzing, and G. Landwehr, “Self-consistent calculations of electric subbands in p-type silicon inversion layers,” in *Proceedings of the Twelfth International Conference on the Physics of Semiconductors, Stuttgart*, edited by M. H. Pilkuhn (Teubner, Stuttgart, 1974), pp. 714-718.

[2] F. J. Ohkawa and Y. Uemura, “Hartree approximation for the electronic structure of a p-channel inversion layer of silicon M. O. S.,” *Prog. Theor. Phys.*, no. 57, pp. 164-175, 1975.

[3] J. M. Luttinger and W. Kohn, “Motion of electrons and holes in perturbed periodic fields,” *Phys. Rev.*, vol. 97, pp. 869-883, Feb. 1955.

[4] G. L. Bir and G. E. Pikus, “Theory of the deformation potential for semiconductors with a complex band structure,” *Sov. Phys. Solid State*, vol. 2, pp.2287-2300, Sept. 1960.

[5] Y. Sun, S. E. Thompson, and T. Nishida, “Physics of strain effects in semiconductors and metal-oxide-semiconductor field-effect transistors,” *J. Appl. Phys.*, vol. 101, no. 10, p. 104503, May 2007.

[6] R. Kubo, “Statistical-mechanical theory of irreversible process. I.” *J. Phys. Soc. Jpn.*, vol. 12, no. 6, pp. 570-586, Jun. 1957.

[7] D. A. Greenwood, “The Boltzmann equation in the theory of electrical conduction in metals,” *Proc. Phys. Soc. London*, vol. 71, pp. 585-596, 1958.

[8] M. V. Fischetti, “Long-range Coulomb interactions in small Si devices. Part II. Effective electron mobility in thin-oxide structures,” *J. Appl. Phys.*, vol. 89, no. 2, pp. 1232-1250, Jan. 2001.

[9] M. V. Fischetti, Z. Ren, P. M. Solomon, M. Yang, and K. Rim, “Six-band $k \cdot p$

calculation of the hole mobility in silicon inversion layers: Dependence on surface orientation, strain, and silicon thickness," *J. Appl. Phys.*, vol. 94, no. 2, pp. 1079-1095, Jul. 2003.

[10] M. Tiersten, "Acoustic-mode scattering mobility of holes in diamond type semiconductors," *J. Phys. Chem. Solids*, vol. 25, pp. 1151-1168, Nov. 1964

[11] P. Lawaetz, "Low-field mobility and galvanomagnetic properties of holes in germanium with phonon scattering," *Phys. Rev.*, vol. 174, no. 3, pp. 867-880, Oct. 1968.

[12] J. D. Wiley, "Valence-band deformation potentials for the III-V compounds," *Solid State Commun.* vol. 8, no. 22, pp.1865-1868, Nov. 1970.

[13] M. Costato and L. Reggiani, "Scattering probabilities for holes I. deformation potential and ionized impurity scattering mechanisms," *Phys. Status Solidi B*, vol. 58, no. 2, pp. 471-482, Aug. 1973.

[14] A. T. Pham, C. Jungemann, and B. Meinerzhagen, "Modeling of hole inversion layer mobility in unstrained and uniaxially strained Si on arbitrarily oriented substrates," in *Solid State Device Research Conf. ESSDERC*, 2007, pp. 390-393

[15] M. De Michielis, D. Esseni, Y. L. Tsang, P. Palestri, L. Selmi, A. G. O'Neill, and S. Chattopadhyay, "A semianalytical description of the hole band structure in inversion layers for the physically based modeling of pMOS transistors," *IEEE Trans. Electron Devices*, vol. 54, no. 9, pp. 2164-2173, Sept. 2007.

[16] S. Yamakawa, H. Ueno, K. Taniguchi, C. Hamaguchi, K. Miyatsuji, K. Masaki, and U. Ravaioli, "Study of interface roughness dependence of electron mobility in Si inversion layers using the Monte Carlo method," *J. Appl. Phys.*, vol. 79, no. 2, pp. 911-916, Jan. 1996.

[17] F. Gámiz, J. B. Roldán, J. A. López-Villanueva, P. Cartujo-Cassinello, and J. E.

Carceller, “Surface roughness at the Si-SiO$_2$ interfaces in fully depleted silicon-on-insulator inversion layers,” *J. Appl. Phys.*, vol. 86, no. 12, pp. 6854-6863, Dec. 1999.

[18] S. H. Lo, D. A. Buchanan, Y. Taur, and W. Wang, “Quantum-mechanical modeling of electron tunneling current from the inversion layer of ultra-thin-oxide nMOSFET's,” *IEEE Electron Device Lett.*, vol. 18, no. 5, pp. 209–211, May 1997.

[19] L. F. Register, E. Rosenbaum, and K. Yang, “Analytic model for direct tunneling current in polycrystalline silicon-gate metal-oxide-semiconductor devices,” *Appl. Phys. Lett.*, vol. 74, no. 3, pp. 457–459, Jan. 1999.

[20] N. Yang, W. K. Henson, J. R. Hauser, and J. J. Wortman, “Modeling study of ultrathin gate oxides using direct tunneling current and capacitance-voltage measurements in MOS devices,” *IEEE Trans. Electron Devices*, vol. 46, no. 7, pp. 1464–1471, July 1999.

[21] Roy R. Craig, Jr., Mechanics of Materials, second edition, John Wiley & Sons inc., 1999.

[22] H. A. Reuda, “Modeling of mechanical stress in silicon isolation technology and its influence on device characteristics,” dissertation of degree of doctor of philosophy, university of Florida, 1999.

Functions of p–NEP

Material	**Si**	**Ge**	**GaAs**
Wafer Orientation	**(001)** **(110)** ***(111)**		
Stress Condition	**Uniaxial Stress** **Long.** **Trans.** **Out-of-Plane**	**Biaxial Stress**	
Applications	**C : Capacitance** **V_{th} : Threshold Voltage** **μ_p : Inversion-Layer Mobility** **I_g : Gate Direct Tunneling Current**		

∗Stress conditions for (111) wafer orientation have not been completed in p–NEP program.

Table 2.1 The function list of p-NEP. The stress conditions in (111) wafer orientation have not been completed.

Operational Range of *p*–NEP

Ref. Conditions:

Temp.=300K, N_{sub}=1e17 cm^{-3}, F_s=1 MV/cm, Unstressed Si, Ge, and GaAs

<table>
<tr><th></th><th>(001)</th><th>(110)</th><th>(111)</th></tr>
<tr><td>Temperature (K)</td><td colspan="3">2 ↔ 400</td></tr>
<tr><td>N_{sub} (cm^{-3})</td><td colspan="3">1e15 ↔ 6e18</td></tr>
<tr><td>F_s (MV/cm)</td><td>0.01 ↔ 4.5</td><td>0.05 ↔ 4.5</td><td>0.05 ↔ 4.5</td></tr>
<tr><td>Uniaxial Stress (GPa)</td><td colspan="3">-5 ↔ 5</td></tr>
<tr><td>Biaxial Stress (GPa)</td><td colspan="3">-5 ↔ 5</td></tr>
</table>

Table 2.2 The operational range list of *p*-NEP. Note that the operational range is not equal to the limitation range. The operational range in this table has been verified by the convergent error and reasonable outputs.

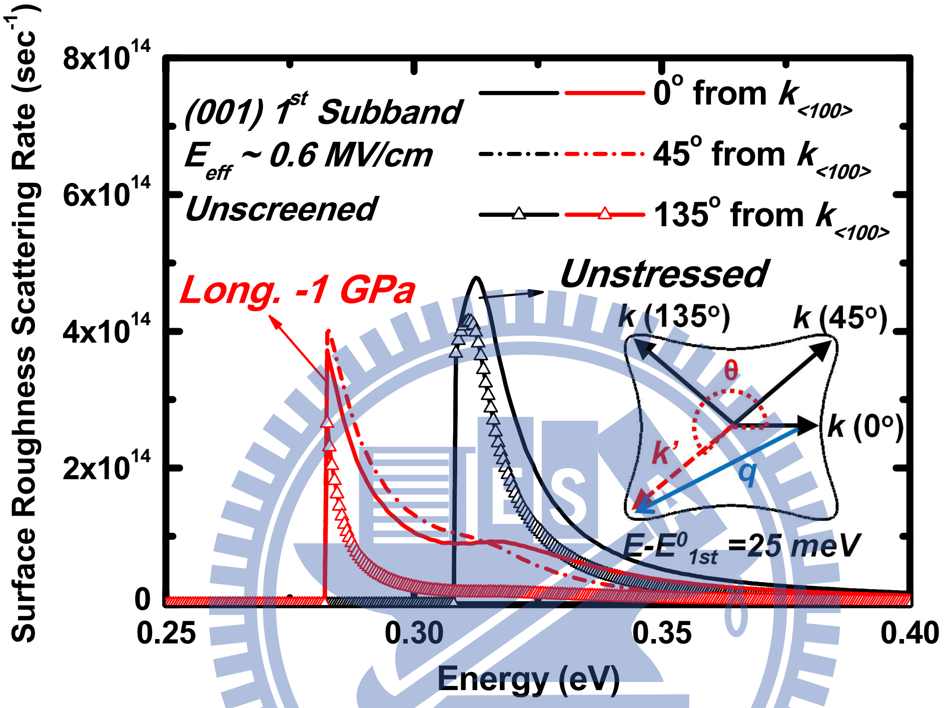

Fig. 2.1(a) Calculated intra-subband surface roughness scattering rate along the different k-direction of the first subband of (001) substrate with the longitudinal -1 GPa stress. The obvious angular dependence can be found in both cases.

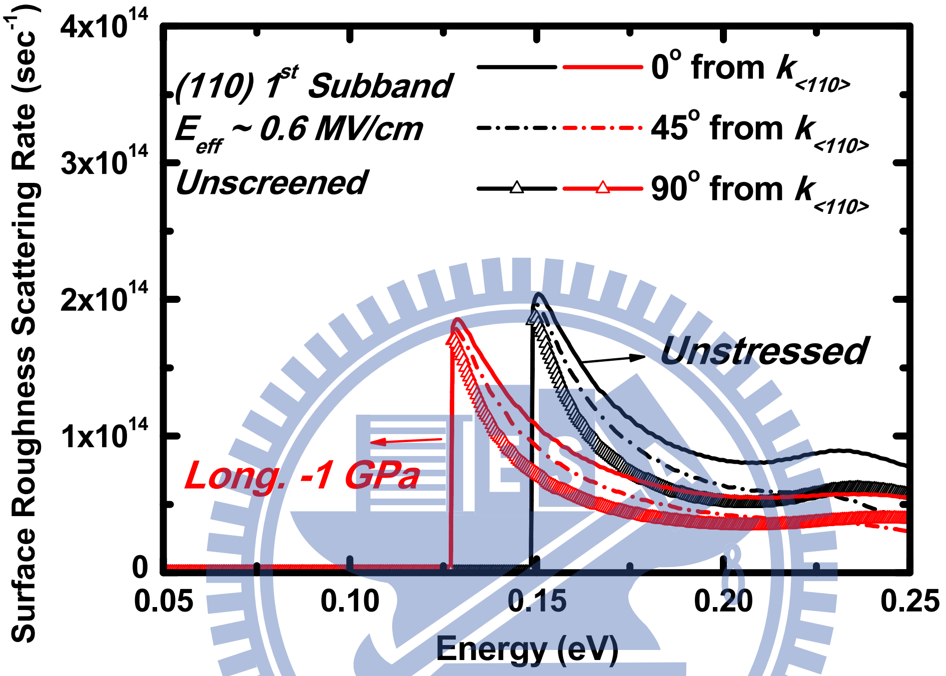

(b)

Fig. 2.1(b) Calculated intra-subband surface roughness scattering rate along the different k-direction of the first subband of (110) substrate with the longitudinal -1 GPa stress. The obvious angular dependence can be found in both cases.

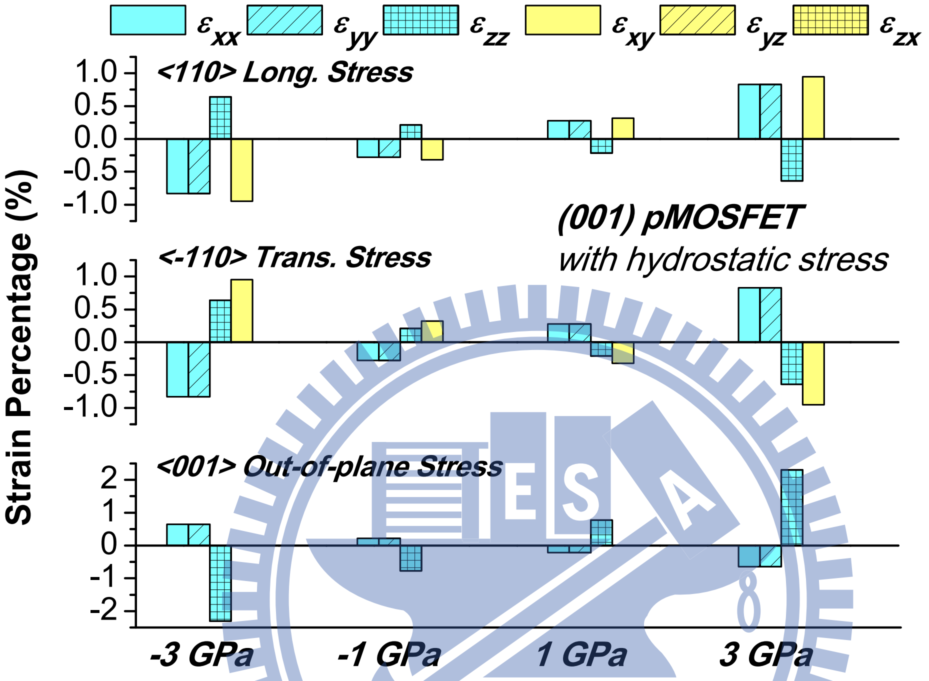

Fig. 2.3 The Bir-Pikus deformation potential parameters are set as a_υ= 2.46, b= -2.1, and d= -4.85, showing the corresponding stress-strain relationships under three-dimensional stresses on (001) p-MOSFET.

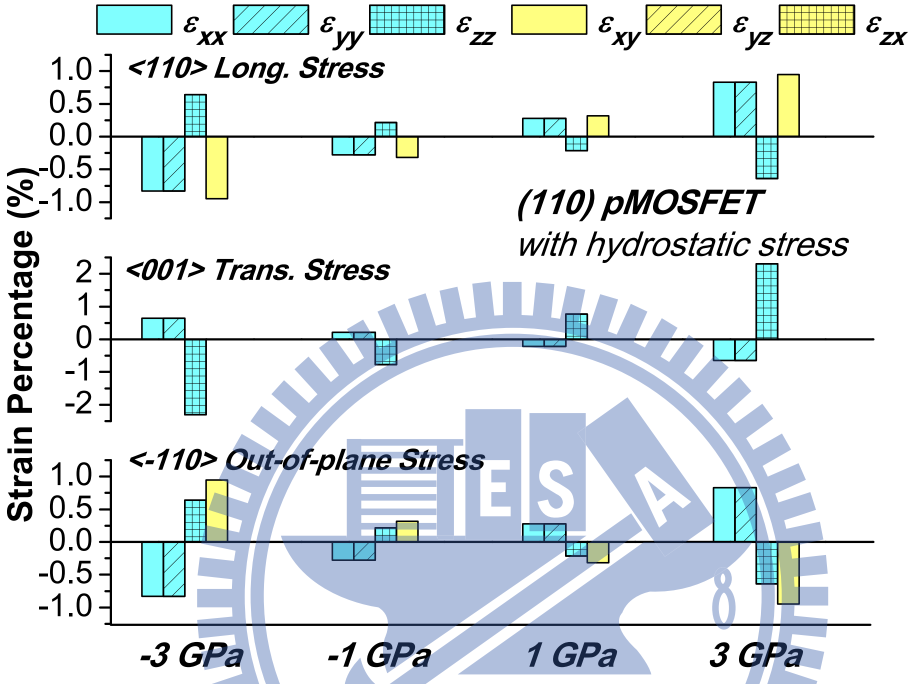

Fig. 2.4 The Bir-Pikus deformation potential parameters are set as a_{υ}= 2.46, b= -2.1, and d= -4.85, showing the corresponding stress-strain relationships under three-dimensional stresses on (110) p-MOSFET.

Chapter 3

Computational Booster in *p*-NEP

3.1 Introduction

As widely recognized, the merits of the effective mass approximation (EMA) in the conduction-band valleys [1] are twofold. First, the computation task to execute a self-consistent Schrödinger and Poisson's equations solving in the inversion layers of nMOSFETs is straightforward [1]. Second, the combination of the resulting subband energy levels and the corresponding electron effective masses can constitute the conduction-band structure in the inversion layers of nMOSFETs [1].

On the other hand, the valence-band structure in the inversion layers of pMOSFETs is quite complicated in terms of the strong anisotropy and non-parabolicity of the hole subbands, as readily described by a six-band $k \cdot p$ method [2] and the original work done by Bangert, von Klitzing and Landwehr [3] and by Ohkawa and Uemura [4]. To simplify the hole subband structure calculation, a triangular potential approximation can be employed [5]. While incorporating the six-band $k \cdot p$ method into the Schrödinger and Poisson's equations to solve the more practical problems, the undertaken numerical calculation becomes so demanding that the overall CPU time is extremely huge, which might prohibit the valence-band structure calculation in a tolerable time. Thus, reducing the CPU time as greatly as possible in the self-consistent six-band $k \cdot p$ framework is absolutely a relevant issue.

Recently, De Michielis, et al. [6] exhibited one such effort in terms of an analytical model for the in-plane energy dispersion, followed by a sophisticated interpolation method by Pham, et al. [7]. However, to produce the hole subband structure as accurately as possible, a very fine discretization in the two-dimensional *k*-space is essential, without accounting for the analytical model [6] or the interpolation method [7]. It is also noticed that Low, et al. [8] explored the effectiveness of one-band EMA in capturing the electrostatics property of six hole bands. Besides, the energy dependence of the hole effective mass was as well taken into account in the development of the analytical model by De Michielis, et al. [6]. Until now, however, the superior ability of the hole EMA to speed up the self-consistent six-band confined $k \cdot p$ calculation was not yet demonstrated as a function of the temperature, the substrate doping concentration, the inversion hole density, and the surface orientation.

In this work, we construct a new computational accelerator to intrinsically boost a self-consistent six-band $k \cdot p$ simulator. A very fine grid in the two-dimensional *k*-space is adopted, without the use of the efficient discretization approach [6],[7]. The core of the accelerator lies in the hole EMA whose formulation, essentially different from those of [6] and [8], can accommodate the use of an electron analogue version of the self-consistent Schrödinger and Poisson's equations solver. In the following sections, we will systematically demonstrate the establishment of the accelerator as well as its ability to overcome the computational burden in the confined $k \cdot p$ simulation.

3.2 Computational Booster

The simulation methodology constructed in this work, as shown in Fig. 1 in terms of a flowchart, consists of the two main blocks: (i) the new computational acceleration and (ii) the self-consistent simulation framework. The connection between the two is the confining potential profile, which is the outcome of the computational accelerator and serves as the input to the subsequent self-consistent simulator. Throughout the work, the energy reference point exactly falls on the classical valence-band edge at the SiO_2/Si interface, as illustrated in Fig. 3.1.

3.2.1 Triangular Potential Based Six-Band $k \cdot p$ Method

In the six-band $k \cdot p$ context, the in-plane wave equation along the quantum confinement direction z can read as depicted in Eq. (2.2.2.1) where $V(z)$ is the confining electrostatic potential, $\xi_{k_x,k_y}(z)$ is the wave function, and E is the energy of holes. The origin z = 0 represents the SiO_2/Si interface. H_{LK} in Eq. (2.2.2.1) is the Luttinger-Kohn Hamiltonian [9] with the split-off energy Δ of 44 meV in the absence of the quantum confinement and with the Luttinger parameters of γ_1 = 4.22, γ_2 = 0.39, and γ_3 = 1.44 [10]. The computational accelerator starts with the initial triangular potential profile: $V^0(z) = F_s^o z$ where F_s^o is the initial surface field. The simulation range of interest in the z direction is divided into a mesh of N_z points in the interval [0, Z_{max}], where Z_{max} is equal to $6E_{max}/\mathrm{q}F_s^o$ for E_{max} = 0.3 eV [5]. Then, Eq. (1) becomes a $6N_z \times 6N_z$ eigenvalue problem. The grid number on k_x-k_y space is 101 × 101 in a Cartesian coordinate system. Also, a polar coordinate system is employed where the grid number on k-θ space is 101 × 101. The boundary conditions are $\xi_{k_x,k_y}(0) = 0$ and $\xi_{k_x,k_y}(Z_{\max}) = 0$. The solution of the eigenvalue problem yields $E(k_x,k_y)$ and normalized $\xi_{k_x,k_y}(z)$. The Fermi level can then be determined. To deal with the (110) case, a rotation transformation from the original (001) k space to (110) k' space is required: $k_x' = -k_z$, $k_y' = \frac{1}{\sqrt{2}}(k_x - k_y)$, and $k_z' = \frac{1}{\sqrt{2}}(k_x + k_y)$. The resulting hole subband energy contours, subband level, and Fermi level on (001) and (110) surface orientations were found to be in good agreements with those of Fischetti, et al. [5].

3.2.2 Hole Effective Mass Approximation Technique

As shown in Fig. 1, the outcomes of the triangular potential based six-band $k \cdot p$ simulator contain the constant-energy contours in k plane, the subband energy levels, the surface potential, and the Fermi level E_f of the system. At this point, we demonstrate how to apply the EMA technique to create the two important parameters in this work: the hole quantization effective mass and the hole *DOS* effective mass. First, the *DOS* function of subband v can be determined in the Cartesian coordinate system [2] by

$$DOS_v(E) = U(E - E_v)\frac{1}{(2\pi)^2} \times \frac{Area_v^{k\text{-}space}(E + dE) - Area_v^{k\text{-}space}(E)}{dE}, \qquad (3.2.2.1)$$

and in the polar coordinate system [5] by

$$DOS_v(E) = U(E - E_v)\frac{1}{(2\pi)^2}\int_0^{2\pi} \frac{K_v(E,\theta)}{\left|\frac{dE}{dK}\right|_{K_v(E,\theta)}} d\theta. \qquad (3.2.2.2)$$

Here, $Area_v^{k-space}(E + dE) - Area_v^{k-space}(E)$ represents the area between the E and $E + dE$ lines of subband v in k plane, E_v is the energy level of subband v, $U(E)$ represents the unit step function of energy, and the magnitude K_v is a function of both the energy E and the angle θ. The *DOS* effective mass of subband v can be obtained accordingly: $m_{DOS}^{v}(E)=2\pi\hbar^{2}\times DOS_{v}(E)$. While averaging the *DOS* effective mass of subband v over the energy, the dependence on hole density distribution must be taken into account:

$$\left\langle m_{\mathrm{DOS}}^{v}\right\rangle=\frac{\int m_{\mathrm{DOS}}^{v}(E)f(E)\cdot DOS_{v}(E)dE}{\int f(E)\cdot DOS_{v}(E)dE}. \qquad (3.2.2.3)$$

where $f(E)$ is the Fermi-Dirac distribution function in equilibrium including the Fermi level E_f. Note that the formalism Eq. (3.2.2.3) is completely different from those of [6] and [8]. As to quantization effective mass of subband v, it can be readily assessed in a triangular potential sense [1]:

$$m_{QN}^{v}=\frac{\hbar^{2}}{2}\left(E_{v}^{(0)}\right)^{-3}\left(\frac{3}{2}\pi eF_{S}^{0}\left(j+\frac{3}{4}\right)\right)^{2}, \qquad (3.2.2.4)$$

where j reflects the status of the wave function at subband minimum (for example, j = 0 for the ground state and 1 for the first excited state). Note that under the quantum confinement conditions, E_5 and E_6 in Eq. (3.2.2.4) no longer refer to the pure (bulk) split-off holes due to the mixing with a fraction of light holes. In other words, E_5 and E_6 should be seen as individual subbands with respect to the classical reference point, rather than to the bulk split-off energy point (situated 44 meV away), when calculating the quantization effective mass. Both the Cartesian and polar coordinate systems led to the nearly same results. Thus, throughout the work, the Cartesian coordinate system is adopted, unless mentioned otherwise. The resulting $\left\langle m_{DOS}^{v}\right\rangle$ and m_{QN}^{v} versus initial surface field are depicted in Fig. 3.2 for subband v = 1 to 6 and Fig. 3.3 for v = 1 with different temperatures.

3.2.3 Core Accelerator

Analogous to the electron counterparts [11],[12], the simple EMA oriented Schrödinger-Poisson iterative solving can readily be employed using the aforementioned hole effective masses. First, the Schrödinger equation in pMOSFETs can be written accordingly:

$$\left[-\frac{\hbar^2}{2m_{QN}^{v}}\frac{d^2}{dz^2}+eV(z)\right]\phi(z)=E\phi(z). \tag{3.2.3.1}$$

The energy level $E_{v,j}$ of sub-subband j within subband v and the corresponding normalized wave function $\phi_{v,j}(z)$ can be obtained by solving the eigen-problem in Eq. (3.2.3.1). Also in analogue, the expression of the hole density in 2DHG case becomes

$$p(z)=\sum_{v,j}\frac{\left\langle m_{DOS}^{v}\right\rangle}{2\pi\hbar^2}k_BT\ln\left(1+\mathrm{e}^{\frac{E_f-E_{v,j}}{kT}}\right)\cdot\left|\phi_{v,j}(z)\right|^2. \tag{3.2.3.2}$$

The EMA oriented Schrödinger-Poisson iterative solving in pMOSFETs can therefore be expected to be as fast as nMOSFETs. The Fermi level is determined in the self-consistent loop, given the surface band bending and substrate doping concentration. The calculation results have been corroborated using the available simulator Schred [11].

As mentioned above, the calculated hole quantization and DOS effective masses contain the information about the anisotropy and non-parabolicity of the subbands. The outcome of the EMA oriented Schrödinger-Poisson iterative solving, which is the initial solution of the confined potential profile as illustrated in Fig. 3.1, is likely to be close to the realistic one. Consequently, a fast convergence in the subsequent self-consistent six-band $k \cdot p$ simulation can be ensured. This is the fact, as will be proved later.

3.3 Results and Discussions

To confirm the validity of the whole simulation methodology in Fig. 3.1, we quote the existing self-consistent six-band $k \cdot p$ simulation results [6], [8]. First, in our work, the following convergence criteria were set for the self-consistent six-band $k \cdot p$ simulator: (i) below 1% error for the surface field and (ii) 10^{-4} V maximum error for the confining electrostatic potential profile. Besides, the grid number N_z was set at 301.

Fig. 3.4 depicts the comparison of the simulated subband energy level on (001) substrate versus inversion-layer hole density with that of De Michielis, et al. [6]. Good agreement is achieved. This is also the case in comparison with those of Low, et al. [8], as given in Fig. 3.5 for the subband level and surface potential versus the surface field F_s. A small deviation of split-off hole (SH) subbands in Fig. 3.4 and 3.5(a) is due to the fact that the subband level in this work represents the energy minimum rather than the gamma point. Further evidence exists in terms of the simulated DOS results, as shown in Fig. 3.6 for (001) and (110) substrates. Evidently, excellent agreements with those from different sources [6], [8] are obtained. Particularly, a careful observation leads to the argument that under the same grid number, the simulated DOS in a polar coordinate system is less "noisy" than the Cartesian one, as expected from the numerical analysis point of view.

More importantly, we found that relative to the conventional self-consistent six-band $k \cdot p$ simulation without the accelerator, the whole computational time with the accelerator included can be substantially reduced. First of all, the simulation methodology in Fig. 3.1 can reduce to the conventional self-consistent six-band $k \cdot p$ simulator only, achieved by simply removing the accelerator part. The CPU time consumed with and without the accelerator is plotted in Fig. 3.7 for (001) and (110) substrates. Interestingly, with the accelerator added, the overall CPU time is reduced down to around 8% of that without the accelerator for (001) substrate and 17% for (110) substrate. Note that the relatively large computational time in this work as compared with that of [7] is due to a larger mesh number in both k space (101×101) and z direction (N_z =301), as well as the lower hardware level and operating system. Further, we found that in all (001) cases under study, no iteration can be needed in the self-consistent six-band $k \cdot p$ simulator of the methodology. This means that the confining electrostatic potential created by the accelerator is in a close proximity of the realistic one, as shown in the inset of Fig. 3.7(a). Even for (110) case in Fig. 3.7(b), only one iteration step is needed to make the specific error satisfied. This explains a slight increase in the CPU time compared to (001) case.

In addition, we present in Fig. 3.8 the enhancement factor of the computational speed as a function of the doping concentration in the substrate while keeping the same inversion carrier density. Also shown is the corresponding CPU time with and without the accelerator. Obviously, the speed enhancement slightly decreases with increasing doping concentration. The increased calculation time as found in the fully self-consistent algorithm itself with increasing doping concentration is primarily due to the nature of solving six-band $k \cdot p$ Schrödinger equation (with the same iteration steps). On the contrary, the increased calculation time in the accelerator-enhanced algorithm is mainly consumed in the triangular potential based six-band $k \cdot p$ Schrödinger solver. The larger increasing rate of calculation time in the accelerator-enhanced algorithm leads to the observed trend of the speed enhancement. We also examine the convergence quality in this work in terms of the errors encountered in the self-consistent simulation part (without any iteration), as shown in Fig. 3.9 for (001) substrate plotted versus the inversion hole density with the temperature as a parameter. It is clear that not only the surface field errors but also the potential errors are all far below the corresponding critical errors of 1% and 10^{-4} V, respectively, valid for the temperature and inversion-layer hole density range demonstrated. This thereby serves as the corroborating evidence that no Gummel type iteration can be needed in the (001) self-consistent six-band $k \cdot p$ simulation. However, further analysis as depicted in Fig. 3.10 reveals that if the more strict convergence criterion is set, additional Gummel iterations may be requested in order to further reduce the errors. In other words, the lower the order of tolerable error, the more iteration steps needed. Thus, there is a trade-off between the convergence criterion and the efficiency of the proposed accelerator. However, we want to emphasize that the convergence error of 10^{-4} V as adopted in this work is adequate. This point can be highlighted in Fig. 3.11 in terms of the fitting of the experimental gate capacitance versus gate voltage curve [13]. Evidently, the fitting quality with the convergence criterion of 10^{-4} V is acceptable, especially in the weak inversion region where the gate capacitance changes sharply with the gate voltage.

3.4 Projection

At this point, two key points can be drawn. First, the initial solution of the confining potential profile as close to the realistic one as possible is the key to eliminating or reducing the conventionally required Gummel type iteration steps in the self-consistent six-band $k \cdot p$ simulation. Thus, the CPU time can be substantially lowered. Second, the ability to create such potential profile in advance is the main merit of the proposed hole EMA based accelerator. Moreover, we want to stress that the hole EMA based accelerator introduced in this work is simple and feasible. Thus, we can make a projection of the accelerator concerning its general applications.

First, the proposed accelerator can accommodate the strained p-MOSFETs case, achieved by incorporating the strain Hamiltonian H_{strain} [5],[14] in the $k \cdot p$ context. Contrary to the unstrained case, the quantization effective mass extraction in Eq. (3.2.2.4) should be replaced when the strain effect will be taken into account by the follows

$$m_{QN}^{\nu} = \frac{\hbar^2}{2}\left(E_{\nu}^{(0)} - E_{\nu}^{Bulk}\right)^{-3}\left(\frac{3}{2}\pi e F_S^0\left(j+\frac{3}{4}\right)\right)^2, \tag{3.4.1}$$

where E_{ν}^{Bulk} refers to the bulk valence band (HH, LH, or SH) of the most occupied hole type in subband ν. The modified method in Eq. (3.4.1) can extract the more meaningful quantization effective mass to prevent the unreasonable results from the huge strain-induced bulk band shift. The unstrained and strained quantization effective masses extracted by Eq. (3.4.1) are shown together in Fig. 3.12. Second, to deal with the ultra-thin film device adequately, a higher order $k \cdot p$ framework, such as the eight-band $k \cdot p$ one (see [15] for the comparison with the six-band one), may be needed to replace the six-band one in the methodology in Fig. 3.1. In this case, the space-induced confinement formula may be required rather than the field induced one (that is, triangular potential well) in this work. Note that the wave function penetration into the oxide was not taken into account here. However, this issue is considerably important, especially for the ultra-thin film case. The effect of the wave function penetration on the applicability of the proposed accelerator, as well as the possible modification of the accelerator, needs to be further investigated. Finally, the additional issues of other surface orientations or channel materials, which were not addressed in this work, should in principle be able to benefit from the proposed accelerator.

References

[1] F. Stern, "Self-consistent results for n-type Si inversion layers," *Phys. Rev. B,* vol. 5, no. 12, pp. 4891-4899, Jun. 1972.

[2] R. Oberhuber, G. Zandler, and P. Vogl, "Subband structure and mobility of two-dimensional holes in strained Si/SiGe MOSFETs," *Phys. Rev. B,* vol. 58, no. 15, pp. 9941-9948, Oct. 1998.

[3] E. Bangert, K. von Klitzing, and G. Landwehr, "Self-consistent calculations of electric subbands in p-type silicon inversion layers," in *Proceedings of the Twelfth International Conference on the Physics of Semiconductors*, *Stuttgart*, edited by M. H. Pilkuhn (Teubner, Stuttgart, 1974), pp. 714-718.

[4] F. J. Ohkawa and Y. Uemura, "Hartree approximation for the electronic structure of a p-channel inversion layer of silicon M. O. S.," *Prog. Theor. Phys*., no. 57, pp. 164-175, 1975.

[5] M. V. Fischetti, Z. Ren, P. M. Solomon, M. Yang, and K. Rim, "Six-band $k \cdot p$ calculation of the hole mobility in silicon inversion layers: Dependence on surface orientation, strain, and silicon thickness," *J. Appl. Phys.*, vol. 94, no. 2, pp. 1079-1095, Jul. 2003.

[6] M. De Michielis, D. Esseni, Y. L. Tsang, P. Palestri, L. Selmi, A. G. O'Neill, and S. Chattopadhyay, "A semianalytical description of the hole band structure in inversion layers for the physically based modeling of pMOS transistors," *IEEE Trans. Electron Devices*, vol. 54, no. 9, pp. 2164-2173, Sept. 2007.

[7] A. T. Pham, B. Meinerzhagen, and C. Jungemann, "A fast $k \cdot p$ solver for hole inversion layers with an efficient 2D *k*-space discretization," *J. Comput. Electron.,* vol. 7, no. 3, pp. 99-102, Dec. 2008.

[8] T. Low, Y. T. Hou, and M. F. Li, "Improved one-band self-consistent effective

mass methods for hole quantization in p-MOSFET," *IEEE Trans. Electron Devices*, vol. 50, no. 5, pp. 1284-1289, May 2003.

[9] J. M. Luttinger and W. Kohn, "Motion of electrons and holes in perturbed periodic fields," *Phys. Rev.*, vol. 97, no. 4, pp. 869-883, Feb. 1955.

[10] P. Lawaetz, "Valence-band parameters in cubic semiconductors," *Phys. Rev. B,* vol. 4, no. 10, pp.3460-3467, Nov. 1971.

[11] Schred, http://nanohub.org/resources/schred.

[12] D. Vasileska, D. K. Schroder, and D.K. Ferry, "Scaled silicon MOSFET's: Degradation of the total gate capacitance," *IEEE Trans. Electron Devices*, vol. 44, no.4, pp. 584-587, April 1997.

[13] K. N. Yang, H. T. Huang, M. C. Chang, C. M. Chu, Y. S. Chen, M. J. Chen, Y. M. Lin, M. C. Yu, S. M. Jang, D. C. H. Yu, and M. S. Liang, "A physical model for hole direct tunneling current in P^+ poly-gate PMOSFETs with ultrathin gate oxides," *IEEE Trans. Electron Devices*, vol. 47, no. 11, pp. 2161-2166, Nov. 2000.

[14] Y. Sun, S. E. Thompson, and T. Nishida, "Physics of strain effects in semiconductors and metal-oxide-semiconductor field-effect transistors," *J. Appl. Phys.*, vol. 101, no. 10, p. 104503, May 2007.

[15] T. Low, M. F. Li, Y. C. Yeo, W. J. Fan, S. T. Ng, and D. L. Kwong, "Valence band structure of ultrathin silicon and germanium channels in metal-oxide-semiconductor field-effect transistors," *J. Appl. Phys.*, vol. 98, no. 2, p. 024504, July 2005.

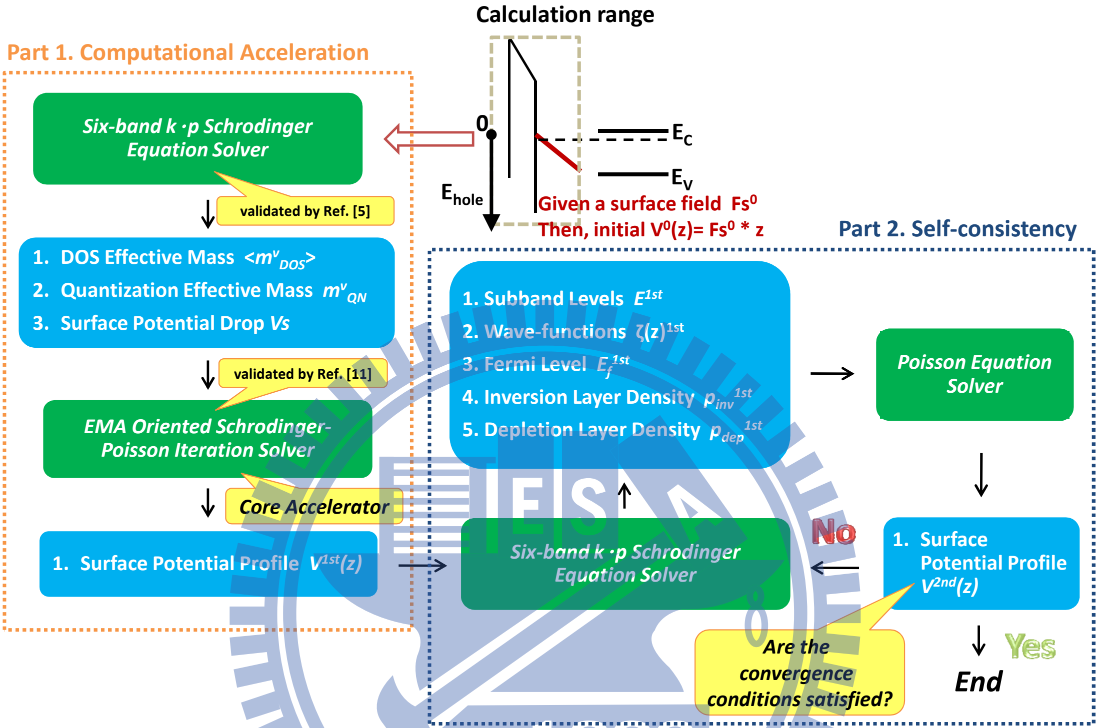

Fig. 3.1 The flowchart of the simulation methodology in the inversion layer of pMOSFET. The methodology consists of two parts: the computational acceleration part in order to enhance the convergence speed and the self-consistent part in order to certify the tolerable error. The green blocks refer to the simulation methodology and the turquoise blocks refer to the outputs from the upper level simulator.

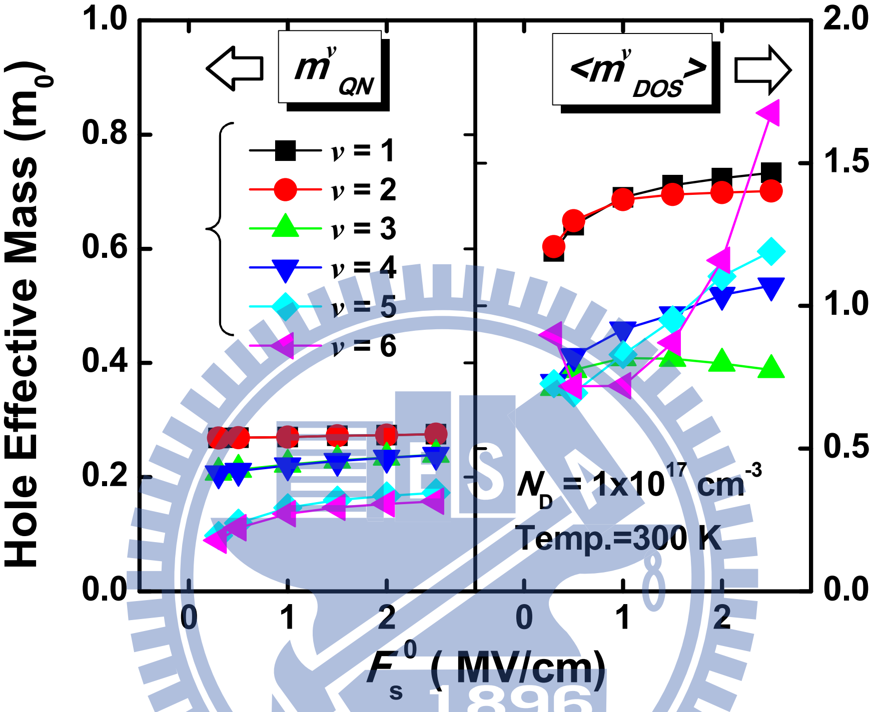

Fig. 3.2 The calculated hole quantization effective masses and DOS effective masses versus initial surface field in the simulation flowchart in Fig. 3.1.

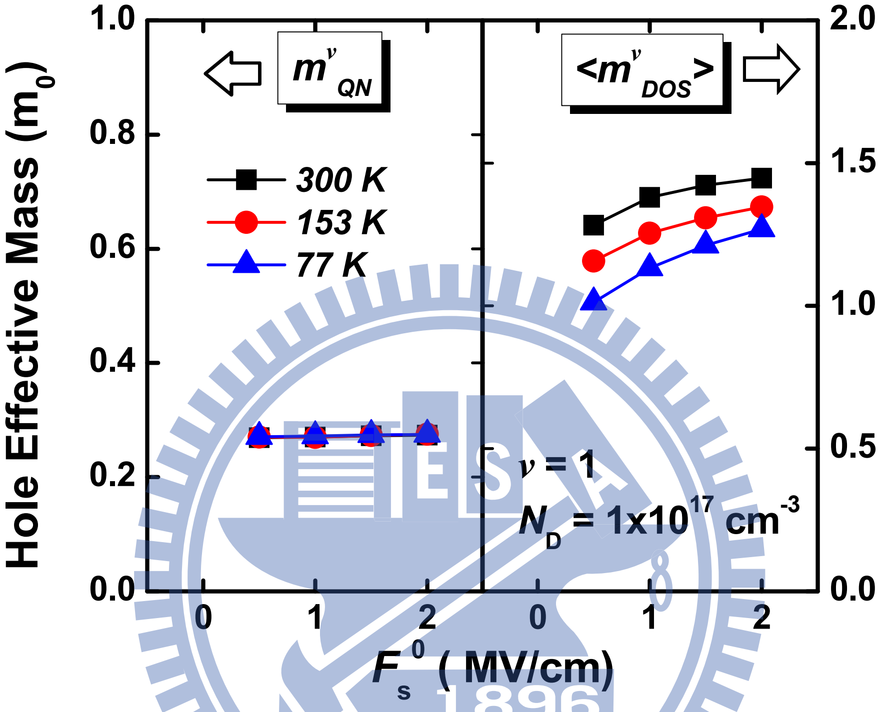

Fig. 3.3 The calculated hole quantization effective masses and DOS effective masses versus initial surface field for different temperatures of 77, 153, and 300 K in the simulation flowchart in Fig. 3.1.

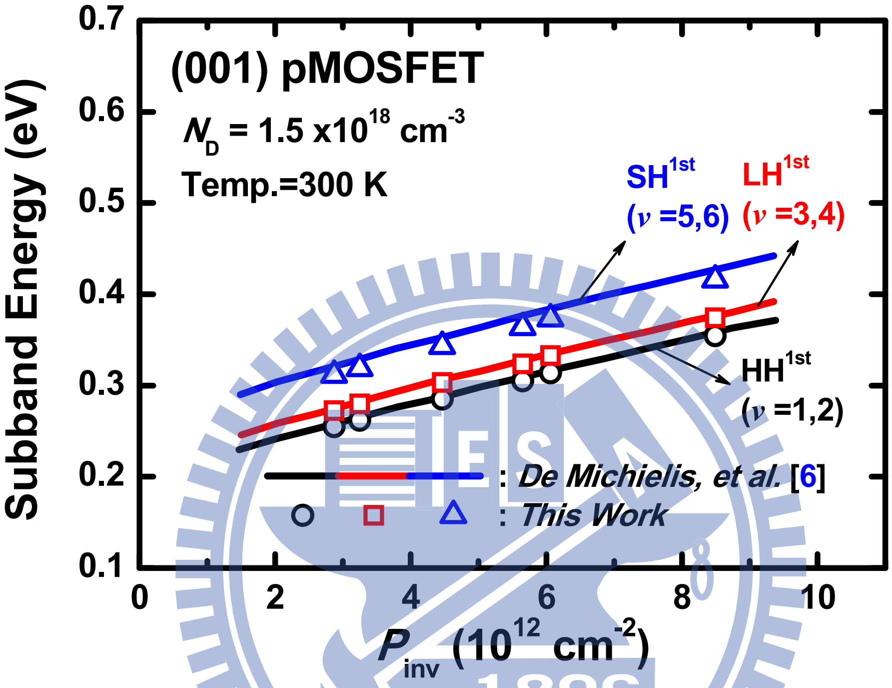

Fig. 3.4 Calculated (symbols) hole subband energy levels versus inversion carrier density on (001) surface. The solid lines come from De Michielis, et al. [6] for comparison.

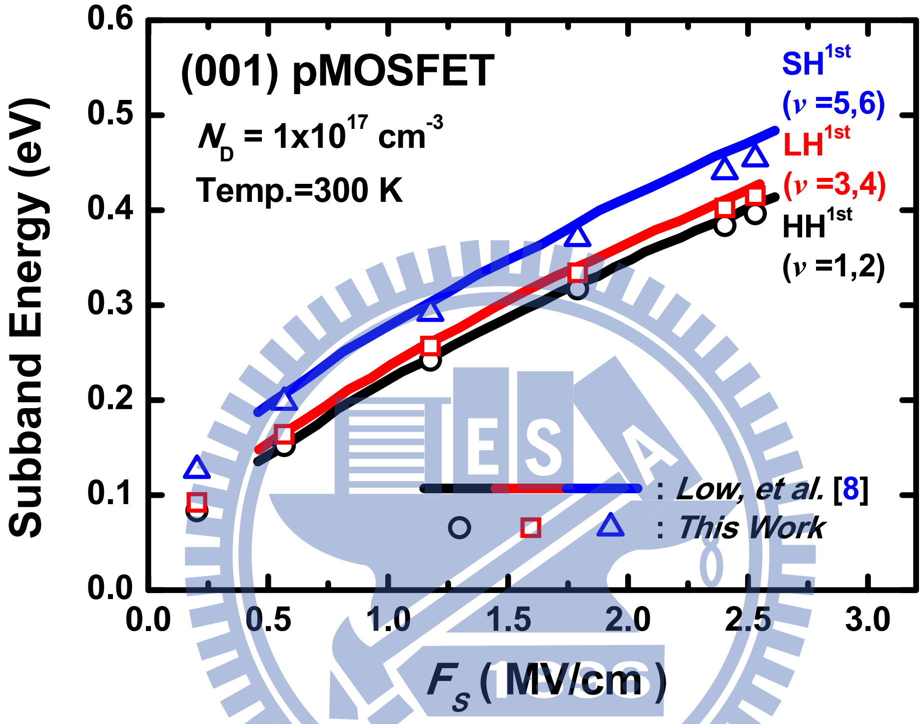

Fig. 3.5(a) Calculated (symbols) hole subband energy levels versus surface field on (001) substrate. The solid lines come from Low, et al. [8] for comparison.

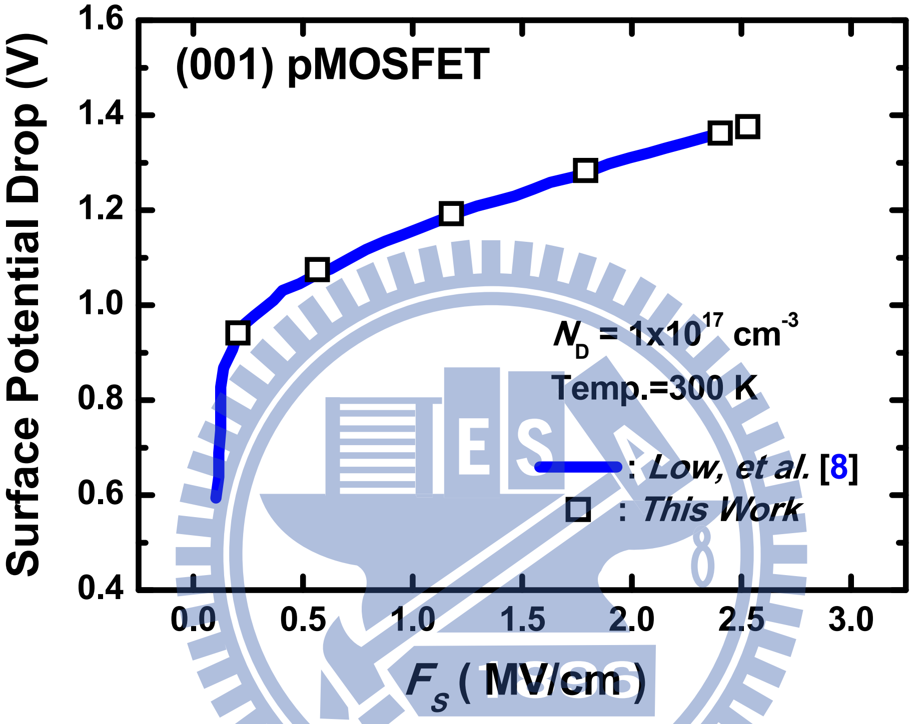

Fig. 3.5(b) The corresponding surface potential versus surface field.

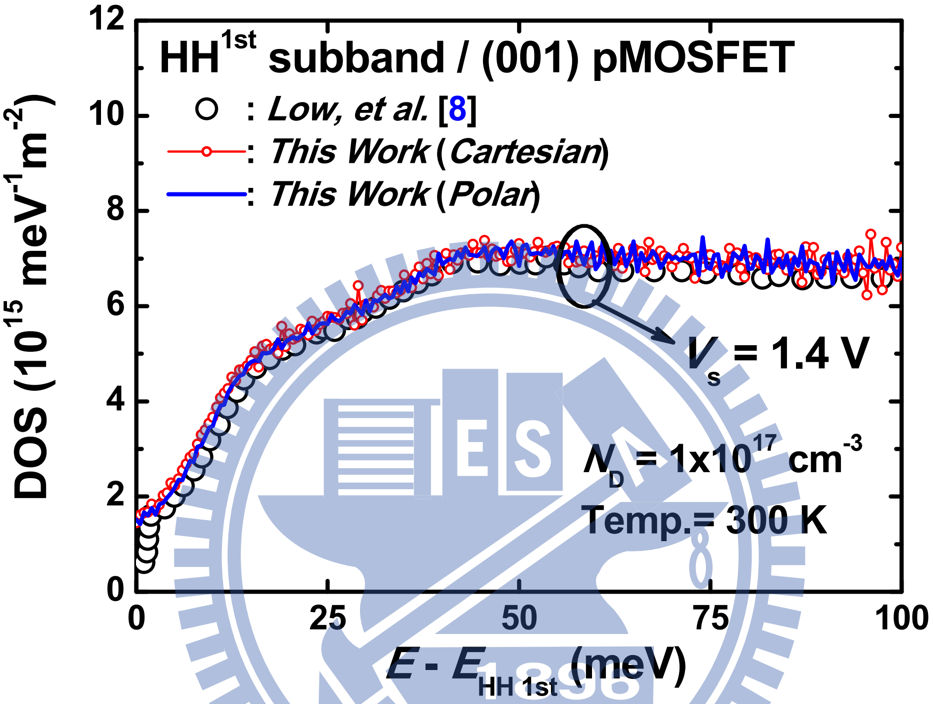

Fig. 3.6 (a) Simulated DOS function for the first subband on (001) substrate in our work. The red and green solid lines are produced from the Cartesian and polar coordinate systems, respectively. The dotted line comes from [8] from comparison.

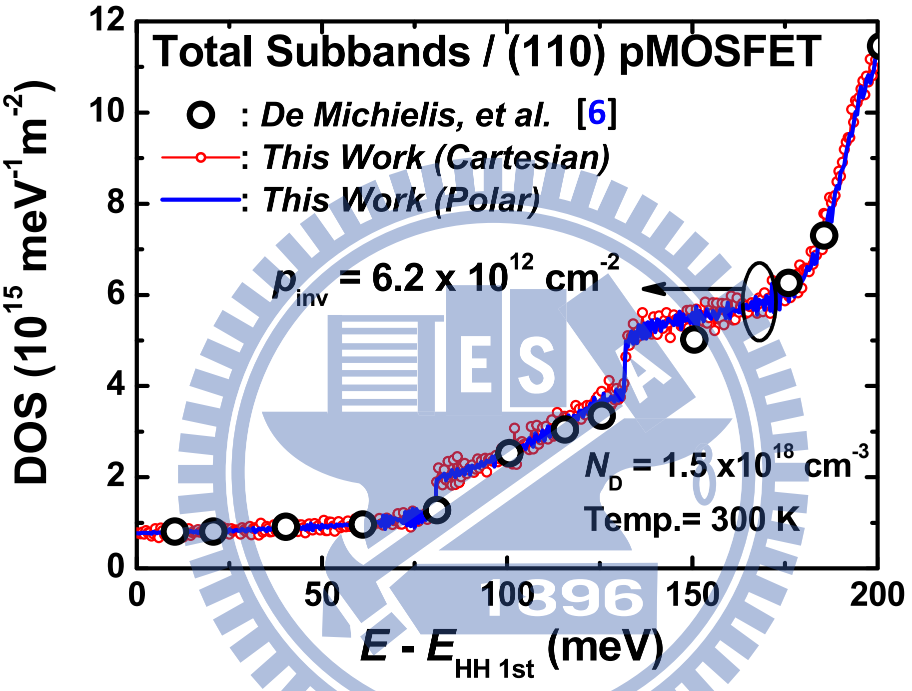

Fig. 3.6(b) Simulated DOS function for the total subbands on (110) substrate. The red and green solid lines are produced from the Cartesian and polar coordinate systems, respectively. The dotted line comes from [6].

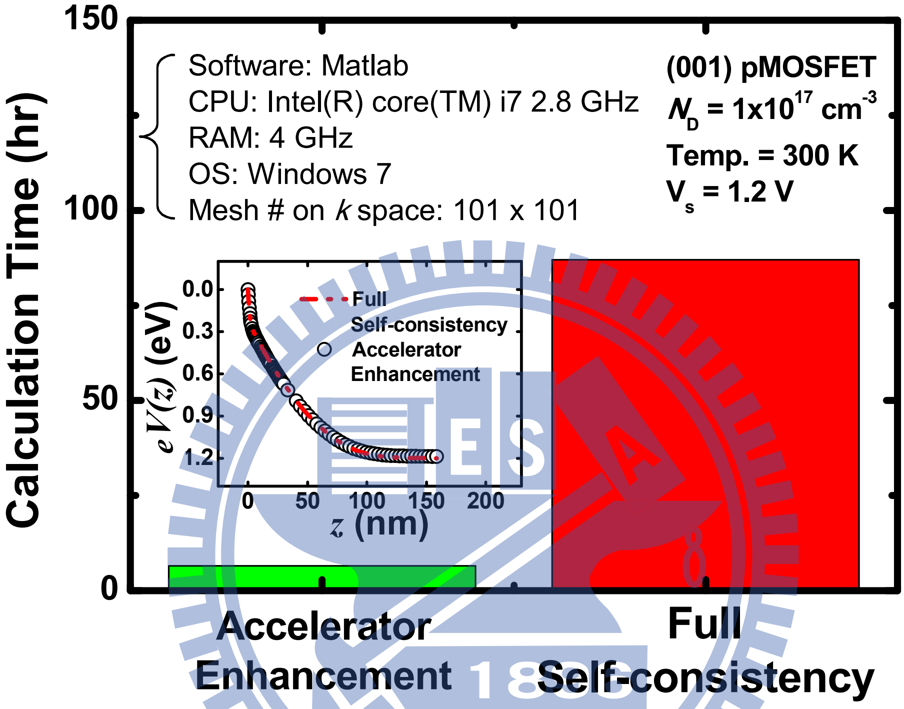

Fig. 3.7(a) Comparison of the CPU time between the accelerator enhanced methodology and the fully self-consistent methodology without the accelerator on (001) substrate. The inserted figure shows the corresponding electrostatic potential profiles.

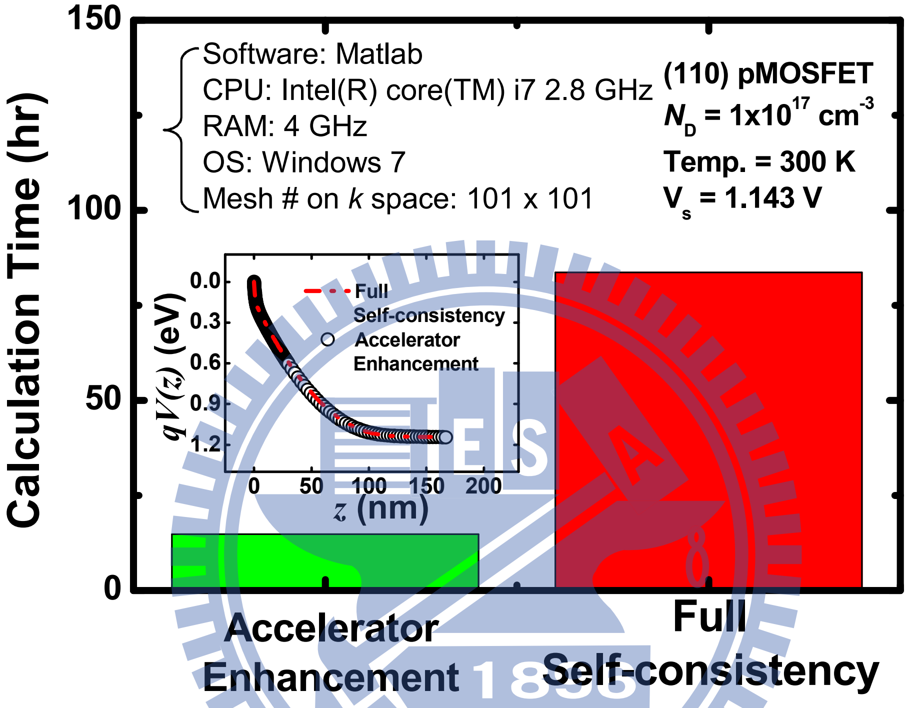

Fig. 3.7(b) Comparison of the CPU time between the accelerator enhanced methodology and the fully self-consistent methodology without the accelerator on (110) substrate. The inserted figure shows the corresponding electrostatic potential profiles.

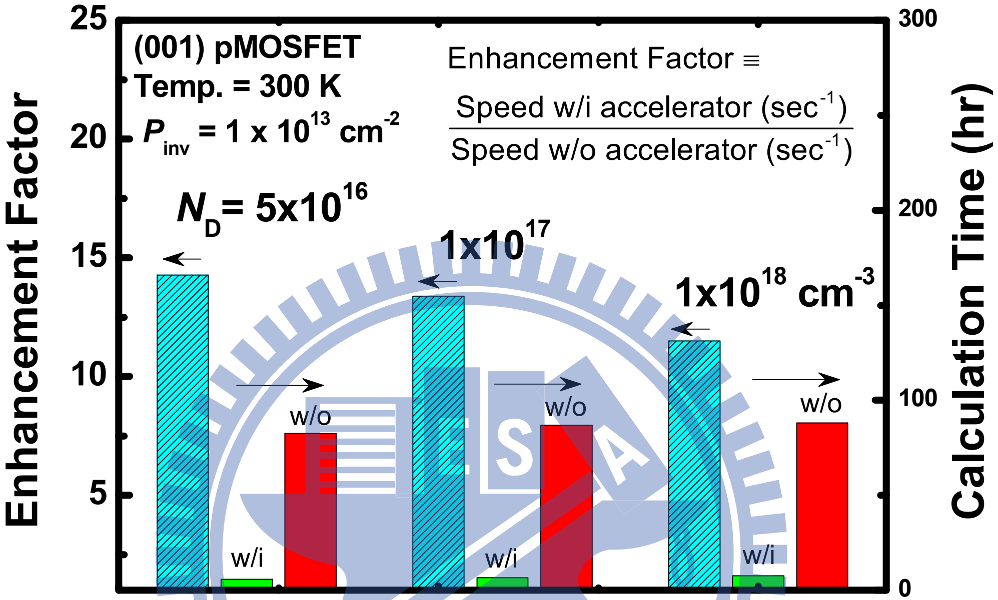

Fig. 3.8 Computational enhancement factor on (001) substrate versus the substrate doping concentration under the same inversion hole density of 1×10^{13} cm^{-2}. Also shown are the corresponding CPU time with and without the accelerator.

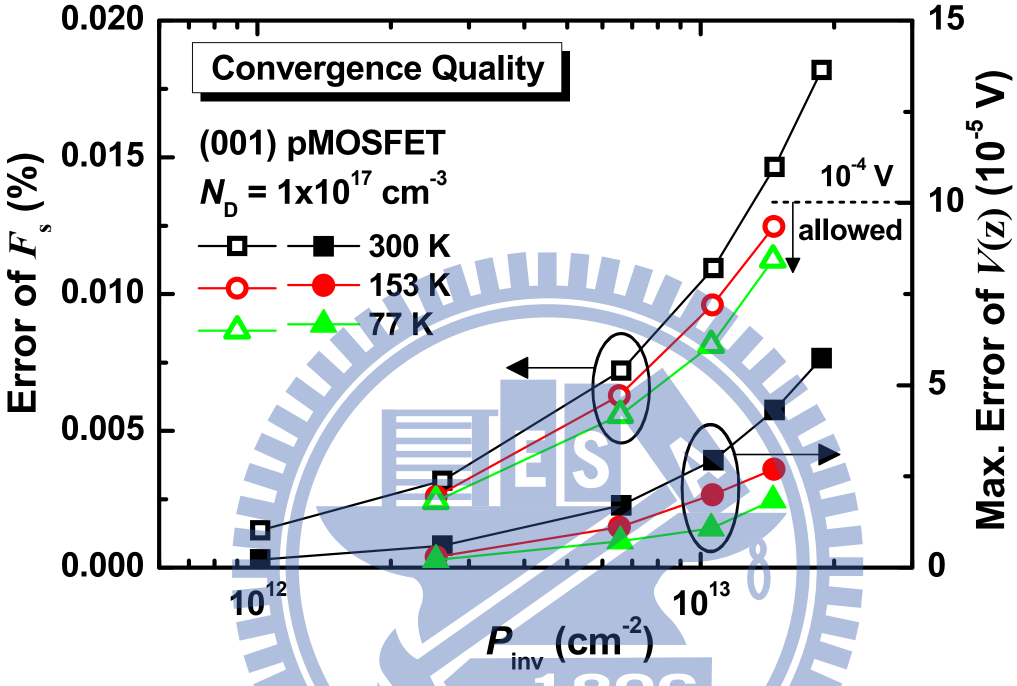

Fig. 3.9 The convergence quality on (001) substrate versus surface field at 77, 153, and 300 K. The convergence conditions in this work are: (i) below 1% error for the surface field and (ii) 10^{-4} V maximum error for the confining electrostatic potential profile.

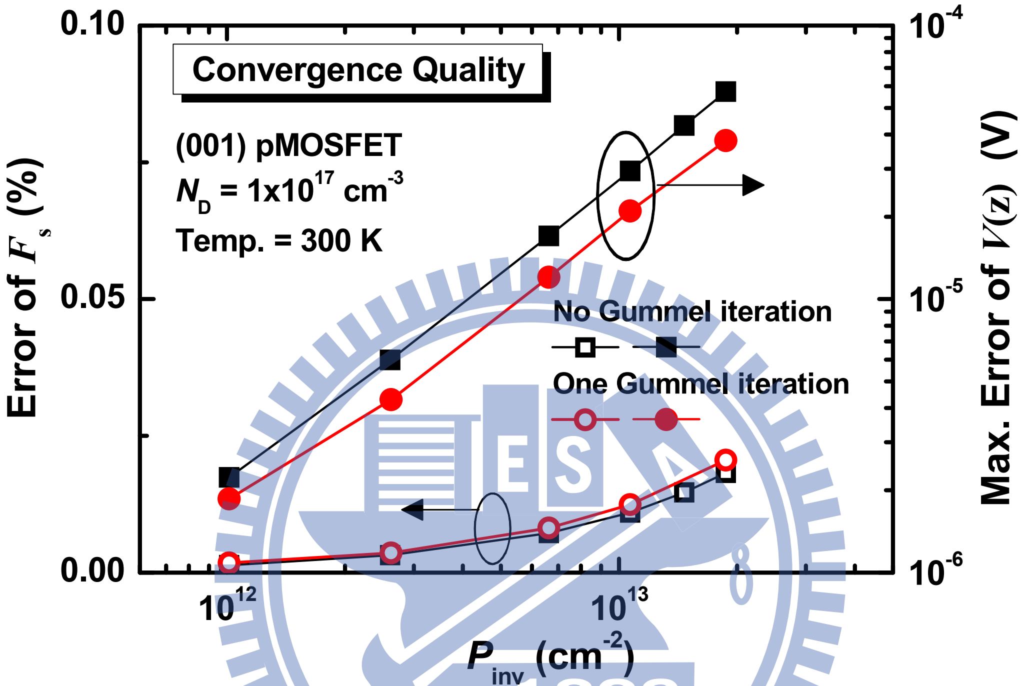

Fig. 3.10 Comparison of the convergence quality having no Gummel iteration and that with the additional Gummel iteration, plotted as a function of the inversion hole density on (001) substrate at 300 K.

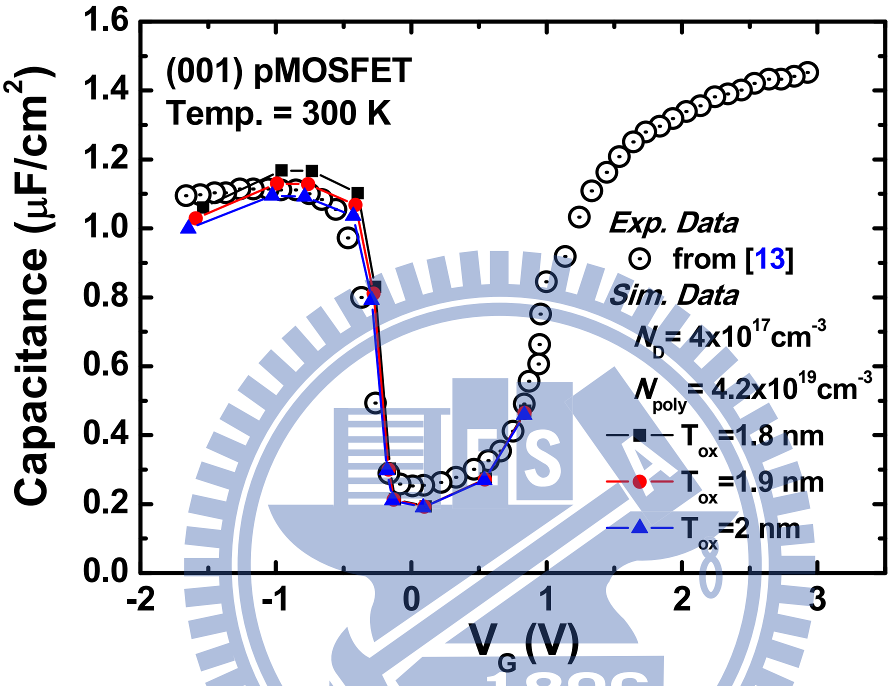

Fig. 3.11 Comparison of the experimental gate capacitance versus gate voltage curves [13] and those (only in weak inversion and strong inversion region) simulated with the convergence criterion of 10^{-4} V for the confining potential. From the HRTEM image [13], the nominal physical gate oxide thickness is 1.89 nm. However, in the simulation, three different physical gate oxide thicknesses were used to testify the validity of the chosen convergence criterion in this work.

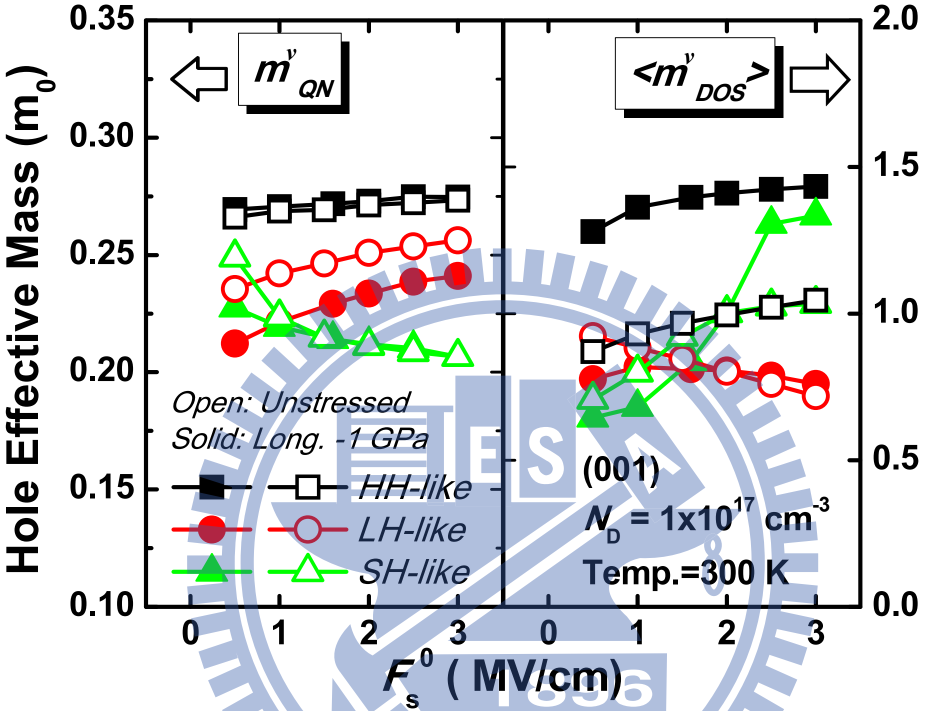

Fig. 3.12 The calculated hole quantization effective masses and DOS effective masses versus initial surface field under unstressed and longitudinal -1 GPa stresses through the modified Eq. (3.4.1). The subbands are simply sorted by the most occupied hole type (heavy-hole-like, light-hole-like, and split-off-hole-like) in each subband.

Chapter 4

Hole Band Structure and Inversion-Layer Mobility Calculation at 2 K

4.1 Introduction

It has been well recognized that the Schrödinger-Poisson self-consistent $k \cdot p$ method (6×6 Luttinger-Kohn matrix) can be used as a tool to quantify the hole subband structures in the inversion layers of p-MOSFETs on (001), (110) or (111) oriented surfaces [1]. The core of this $k \cdot p$ method lies on the Luttinger parameters γ_1, γ_2, and γ_3. The literature value of $(\gamma_1^0, \gamma_2^0, \gamma_3^0) = (4.22, 0.39, 1.44)$ stemmed from the analysis of the momentum matrix elements on *bulk* silicon according to Lawaetz [2]. The other two sets of Luttinger parameters mentioned by Humphreys [3] were also widely used in silicon valence band calculation. All of them are listed in Table 4.1. However, the validity of these parameters remained unclear for the extra confinement originating from the surface electrostatic potential $V(z)$ in p-MOSFETs. Recently, while conducting the Shubnikov-de Haas (SdH) oscillation experiment down to 2 K, Takahashi, et al. [4] for the first time directly observed the realistic subband structures of (110) p-MOSFETs. This experiment provides a good opportunity to delicately study the subband structures of two-dimensional hole gas (2DHG) via the self-consistent six-band $k \cdot p$ Schrödinger-Poisson simulation.

In this work, the experimentally constructed hole subband structures [4] will be used to examine the validity of the $k \cdot p$ method in 2DHG, especially the bulk oriented Luttinger parameters.

4.2 γ_1, γ_2, and γ_3 Examination

Simulator *p*-NEP with the six-band $k \cdot p$ Schrödinger-Poisson self-consistent method was utilized in this work. The validation of *p*-NEP was confirmed in the previous chapter. In particular, the calculated DOS function of (110) p-MOSFET at 300 K as shown in Fig. 3.6(b) is nearly a constant DOS function of the 1st subband. It means it possible to the detectable proper switching when Fermi level crosses the 2nd subband at low temperatures. In terms of the recent experimental results in [4], there are five important measured values to determine the *realistic* hole subband structures at 2 K as illustrated in Fig. 4.1: two threshold voltages which are denoted as V_{th}^{L} (*L* for the first subband) and V_{th}^{H} (*H* for the second subband) obtained by Shubnikov-de Haas (SdH) oscillation analysis, one surface carrier density (N_{s}) at V_{th}^{H} bias condition obtained by *C*-*V* measurement, and two cyclotron effective masses m_{c}^{L} and m_{c}^{H}.

Then, the calculated solutions must satisfy two measured cyclotron effective masses, $m_{\mathrm{c}}^{L} = 0.26m_0$, and $m_{\mathrm{c}}^{H} = 0.43m_0$, meanwhile consistent with the experimental $V_{\mathrm{th}}^{L} = -1.2$ V, $V_{\mathrm{th}}^{H} = -2.3$ V, and $N_{\mathrm{s}} = 4 \times 10^{12}$ cm^{-2}. In advance, the low temperature validity of *p*-NEP preliminarily confirmed by the simulated capacitance from Schred [5] and by the experimental hole effective mobility [6] are shown in Fig. 4.2 and Fig. 4.3 respectively. To examine the validity of the bulk oriented Luttinger parameters in 2DHG, the subband structures reproduced by the γ_1^0, γ_2^0, and γ_3^0 at 2 K are shown in Fig. 4.4 with the five crucial calculated values mentioned above. The quite satisfactory comparisons between the calculated values and experimental data [4] are obtained. The transition region from the first subband to the second subband which is probably due to the Fermi level fluctuation is also marked in Fig. 4.4 by comparing the experimental transconductance data in [4]. In order to see the γ modulation effect on subband structures, we modulate the γ_1^0, γ_2^0, and γ_3^0 in Luttinger-Kohn matrix within the broad range of $\pm 20\%$ which is based on the error range of the factors A, B, and C appearing in the analytical energy surface model expressed by Dresselhaus [7]. To efficiently quantify the impact of γ modulation, the triangular potential approximation is used in Fig. 4.5, 4.6, and 4.7 to perform the modulation of γ_1, γ_2, γ_3 individually in (110) p-MOSFETs and in Fig. 4.8, 4.9, 4.10 to perform the modulation of γ_1, γ_2, γ_3 individually in (001) p-MOSFETs. It is obviously seen that the γ_1 and γ_3 modulations have the stronger and mutually reversely symmetric influences on the subband levels, but the γ_2 modulation has just slight effects on the subband levels. Furthermore, though the different sets of Luttinger parameters in Table 4.1, the corresponding total density-of-states functions are calculated with a F_s=1 MV/cm triangular potential as shown in Fig. 4.11 for (001) case and Fig. 4.12 for (110) case. Similar results can be found between the sets of Luttinger parameters from Lawaetz [2] and Hesel [3] but with the different results from Balslev and Lawaetz [3] (due to around -20% deviation in γ_2) as listed in Table 4.1. Based on the results in Fig. 4.4, 4.11, and 4.12, it is followed that using the Luttinger parameters from Lawaetz [2] and Hesel [3] can obtain more satisfactory comparisons with the experimental data [4]. Thus, the calculated <110>/(110) hole mobility including the phonon and the surface roughness scattering with the Luttinger parameters from Hesel [3] are drawn together with the experimental <110>/(110) hole effective mobility at 50, 200, and 300 K [8] in Fig. 4.13. On the other hand, the calculated <110>/(110) and <001>/(110) hole mobility at 2 K are shown in Fig. 4.14 for compared with the experimental hole effective mobility at 2 K from [8]. In Fig. 4.15, the resulting DOS effective masses also compare to the measured cyclotron effective masses in [4].

In summary, with the γ sets of Lawaetz [2] and Hesel [3] in Table 4.1, the validity of the bulk oriented Luttinger parameters in 2DHG has been successfully justified by using the Takahashi, et al.'s Shubnikov-de Haas (SdH) oscillation experiment at 2 K [4]. These two sets of bulk oriented Luttinger parameters can therefore directly apply to the subband structure calculation and the hole mobility calculation, both with the acceptable precision.

4.3 Conclusions

Three published sets of bulk oriented Luttinger parameters have been successfully examined by finding out the possible agreements with the direct experiments by Takahashi, et al. The *realistic* subband structures have been constructed by the these comparisons. The resulting hole mobility and DOS effective masses have clearly been demonstrated in (110) p-MOSFETs at 2 K.

References

[1] R. Winkler and A. I. Nesvizhskii, "Anisotropic hole subband states and interband optical absorption in [mmn]-oriented quantum wells," *Phys. Rev. B,* vol. 53, no. 15, pp. 9984-9992, Apr. 1996.

[2] P. Lawaetz, "Valence-band parameters in cubic semiconductors," *Phys. Rev. B,* vol. 4, no. 10, pp. 3460-3467, Nov. 1971.

[3] R. G. Humphreys, "Valence band averages in silicon: Anisotropy and non-parabolicity," *J. Phys. C: Solid State Phys.*, vol. 14, pp. 2935-2942, Feb. 1981.

[4] T. Takahashi, G. Yamahata, J. Ogi, T. Kodera, S. Oda, and K. Uchida, "Direct observation of subband structures in (110) pMOSFETs under high magnetic field: impact of energy split between bands and effective masses on hole mobility," in *IEDM Tech. Dig.*, 2009, pp. 477-480

[5] Schred, http://nanohub.org/resources/schred.

[6] S. Takagi, A. Toriumi, M. Iwase, and H. Tango, "On the universality of inversion layer mobility in Si MOSFET's: Part I-effects of substrate impurity concentration," *IEEE Trans. Electron Devices*, vol. 41, no. 12, pp. 2357-2362, Dec. 1994.

[7] G. Dresselhaus, A. F. Kip, and C. Kittel, "Cyclotron resonance of electrons and holes in silicon and germanium crystals," *Phys. Rev.*, vol. 98, no. 2, pp. 368-384, Apr. 1955.

[8] T. Takahashi, T. Kodera, S. Oda, and K. Uchida, "Experimental study on subband structures and hole transport in (110) Si p-type metal-oxide-semiconductor field-effect transistors under high magnetic field," *J. Appl. Phys.*, vol. 109, pp. 034505-1-034505-7, Feb. 2011.

Luttinger Parameters	γ_1	γ_2	γ_3
Lawaetz [2]	**4.22**	**0.39**	**1.44**
Hensel [3]	**4.285**	**0.339**	**1.446**
Balslev and Lawaetz [3]	**4.23**	**0.31**	**1.46**

Table 4.1 The list of the widely used bulk oriented Luttinger parameters mentioned in the Lawaetz's and Humphreys's published literatures [2], [3].

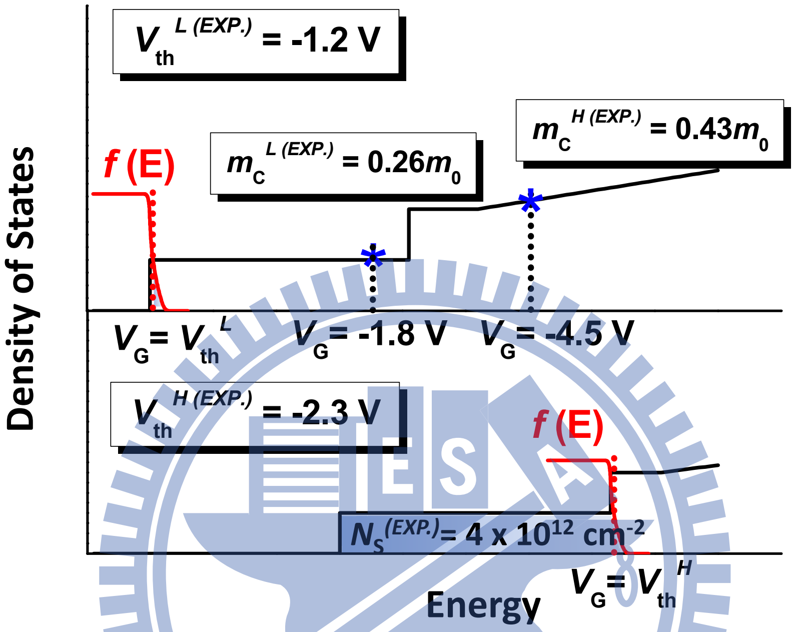

Fig. 4.1 Illustration of the experimental criteria [4] in the presence of density-of-states functions under two bias conditions, V_{th}^L and V_{th}^H with 3×10^{16} cm^{-3} substrate doping (N_{sub}) at 2 K. The abrupt Fermi distribution can ensure the proper switching.

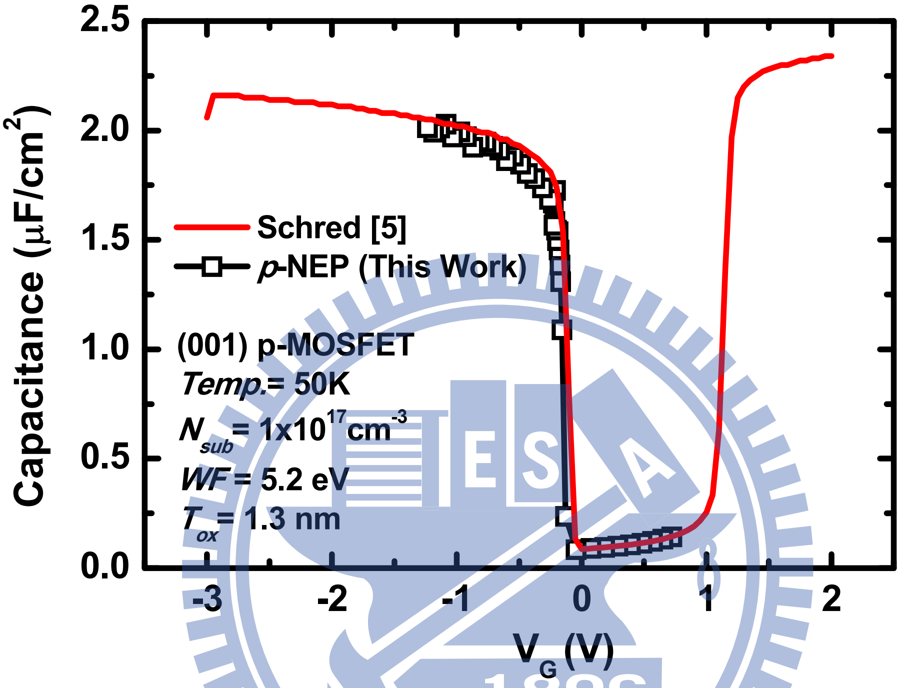

Fig. 4.2 Low-temperature validity of *p*-NEP preliminarily confirmed by the simulated capacitance at 50 K by Schred [5] which adopts the constant mass self-consistent Schrödinger-Poisson method. Although the different methods of band structure calculations are made between Schred and our work, both self-consistent results still can offer a preliminary comparison.

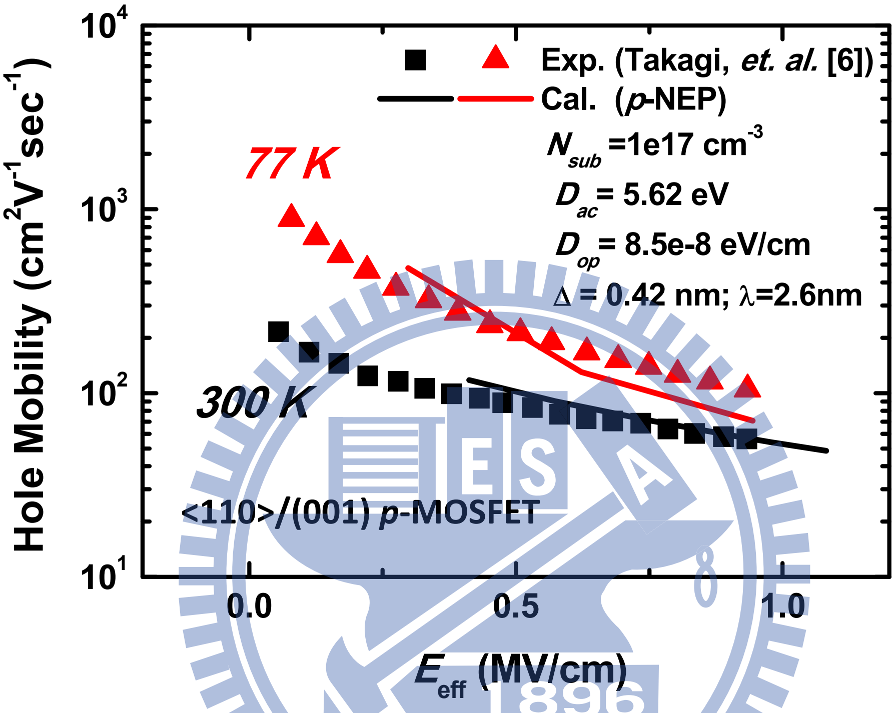

Fig. 4.3 Low temperature validity of *p*-NEP preliminarily confirmed by the experimental hole effective mobility [6] at 77 K and 300 K.

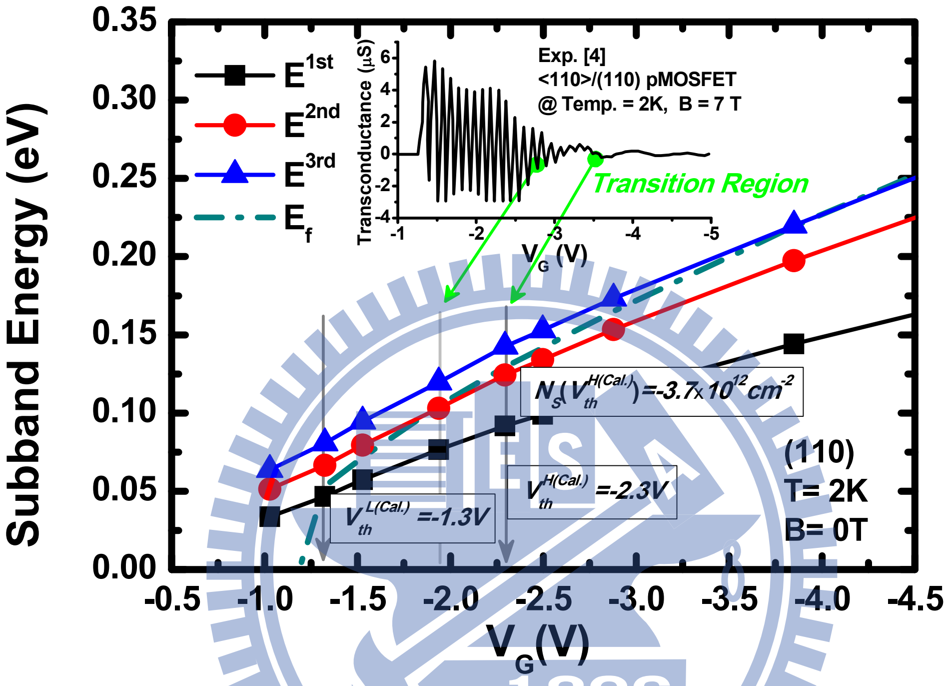

Fig. 4.4 The situation *with* γ_1^0, γ_2^0, *and* γ_3^0 represented by the subband energies and Fermi level versus gate volatge with 3×10^{16} cm^{-3} substrate doping (N_{sub}) and 6 nm oxide thickness of SiO$_2$ at 2 K. The simulation results are: $V_{\mathrm{th}}^{L\,(Cal.)}$= -1.3 V, $V_{\mathrm{th}}^{H\,(Cal.)}$ = -2.3 V and $N_s^{(Cal.)}(V_{\mathrm{th}}^{H})$ = 3.7×10^{12} cm^{-2}. The ccalculated $V_{\mathrm{th}}^{H\,(Cal.)}$ and $N_s^{(Cal.)}(V_{\mathrm{th}}^{H})$ are closed to the experimental values [4].

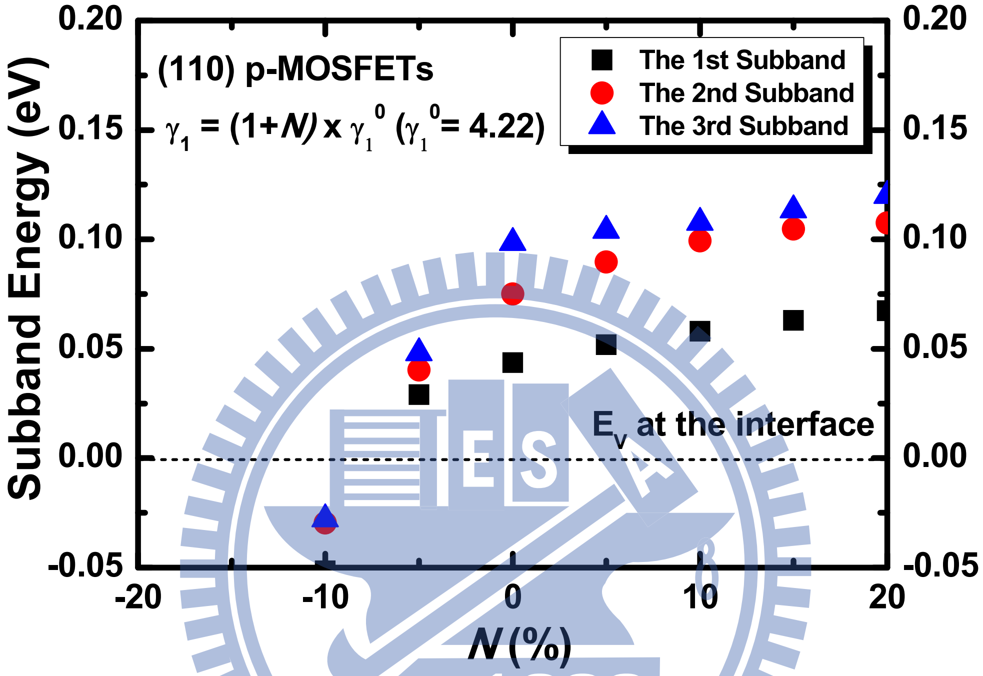

Fig. 4.5 The impact of γ_1 modulation on subband minimum of (110) p-MOSFETs. The triangular potential approximation is used to efficiently quantify this impact with 3×10^{16} cm^{-3} substrate doping (N_{sub}) and fixed 0.25 MV/cm surface field (F_s).

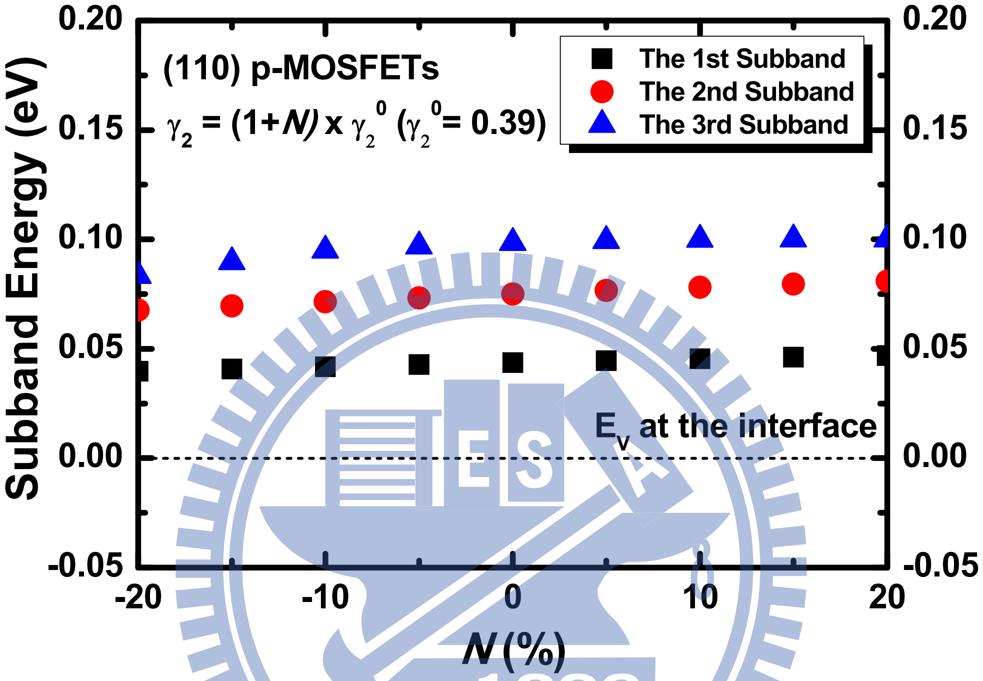

Fig. 4.6 The impact of γ_2 modulation on subband minimum of (110) p-MOSFETs. The triangular potential approximation is used to efficiently quantify this impact with 3×10^{16} cm^{-3} substrate doping (N_{sub}) and fixed 0.25 MV/cm surface field (F_s).

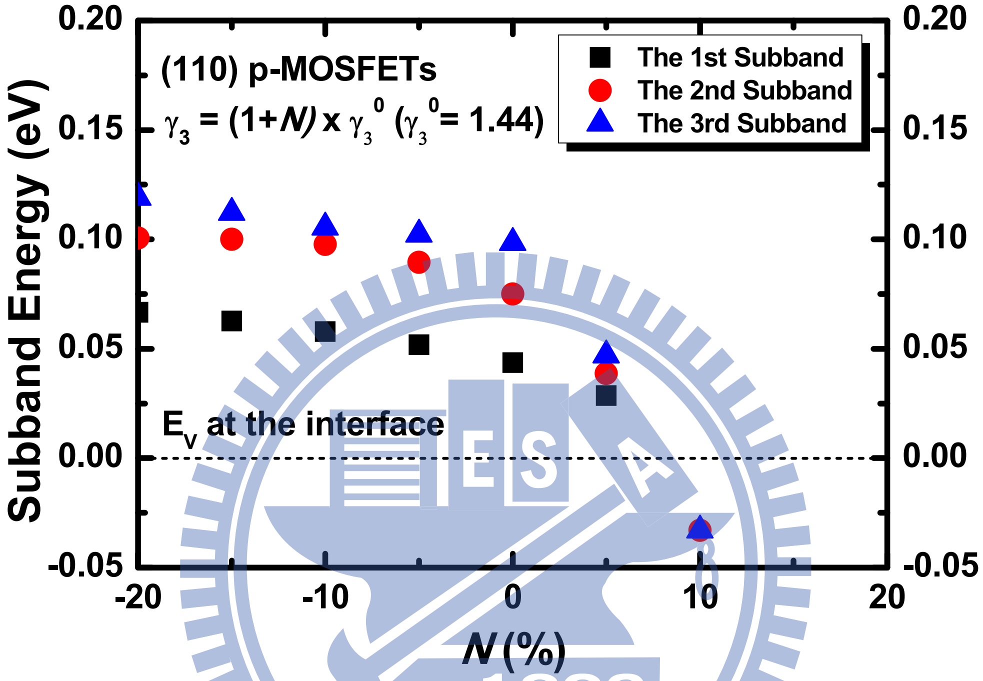

Fig. 4.7 The impact of γ_3 modulation on subband minimum of (110) p-MOSFETs. The triangular potential approximation is used to efficiently quantify this impact with 3×10^{16} cm^{-3} substrate doping (N_{sub}) and fixed 0.25 MV/cm surface field (F_s).

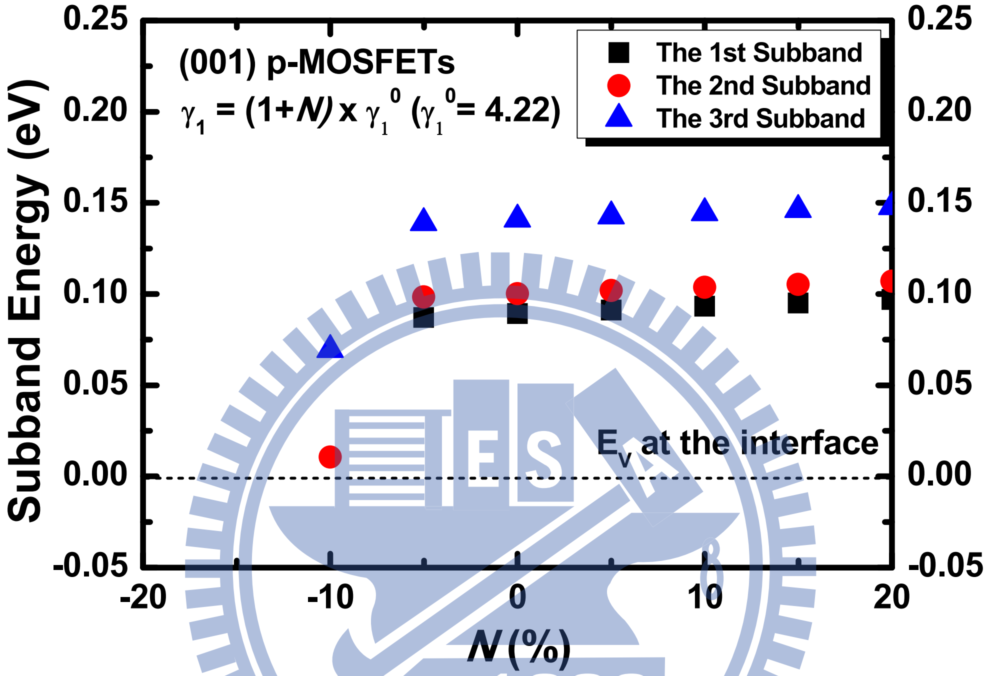

Fig. 4.8 The impact of γ_1 modulation on subband minimum of (001) p-MOSFETs. The triangular potential approximation is used to efficiently quantify this impact with 3×10^{16} cm^{-3} substrate doping (N_{sub}) and fixed 0.25 MV/cm surface field (F_s).

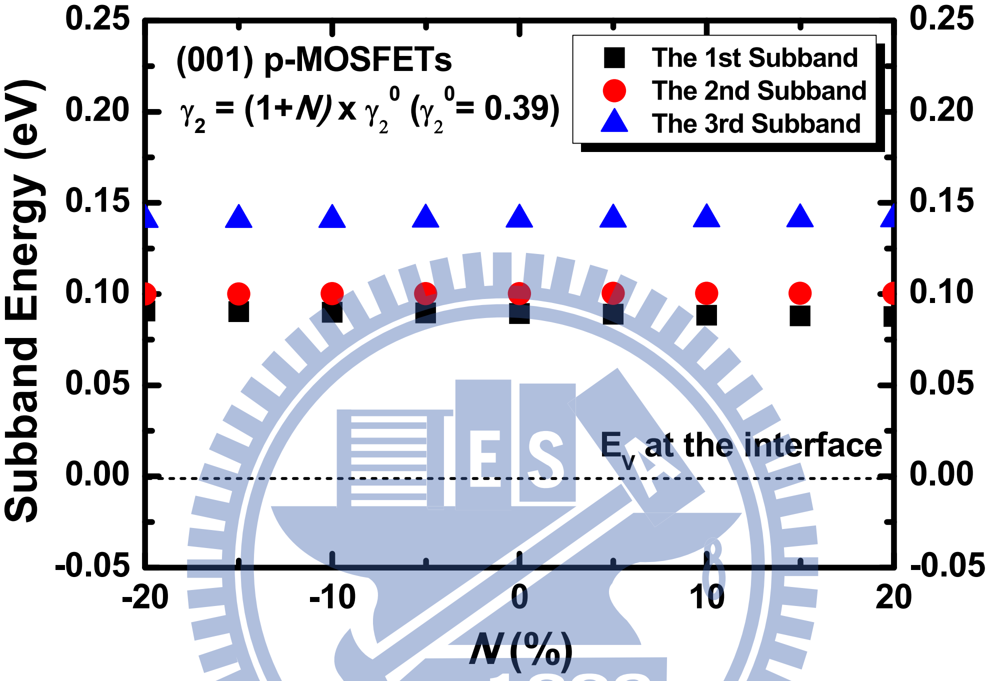

Fig. 4.9 The impact of γ_2 modulation on subband minimum of (001) p-MOSFETs. The triangular potential approximation is used to efficiently quantify this impact with 3×10^{16} cm^{-3} substrate doping (N_{sub}) and fixed 0.25 MV/cm surface field (F_s).

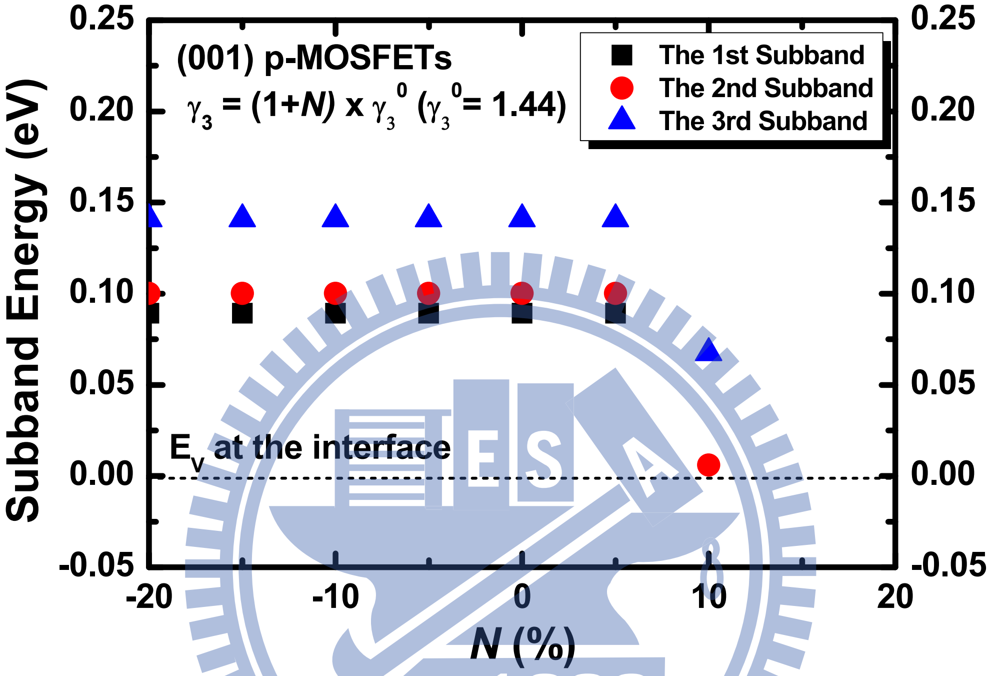

Fig. 4.10 The impact of γ_3 modulation on subband minimum of (001) p-MOSFETs. The triangular potential approximation is used to efficiently quantify this impact with 3×10^{16} cm^{-3} substrate doping (N_{sub}) and fixed 0.25 MV/cm surface field (F_s).

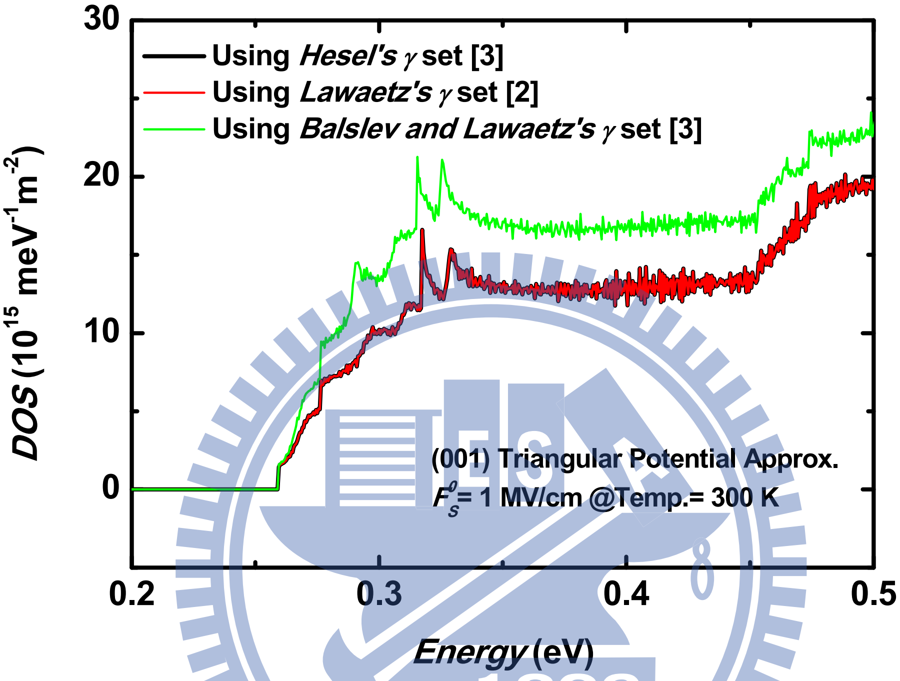

Fig. 4.11 The calculated (001) total density-of-states functions using the three different sets in Table 4.1 for a triangular potential with F_s=1 MV/cm at 300 K.

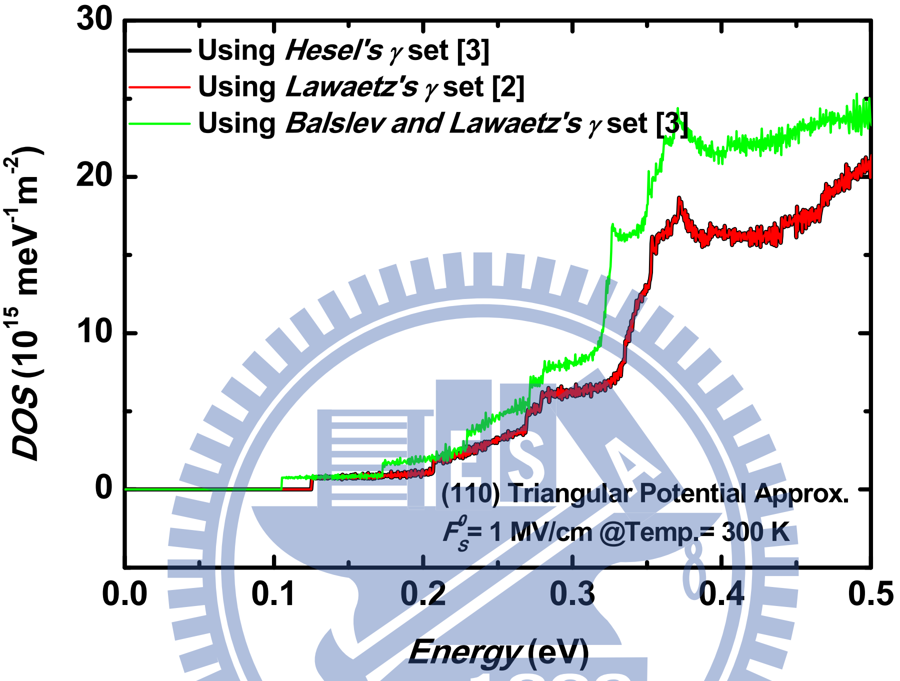

Fig. 4.12 The calculated (110) total density-of-state functions using the three different sets in Table 4.1 for a triangular potential with F_s=1 MV/cm at 300 K.

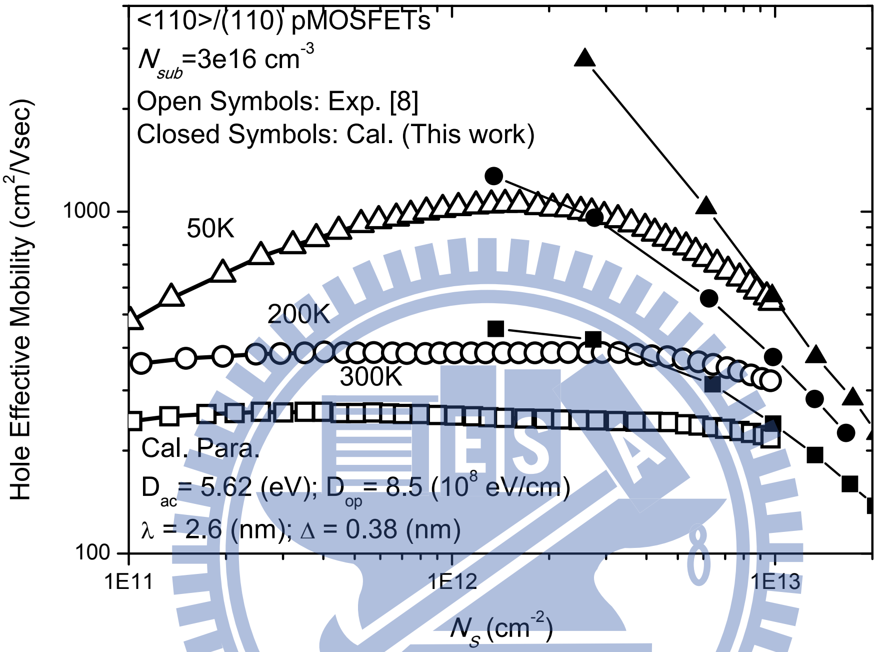

Fig. 4.13 Comparison of calculated <110>/(110) hole mobility due to phonon and surface roughness scattering with the Luttinger parameters from Hensel [3] with the experimental <110>/(110) hole effective mobility [8] at 50, 200, and 300 K.

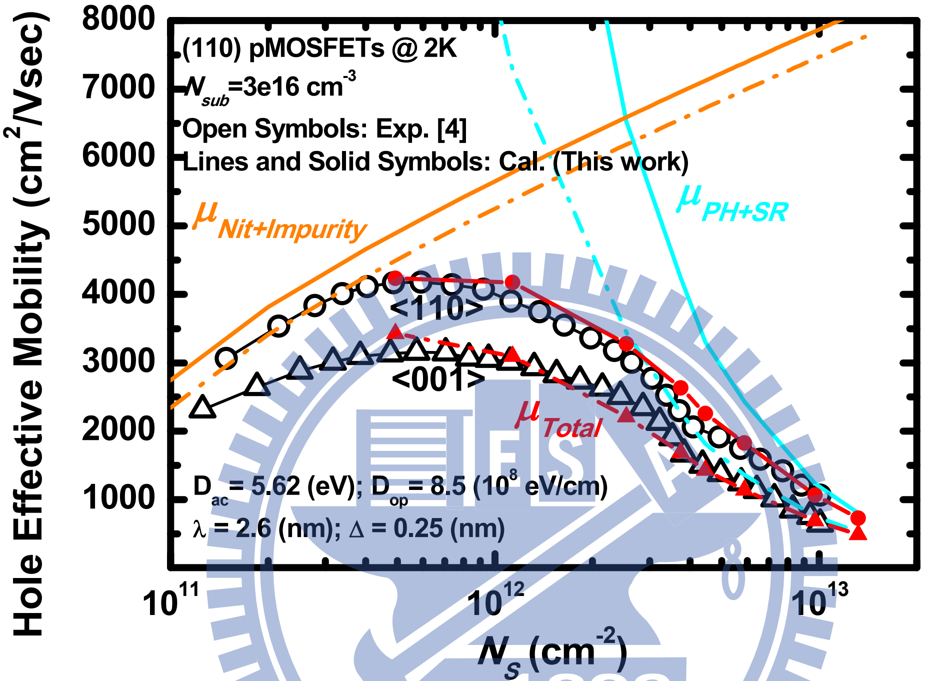

Fig. 4.14 Comparison of calculated <110> and <001>/(110) hole mobility due to phonon and surface roughness scattering with the Luttinger parameters from Hesel [3] with the experimental hole effective mobility data [8] at 2K. Interface-trap- and ionized-impurity-limited hole mobility (empirical fitting) are involved in calculation using Matthiessen's rule. Note that the rms height of the amplitude of the surface roughness Δ is extracted to be 0.25 nm here which differs from the value in Fig. 4.13.

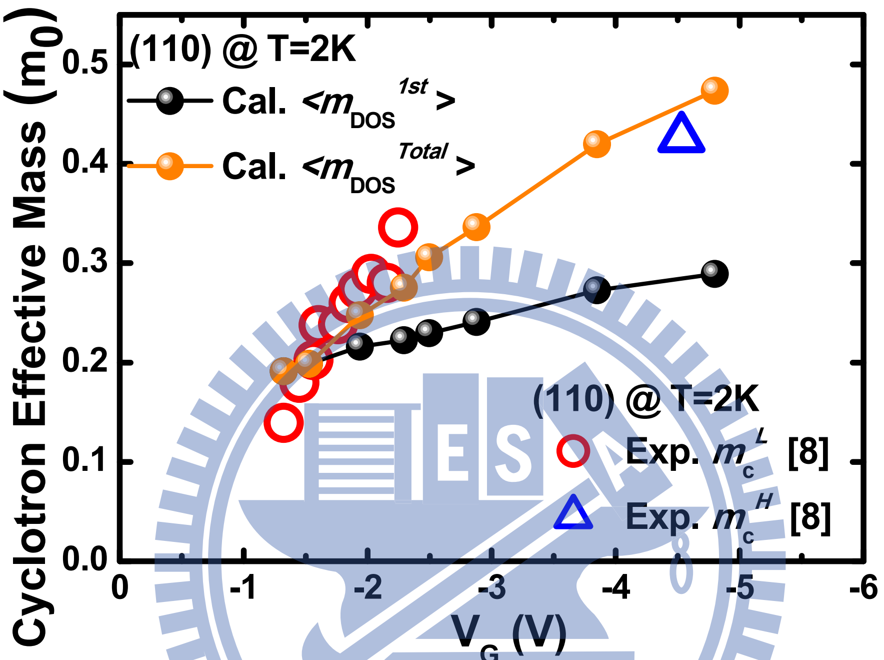

Fig. 4.15 Calculated density-of-states effective masses using the γ set from Hesel [3] with 3×10^{16} cm^{-3} substrate doping (N_{sub}) at 2 K and 0 T. The direct comparison with the measured cyclotron effective masses is shown.

Chapter 5

Three-Dimensional GPa-Level Stress Altered Hole Mobility in (001) and (110) Silicon Inversion Layers

5.1 Introduction

For highly scaled MOSFET devices [1], very complicated mechanical stresses, no matter the intentional or unintentional stressors from arbitrary directions, will be inevitable. The reason is that applied mechanical stresses can boost device performance [2], [3]. Especially for the three-dimensional structure of multi-gate transistor such as the commercialized FinFET, the strains generated from the fin-width and fin-height are directly measured with the absolute values of 0.1% to 0.8% [4], [5]. This range of mixed strains will cause the substantial warping of band structures in the quantum-confined inversion layer and lead to the carrier mobility change. So far, many groups presented different calculated results under the uniaxial and biaxial stresses in (001) and/or (110) p-MOSFETs [6]-[9], concerning the surface orientations of p-FinFET sidewalls. However, the individual contributions of hole mobility change from phonon scattering, surface-roughness scattering, conductivity effective mass, and scattering time are still not fully clear, especially for the 3-D stressed conditions. Importantly, in the area of strain altered hole inversion-layer mobility study to date, the primary factors and guidelines needed to experimentally determine the unique values of Bir-Pikus deformation potentials, a_υ, b, and d were not published, in particular in the GPa-level stress range. In order to clarify these issues, the research will be discussed as in the following sections.

In Section 5.2, we will focus on the individual contributions of hole mobility change from three scattering mechanisms: acoustic phonon scattering, optical phonon scattering, and the surface roughness scattering. Relying on these scattering mechanisms, the well-known Matthiessen's rule in the 3-D stressed (001) and (110) p-MOSFETs also can be verified. The study on the scattering-time-limited and the conductivity-mass-limited mobility changes will be clarified in Section 5.3. Section 5.4 will be devoted to the calculated hole inversion-layer mobility change for varying a_υ, b, and d. This leads to the establishment of the guidelines which enable, in a step-by-step manner, an experimental determination of the unique values of the factors. The parameters used in Section 5.2 and 5.3 are listed in Table 5.1 Notice that the scattering parameters used in Section 5.2 and 5.3 are assumed to be independent of the Bir-Pikus potentials a_v, b, and d. On the contrary, the modified scattering parameters and Bir-Pikus deformation potentials used in Section 5.4 are listed in Table 5.2.

5.2 Phonon and Surface-Roughness Limited Hole Mobility Changes

Firstly, we show the calculated (001) and (110) total mobility changes at the effective field $E_{\mathrm{eff}} \approx 1.1$ MV/cm and 1.2 MV/cm, respectively, and make a comparison with the simulated data from [8], [9] in Fig. 5.1 and 5.2. The device structures for (001) and (110) p-MOSFETs are drawn in Fig. 5.3 in the presence of the longitudinal, transverse, and out-of-plane stresses. In order to determine the individual contributions of the phonon and surface roughness scattering, we calculate the hole mobility individually by replacing τ_{total}^{μ} with τ_{phonon}^{μ} and τ_{sr}^{μ}. Therefore, the total, phonon-limited, and surface-roughness-limited mobility changes can be calculated separately as illustrated in Fig. 5.4, 5.5, and 5.6 for (001) and 5.7, 5.8, and 5.9 for (110) with the longitudinal, transverse, and out-of-plane stress, respectively. At first, as depicted in Fig. 5.4 and 5.7, surface roughness scattering obviously limits the (001) and (110) mobility enhancement in the region of high longitudinal compressive stress. Secondly, all highlighted cases here indicate that surface-roughness-limited mobility is not as sensitive as phonon-limited mobility. The reason can be related to the momentum change q in denominator of Eq. (2.3.4.1) which offsets the change of density-of-states in the numerator.

Next, we will discuss the validity of Matthiessen's rule for the universal mobility on the 3-D stressed (001) and (110) p-MOSFETs. The error percentage of the mobility is chosen to quantify the validity of Matthiessen's rule and the equation can be described as

$$\mu\ Error = \left(\left(\frac{1}{\mu_{phonon}} + \frac{1}{\mu_{sr}}\right) - \mu_{Total}\right) / \mu_{Total}, \tag{5.2.1}$$

where μ_{phonon}, μ_{sr} and μ_{Total} are the average mobility over all k-states. As shown in Fig. 5.10 and 5.11, the errors are about 20 ~ 50% both for (001) and (110) cases and the value of error can be seen as a function of stress. The large errors due to Matthiessen's rule are stronger energy-dependent functions of the group velocity, scattering time, and density-of-states in the hole inversion layers.

5.3 Scattering Time and Conductivity Mass Limited Hole Mobility Changes

According to the effective mass approximation in Section 3.2.2, it is a quasi-classical treatment which can straightforwardly represent the shape and the warping of the band structures. As to the conductivity effective mass, it directly relates to the group velocity along the transport direction and acts an important role in carrier mobility. However, due to the nature of the non-parabolic and anisotropic valence bandstructures, the constant conductivity effective mass is no longer appropriate to the inversion-layer hole subband structures. Thus, the reversely extracted conductivity effective mass is incorporated here via

$$\overline{m_C} = e \times \bar{\tau}/\mu, \qquad (5.3.1)$$

where e is the free electron charge, $\bar{\tau}$ refers to the average scattering time, and μ refers to the average mobility. Eq. (5.3.1) can macroscopically cover the warping of valence band structure and reflect the transport properties as well. $\bar{\tau}_{total}$ is the average scattering time derived elaborately by

$$\overline{\tau_{Total}} = \frac{\sum_{\mu} \frac{1}{(2\pi)^2} \int_{\mu} {}_{BZ} d^2k \times \tau^{\mu}{}_{Total}(k) \times f_0(k)}{\sum_{\mu} \frac{1}{(2\pi)^2} \int_{\mu} {}_{BZ} d^2k \times f_0(k)}. \qquad (5.3.2)$$

The results of average scattering time and the extracted conductivity effective masses are shown in Fig. 5.12 and 5.13 for (001) and (110) cases, respectively. The conductivity effective masses extracted here are not as similar as the directly calculated (double differential effective mass) conductivity effective masses near the Γ point of each band structure. The purpose of this inverse extraction process is to offer the straightforward physical value rather than calculating the hole mobility elaborately.

The scattering-time-limited and the conductivity-mass-limited mobility changes are illustrated in Fig. 5.14 to 5.16 for (001) and 5.17 to 5.19 for (110) with the longitudinal, transverse, and out-of-plane stress all taken into account. According to Eq. (5.3.1), the relationship between the scattering time and the conductivity mass is represented by:

$$\frac{\mu(\sigma)}{\mu(0)} = \frac{\overline{\tau_{Total}}(\sigma)}{\overline{\tau_{Total}}(0)} \times \frac{\overline{m_c}(0)}{\overline{m_c}(\sigma)}. \tag{5.3.3}$$

Through the (001) cases in Fig. 5.14 and 5.15, the non-equivalence between the longitudinal compressive condition and transverse tensile condition can be attributed to the opposite normal strains as shown in Fig. 2.3: the biaxial tensile strains reduce the influences of the shear strains both on the scattering time and the conductivity effective mass. Here, we can anticipate the more sensitive warping of 2-D k-space energy contours of the dominant subbands on (001) than (110) as shown in Fig. 5.20 because the stress-induced variance of the (001) conductivity effective masses and scattering time are larger than (110) ones. Therefore, the (110) scattering-time-limited and the conductivity-effective-mass-limited mobility changes are smaller than the (001) cases. We also calculate the average 2-D density-of-states effective masses as

$$\overline{m_{DOS}} = 2\pi\hbar^2 \times \frac{\int_{E_1^{(0)}} DOS_{Total}(E) \times f_0 dE}{\int_{E_1^{(0)}} f_0 dE} \times \frac{1}{m_0}, \tag{5.3.4}$$

to see the relationship between 2-D density-of-states effective mass and scattering time under the 3-D stressed conditions. The stress-induced $1/\overline{m}_{DOS}$ changes are drawn in Fig. 5.14 to 5.19 with the dashed lines, showing the comparisons with the scattering-time-limited mobility changes, especially when the surface roughness influence is absent. This is because τ_{sr} depends not only on $1/\overline{m}_{DOS}$ term but also the momentum-change-dependent term as discussed in Section 2.3.4. The following expression will make sense in the absent of the surface roughness,

$$\frac{\mu(\sigma)}{\mu(0)} = \frac{\bar{m}_c(0)}{\bar{m}_c(\sigma)} \times \frac{\bar{m}_{DOS}(0)}{\bar{m}_{DOS}(\sigma)}. \tag{5.3.5}$$

5.4 Effect of Strained k・p Deformation Potentials on Hole Mobility

The valence-band structure in the inversion layers of silicon p-MOSFETs can be obtained by self-consistently solving Poisson and Schrödinger's equations by *p*-NEP. Then, it is a straightforward task to deal with two-dimensional hole transport issues. This also is the case for state-of-the-art p-MOSFETs undergoing the strain engineering in the manufacturing process. Specifically, to compensate for the mobility degradation in a scaling direction, GPa-level stresses [10], [11] are needed. To match this trend, it is crucial to accurately calculate the hole inversion-layer mobility in the strain altered valence-band structure, especially the widely used strained k・p valence-band structure originating from the works of Luttinger and Kohn [12] and of Bir and Pikus [13]. So far, however, published calculation results in the context of the strained k・p valence-band structure differed much from each other [6]-[9], as shown in Fig. 5.21

Such inconsistencies are likely due to largely spanned values [6], [9] (see Table 5.3) in the Bir-Pikus deformation potentials, a_υ, b, and d. Indeed, according to literature sources (see [14]-[17] and the references therein), a_υ, b, and d were widespread in terms of the error range: 2.06 eV ≤ a_υ≤ 2.46 eV, −2.58 eV ≤ b ≤ −1.5 eV, and −5.3 eV ≤ d ≤ −3.1 eV. There were two origins proposed [15] for such large errors: one of a complicated dependence on the strain conditions making the extraction of deformation potentials a hard problem and one of a limited strain range used in the extraction. For example, b = −2.33 eV and d = −4.75 eV [15] were representative of small-strain situations and deviations should be expected at large strain, according to Fischetti, et al. [15]. Although good agreement with the mobility enhancement data was obtained with another set of a_υ, b, and d (see Table I for Wang, et al.'s work [6]), the corresponding applied uniaxial stress range is not wide enough (less than 400 MPa in magnitude; see Fig. 18 of [6]).

Importantly, in the area of strain altered hole inversion-layer mobility study to date, the primary factors and guidelines needed to experimentally determine the unique values of a_υ, b, and d were not published, in particular in the GPa-level stress range. To perform such experimental extraction as rigorously as possible, two additional factors should be taken into account. One is the acoustic deformation potential, D_{ac}. D_{ac} is not an independent parameter but a function of a_υ, b, and d, according to Bir and Pikus [13], Tiersten [18], and Lawaetz [19]. The second additional factor is the deformation potential of optical phonons d_0 or the average optical deformation potential D_{op}, which will affect the choice of surface roughness parameters while making a fit to mobility data.

5.4.1 Effect of Bir-Pikus Deformation Potentials

Calculations with different values of Bir-Pikus parameters were executed for each of three distinct uniaxial stress directions: (i) in-plane longitudinal stress along the transport <110> direction; (ii) in-plane transverse stress perpendicular to the transport <110> direction; and (iii) out-of-plane stress in the quantum confinement direction. The results on both (001) and (110) substrates are shown in Fig. 5.21 for two cases: one of a_υ = 2.46 eV, b = −2.1 eV, and d = −4.8 eV (close to that of [9]) and one of $a_\upsilon = 2.1$ eV, $b = -1.6$ eV, and $d = -2.7$ eV (as in [6]). The calculated 3-D uniaxial stress dependencies of mobility change resemble those published elsewhere [8], [9]. This confirms the validity of the calculation method in this work. In Fig. 5.22, one can see that different Bir-Pikus parameters lead to different strain altered hole mobilities, particularly for the longitudinal compressive stress.

To determine the primary factors, we made a set of $a_\upsilon = 2.46$ eV, $b = -2.1$ eV, and $d = -4.8$ eV as reference. In the subsequent calculation, one of these parameters is given three distinct values (one reference and two values equal or close to the upper and lower limits of the aforementioned error range), along with the two remainders fixed at their reference values. The results are plotted in Fig. 5.23 for two <110> uniaxial stresses of –2 and –3 GPa on (001) substrate. Note that different sets of a_υ, b, and d produce different calculated D_{ac} values according to (1), which will *together* alter the amount of the mobility change percentage. It can further be seen from Fig. 5.23 that a change in a_υ only has a weak effect on mobility enhancement; the effect of varying b is moderate; but for d, its effect is strongly large. The origin is due to the decreased subband separation and the increased DOS, as shown in the inset of the figure. The primary factor, d, and the secondary factor, b, also hold for (110) case.

5.4.2 Guidelines and Experimental Determination

Guidelines are established in terms of a flowchart shown in Fig. 5.24. There are six input parameters: a_υ, b, d, d_0, Δ, and λ. The corresponding D_{ac} and D_{op} can be determined according to Eq. (2.3.2.1) and (2.3.3.1), respectively. To facilitate the procedure, we first took a literature value of 26.6 eV for d_0 [20] and hence the corresponding D_{op} of 8.5×10^{-8} eV/cm. Then, a fit to the experimental unstrained hole effective mobility data in Fig. 5.25 as cited elsewhere [21] was carried out, producing Δ = 0.42 nm and λ = 2.6 nm. It can be seen from the figure that a good fitting appears in the high E_{eff} region or the universal mobility region, valid for different substrate orientations and different transport directions. This validates the presented calculation method. Here, E_{eff} is the vertical effective electric field in the inversion layer, which was calculated using the empirical formula: $E_{eff} = e(\eta P_{inv} + P_{dep})$ with η taken as 1/3 according to Takagi, et al. [22], where P_{inv} is the inversion-layer density and P_{dep} is the substrate depletion charge density. Deviations in the low E_{eff} region are expected because impurity Coulomb scattering was not taken into account in this work.

At this point, the number of input parameters reduces to three. Since a_υ and b are weak or moderate in effect, we can quote the literature values: $a_\upsilon = 2.46$ eV [15] and $b = -2.1$ eV [16]. Then, with a guess of d, the strain induced hole mobility change was calculated, an updated d was obtained in comparison with the experimental data. This process was iterated until a good fitting is achieved. In this way, we obtained $d = -3.1$ eV and $D_{ac} = 5.62$ eV from a fit to hole inversion-layer mobility enhancement data under uniaxial compressive stress [10], [11], as depicted in Fig. 5.26. Biaxial-stress mobility data [23], [24] also were quoted. Extra calculation for this case was performed. The result is shown in the inset of the figure. Fairly good agreement remains, without changing any parameters. The extracted results are listed in Table 5.2. The corresponding calculated hole mobility change at two different E_{eff} is shown in Fig. 5.21 for comparison.

Even making a change of b to −1.6 eV, we found that the reproduction quality is acceptable, as shown in the inset of Fig. 5.26. Strikingly, such change in b does not significantly affect the calculated hole mobility enhancement in case of uniaxial stress, as shown in Fig. 5.26. This invariability supports the published error range of −2.58

eV $\leq b \leq -1.5$eV [14]-[17]. Above arguments hold for other a_υ values, as has been proved in Fig. 5.23. This can reasonably explain the commonly used values of 2.06 eV $\leq a_\upsilon \leq$ 2.46 eV [14], [17]. Good reproduction of the data is evident and can be found when a_υ = 2.46 eV, b = −2.1 eV, and d = −3.1 eV. It is noteworthy that the experimentally determined d of −3.1 eV in this work is exactly that (−3.1 eV) [16] based on cyclotron resonance measurements [25].

Above results stemmed from a specific d_0 of 26.6 eV. As illustrated by the guidelines in Fig. 5.24, a change in d_0 may change the extracted surface roughness parameters. In fact, the quoted mobility data sources [10], [11], [21], [23], [24] came from different manufacturing processes featuring different surface roughness details. Thus, it is clear that the uncertainty exists in d_0 or equivalently the surface roughness parameters. To reflect this, we show in Fig. 5.27 the effect of varying surface roughness height Δ. Evidently, the calculated hole mobility change in Fig. 5.27 is almost the same as Fig. 5.26. In other words, the uncertainty in Δ does not significantly affect the calculated hole mobility change. This also is the case for surface roughness correlation length λ. Therefore, the extracted parameters as listed in Table 5.2 remain valid in the presence of the uncertainty in the surface roughness parameters.

Finally, we add two interesting calculation results, as depicted in Fig. 5.28. First, the inclusion of the screening effect in surface roughness scattering will reduce the calculated hole inversion-layer mobility change, particularly in the high stress region. Second, a change in the surface roughness model from the exponential function to the Gaussian function does not influence the result.

5.5 Conclusions

It has been found the phonon-limited mobility change is more stress-sensitive than the surface-roughness-limited one, and the mobility change ratio can be reversely proportional to the conductivity effective mass and density-of-states effective mass only in the absence of the surface roughness-limited mobility change. Individual contributions of hole mobility change have all be quantified. Calculated hole mobility change due to varying a_{υ}, b, and d has been created and has accounted for 3-D uniaxial stress conditions. The primary factor d and the secondary factor b have been drawn. Guidelines have been established, followed by the experimental determination of a_{υ}, b, and d. The literature errors of the Bir-Pikus deformation potentials have therefore been improved.

References

[1] ITRS 2011. Available: http://www.itrs.net.

[2] T. Ghani, M. Armstrong, C. Auth, M. Bost, P. Charvat, G. Glass, T. Hoffmann, K. Johnson, C. Kenyon, J. Klaus, B. Mclntyre, K. Mistry, A. Murthy, J. Sandford, M. Silberstein, S. Sivakumar, P. Smith, K. Zawadzki, S. Thompson and M. Bohr, "A 90nm high volume manufacturing logic technology featuring novel 45nm gate length strained silicon CMOS transistors," in *IEDM Tech. Dig.*, 2003, pp. 978-980.

[3] P. Packan, S. Akbar, M. Armstrong, D. Bergstrom, M.Brazier, H. Deshpande, K. Dev, G. Ding, T. Ghani, O. Golonzka, W. Han, J. He, R. Heussner, R. James, J. Jopling, C. Kenyon, S. H. Lee, M. Liu, S. Lodha, B. Mattis, A. Murthy, L. Neiberg, J. Neirynck, S. Pae, C. Parker, L. Pipes, J. Sebastian, J. Seiple, B. Sell, A. Sharma, S. Sivakumar, B. Song, A. St. Amour, K. Tone, T. Troeger, C. Weber, K. Zhang, Y. Luo, and S. Natarajan, "High performance 32nm logic technology featuring 2nd generation high-k + metal gate transistors," in *IEDM Tech. Dig.*, 2009, pp. 659-662.

[4] N. Serra, F. Conzatti1, D. Esseni, M. De Michielis, P. Palestri, L. Selmi, S. Thomas, T.E. Whall, E.H.C. Parker, D.R. Leadley, L. Witters, A. Hikavyy, M.J. Hÿtch, F. Houdellier, E. Snoeck, T.J. Wang, W.C. Lee, G. Vellianitis, M.J.H. van Dal, B. Duriez, G. Doornbos and R.J.P. Lander, "Experimental and physics-based modeling assessment of strain induced mobility enhancement in FinFETs," in *IEDM Tech. Dig.*, Dec. 2009, pp. 71-74.

[5] M. Saitoh, A. Kaneko, K. Okano, T. Kinoshita, S. Inaba, Y. Toyoshima and K. Uchida, "Three-dimensional stress engineering in FinFETs for mobility/on-current enhancement and gate current reduction ," in *VLSI Symp.*

Tech. Dig., 2008, pp. 18–19.

[6] E. X. Wang, P. Matagne, L. Shifren, B. Obradovic, R. Kotlyar, S. Cea, M. Stettler, and M. D. Giles, "Physics of hole transport in strained silicon MOSFET inversion layers," *IEEE Trans. Electron Devices*, vol. 53, no. 8, pp. 1840-1851, Aug. 2006.

[7] A. T. Pham, C. Jungemann, and B. Meinerzhagen, "Microscopic modeling of hole inversion layer mobility in unstrained and uniaxially stressed Si on arbitrarily oriented substrates," *Solid-State Electronics*, vol. 52, pp. 1437-1442, May 2008.

[8] P. Packan, S. Cea, H. Deshpande, T. Ghani, M. Giles, O. Golonzka, M. Hattendorf, R. Kotlyar, K. Kuhn, A. Murthy, P. Ranade, L. Shifren, C. Weber, and K. Zawadzki, "High performance Hi-K+ metal gate strain enhanced transistors on (110) silicon," in *IEDM Tech. Dig.*, 2008, pp. 1-4.

[9] F. M. Bufler, A. Erlebach, and M. Oulmane, "Hole mobility model with silicon inversion layer symmetry and stress-dependent piezoconductance coefficients," *IEEE Electron Device Lett.*, vol. 30, no. 9, pp. 996-998, Sep. 2009.

[10] L. Smith, V. Moroz, G. Eneman, P. Verheyen, F. Nouri, L. Washington, M. Jurczak, O. Penzin, D. Pramanik, and K. De Meyer, "Exploring the limits of stress-enhanced hole mobility," *IEEE Electron Device Lett.*, vol. 26, no. 9, pp. 652-654, Sep. 2005.

[11] L. Washington, F. Nouri, S. Thirupapuliyur, G. Eneman, P. Verheyen, V. Moroz, L. Smith, X. Xu, M. Kawaguchi, T. Huang, K. Ahmed, M. Balseanu, L. Q. Xia, M. Shen, Y. Kim, R. Rooyackers, K. De Meyer, and R. Schreutelkamp, "pMOSFET with 200% mobility enhancement induced by multiple stressors," *IEEE Electron Device Lett.*, vol. 27, no. 6, pp. 511-513, Jun. 2006.

[12] J. M. Luttinger and W. Kohn, “Motion of electrons and holes in perturbed periodic fields,” *Phys. Rev.*, vol. 97, pp. 869-883, Feb. 1955.

[13] G. L. Bir and G. E. Pikus, “Theory of the deformation potential for semiconductors with a complex band structure,” *Sov. Phys. Solid State*, vol. 2, pp.2287-2300, Sept. 1960.

[14] Y. Sun, S. E. Thompson, and T. Nishida, “Physics of strain effects in semiconductors and metal-oxide-semiconductor field-effect transistors,” *J. Appl. Phys.*, vol. 101, no. 10, p. 104503, May 2007.

[15] M. V. Fischetti and S. E. Laux, “Band structure, deformation potentials, and carrier mobility in strained Si, Ge, and SiGe alloys,” *J. Appl. Phys.*, vol. 80, no. 4, pp. 2234-2252, Aug. 1996.

[16] R. Oberhuber, G. Zandler, and P. Vogl, “Subband structure and mobility of two-dimensional holes in strained Si/SiGe MOSFET’s,” *Phys. Rev. B*, vol. 58, no. 15, pp. 9941-9948, Oct. 1998.

[17] L. D. Laude, F. H. Pollak, and M. Cardona, “Effects of uniaxial stress on the indirect exciton spectrum of silicon,” *Phys. Rev. B*, vol. 3, no. 8, pp. 2623-2636, Apr. 1971.

[18] M. Tiersten, “Acoustic-mode scattering mobility of holes in diamond type semiconductors,” *J. Phys. Chem. Solids*, vol. 25, pp. 1151-1168, Nov. 1964.

[19] P. Lawaetz, “Low-field mobility and galvanomagnetic properties of holes in germanium with phonon scattering,” *Phys. Rev.*, vol. 174, no. 3, pp. 867-880, Oct. 1968.

[20] C. Jacoboni and L. Reggiani, “The Monte Carlo method for the solution of charge transport in semiconductors with applications to covalent materials,” *Rev. Mod. Phys.*, vol. 55, no. 3, pp. 645-705, Jul. 1983.

[21] C. J. Tang, S. H. Huang, T. Wang, and C. S. Chang, “Investigation of the strained PMOS on (110) substrate,” in *VLSI-TSA*, 2007, pp. 1-2.

[22] S. Takagi, A. Toriumi, M. Iwase, and H. Tango, “On the universality of inversion layer mobility in Si MOSFET's: Part I-effects of substrate impurity concentration,” *IEEE Trans. Electron Devices*, vol. 41, no. 12, pp. 2357-2362, Dec. 1994.

[23] K. Rim, K. Chan, L. Shi, D. Boyd, J. Ott, N. Klymko, F. Cardone, L. Tai, S. Koester, M. Cobb, D. Canaperi, B. To, E. Duch, I. Babich, R. Carruthers, P. Saunders, G. Walker, Y. Zhang, M. Steen, and M. Ieong," Fabrication and mobility characteristics of ultrathin strained Si directly on Insulator (SSDOI) MOSFETs," in *IEDM Tech. Dig.*, 2003, pp. 3.1.1-3.1.4.

[24] C. W. Leitz, M. T. Currie, M. L. Lee, Z.-Y. Cheng, D. A. Antoniadis, and E. A. Fitzgerald, “Hole mobility enhancements and alloy scattering-limited mobility in tensile strained Si/SiGe surface channel metal-oxide-semiconductor field-effect transistors,” *J. Appl. Phys.*, vol. 92, no. 7, pp. 3745-3751, Oct. 2002.

[25] J. C. Hensel and G. Feher, “Cyclotron resonance experiments in uniaxially stressed silicon: Valence band inverse mass parameters and deformation potentials,” *Phys. Rev.*, vol. 129, no. 3, pp. 1041-1062, Feb. 1963.

	D_{ac} (eV)	**D_{op} (10^{-8}eV/cm)**	**$\hbar\omega_{op}$ (meV)**	**λ (nm)**	**Δ (nm)**	**a_v (eV)**	**b (eV)**	**d (eV)**	**d_0 (eV)**
Section 5.2 & 5.3 **N_{sub}=1x10^{17}cm^{-3}** **T=300K**	**5.62**	**8.5**	**61.2**	**2.6**	**0.42**	**2.46**	**-2.1**	**-4.8**	**41.5**

Table 5.1 List of scattering parameters and Bir-Pikus potentials used in Section 5.2 and 5.3. Notice that the scattering parameters used in Section 5.2 and 5.3 are *assumed to be independent* of the Bir-Pikus potentials a_v, b, and d.

	D_{ac} (eV)	D_{op} (10^{-8}eV/cm)	$\hbar\omega_{op}$ (meV)	λ (nm)	Δ (nm)	a_v (eV)	b (eV)	d (eV)	d_0 (eV)
Section 5.4 **N_{sub}=1x10^{17}cm^{-3}** **T=300K**	**5.62**	**8.5**	**61.2**	**2.6**	**0.42**	**2.46**	**-2.1**	**-3.1**	**26.6**

Table 5.2 List of the modified scattering parameters and Bir-Pikus potentials used in Section 5.4.

γ_1	γ_2	γ_3	a_v (eV)	b (eV)	d (eV)	d_0 (eV)	$\Delta_{split-off}$ (eV)
4.285	**0.339**	**1.446**	**2.46**	**-2.1**	**-3.1**	**26.6**	**0.044**
c_{11}	c_{12}	c_{44}	ρ	a_0	v_l	v_t	
	(10^{10} N/m^2)		(g/cm^3)	(Å)	(10^5 cm/sec)		
16.6	**6.41**	**7.94**	**2.329**	**5.43**	**9.04**	**5.41**	

Table 5.3 Material parameters used in Section 5.4. γ_1, γ_1, and γ_1 are Luttinger parameters; a_v, b, and d are the Bir-Pikus potentials; d_0 is the optical deformation potential; $\Delta_{split-off}$ is the split-off hole energy; c_{11}, c_{12}, and c_{44} are the elastic coefficients; ρ and a_0 are the crystal density and lattice constant of silicon; v_l and v_t are the longitudinal and transverse sound velocity.

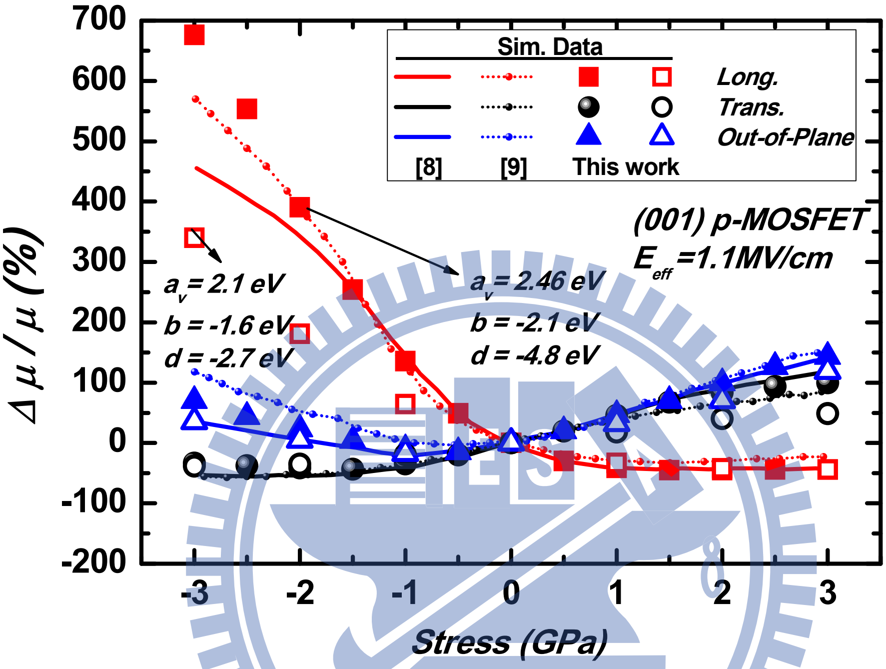

Fig. 5.1 Calculated 3-D uniaxial stress dependence of hole inversion-layer mobility change for different deformation potentials on (001) substrate. Comparison is done with other groups [8], [9]. The Bir-Pikus potentials a_v=2.1 eV, b=-1.6 eV, and d=-2.7 eV are cited in [6].

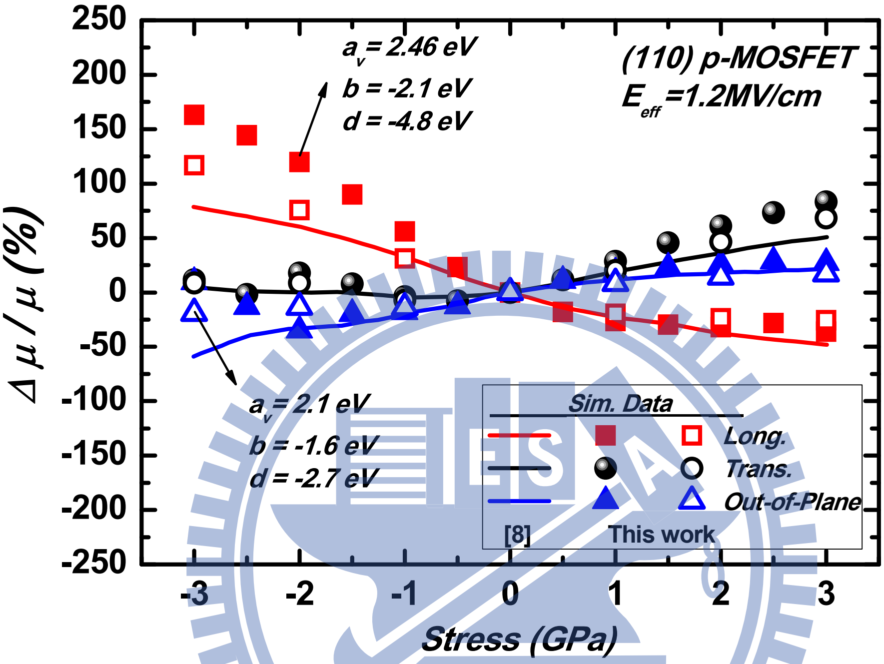

Fig. 5.2 Calculated 3-D uniaxial stress dependence of hole inversion-layer mobility change for different deformation potentials on (110) substrate. Comparison is done with other groups [8]. The Bir-Pikus potentials a_v=2.1 eV, b=-1.6 eV, and d=-2.7 eV are quoted in [6].

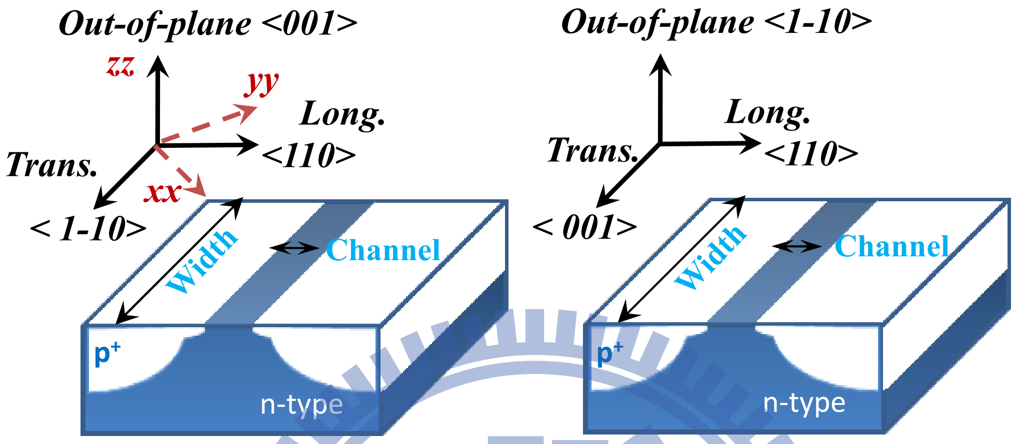

(001) wafer **(110) wafer**

Fig. 5.3 The device structures for (001) and (110) p-MOSFETs. The channel direction and applied stress direction are clarified. Here, three-dimensional in-plane longitudinal, transverse and out-of-plane stress are involved in this dissertation.

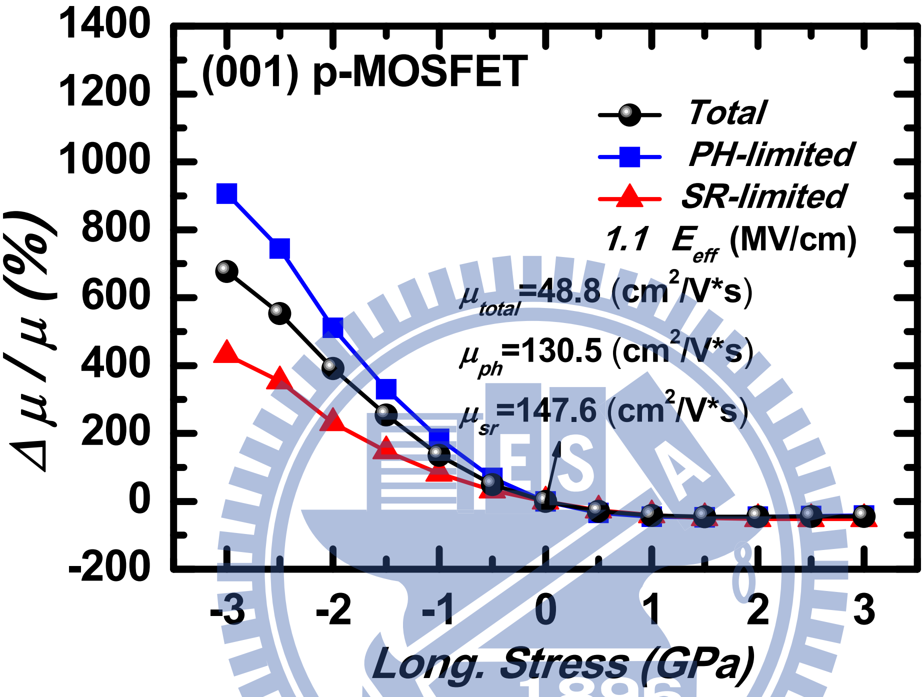

Fig. 5.4 Mobility enhancement under longitudinal stress for different mobility components such as phonon- and surface-roughness-limited ones at E_{eff} = 1.1MV/cm in (001) p-MOSFET.

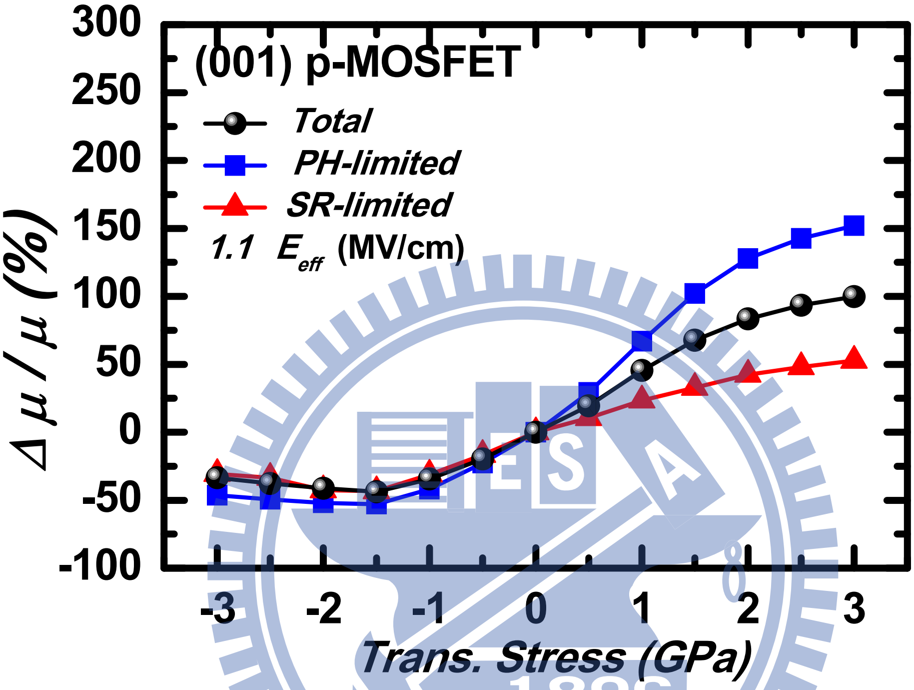

Fig. 5.5 Mobility enhancement under transverse stress for different mobility components such as phonon- and surface-roughness-limited ones at E_{eff} = 1.1MV/cm in (001) p-MOSFET.

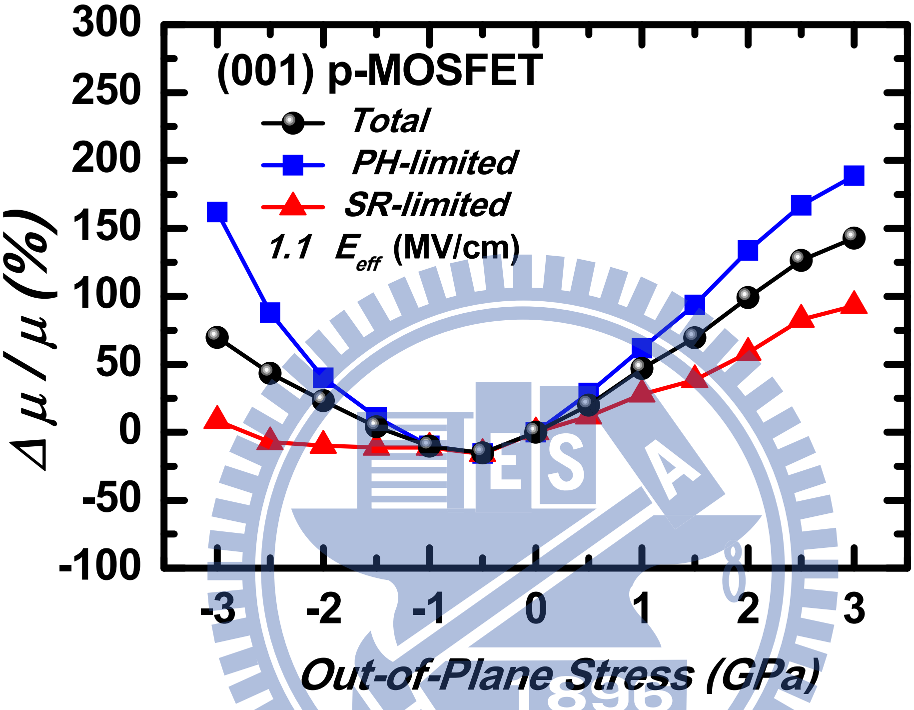

Fig. 5.6 Mobility enhancement under out-of-plane stress for different mobility components such as phonon- and surface-roughness-limited ones at E_{eff} = 1.1MV/cm in (001) p-MOSFET.

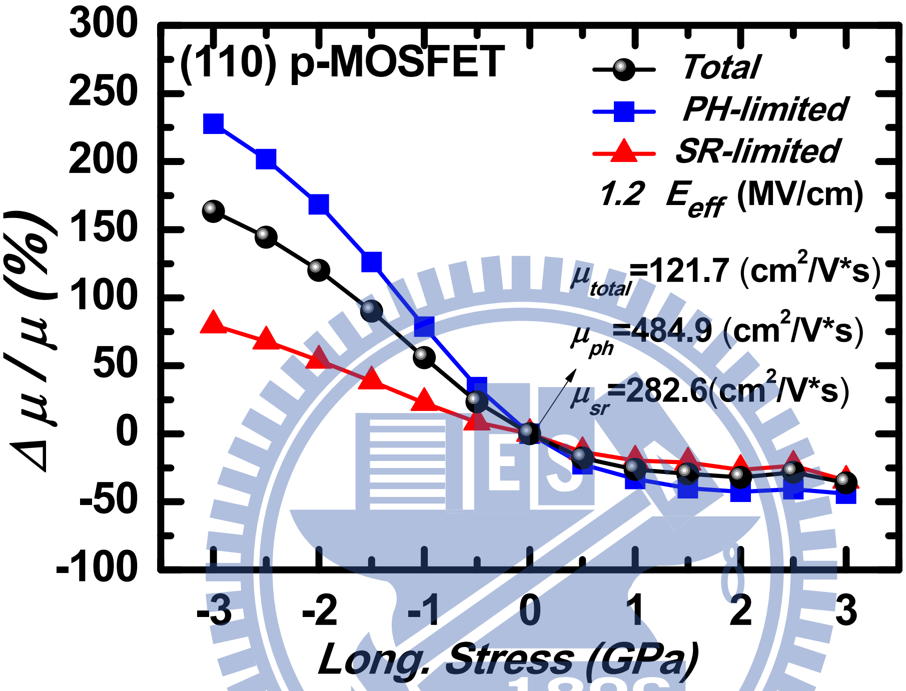

Fig. 5.7 Mobility enhancement under longitudinal stress for different mobility components such as phonon- and surface-roughness-limited ones at E_{eff} = 1.2MV/cm in (110) p-MOSFET.

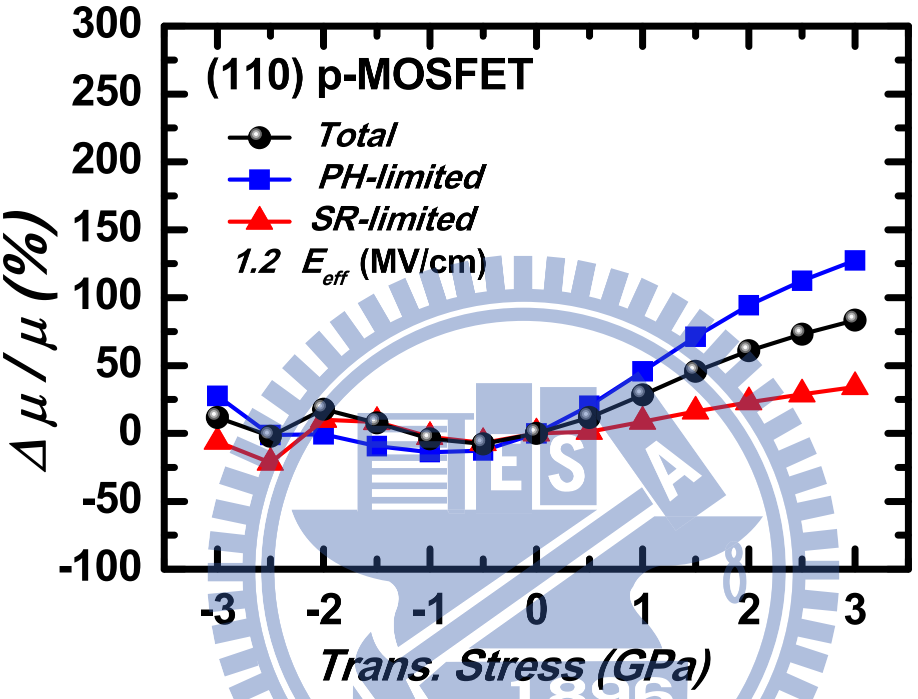

Fig. 5.8 Mobility enhancement under transverse stress for different mobility components such as phonon- and surface-roughness-limited ones at E_{eff} = 1.2MV/cm in (110) p-MOSFET.

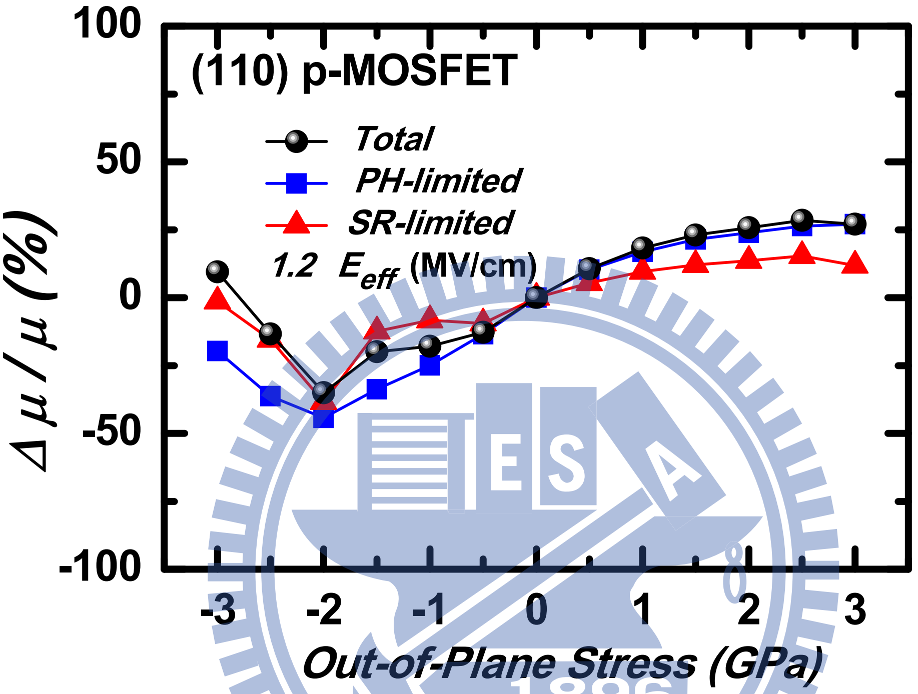

Fig. 5.9 Mobility enhancement under out-of-plane stress for different mobility components such as phonon- and surface-roughness-limited ones at E_{eff} = 1.2MV/cm in (110) p-MOSFET.

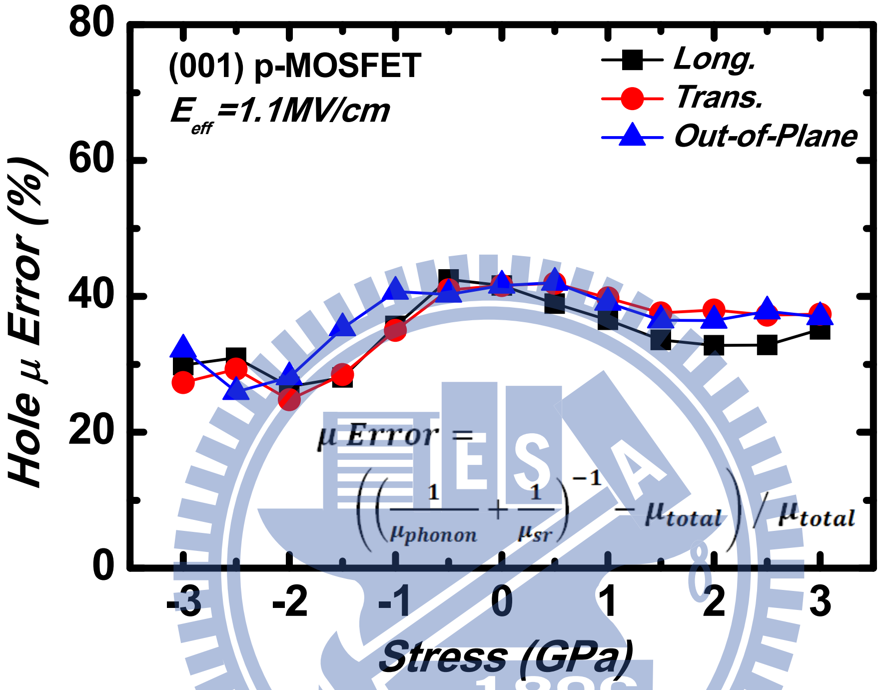

Fig. 5.10 The error of Matthiessen's rule for three-dimensional uniaxial stresses at E_{eff} = 1.1MV/cm in (001) p-MOSFET.

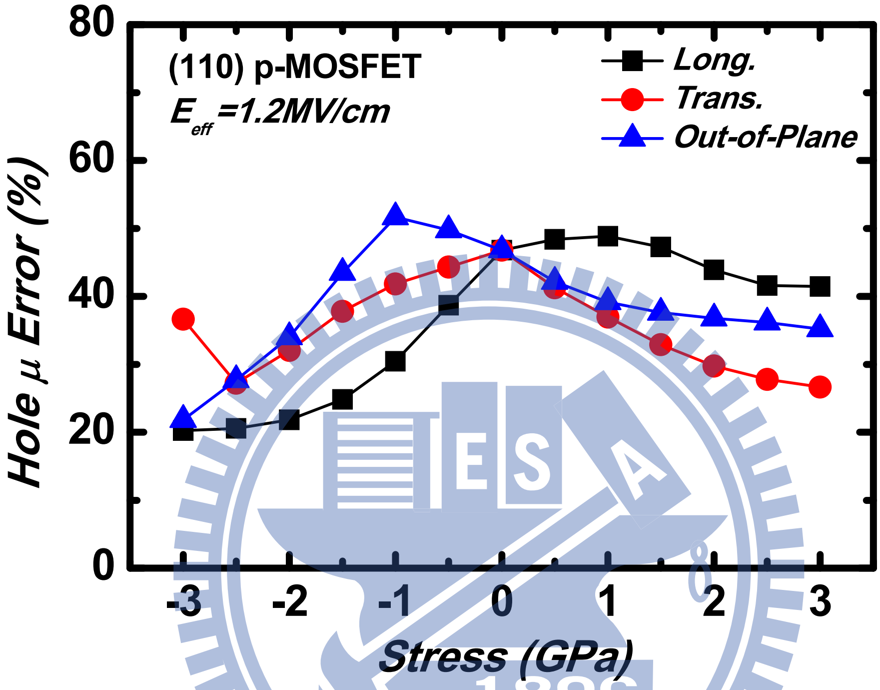

Fig. 5.11 The error of Matthiessen's rule for three-dimensional uniaxial stresses at E_{eff} = 1.2MV/cm in (110) p-MOSFET.

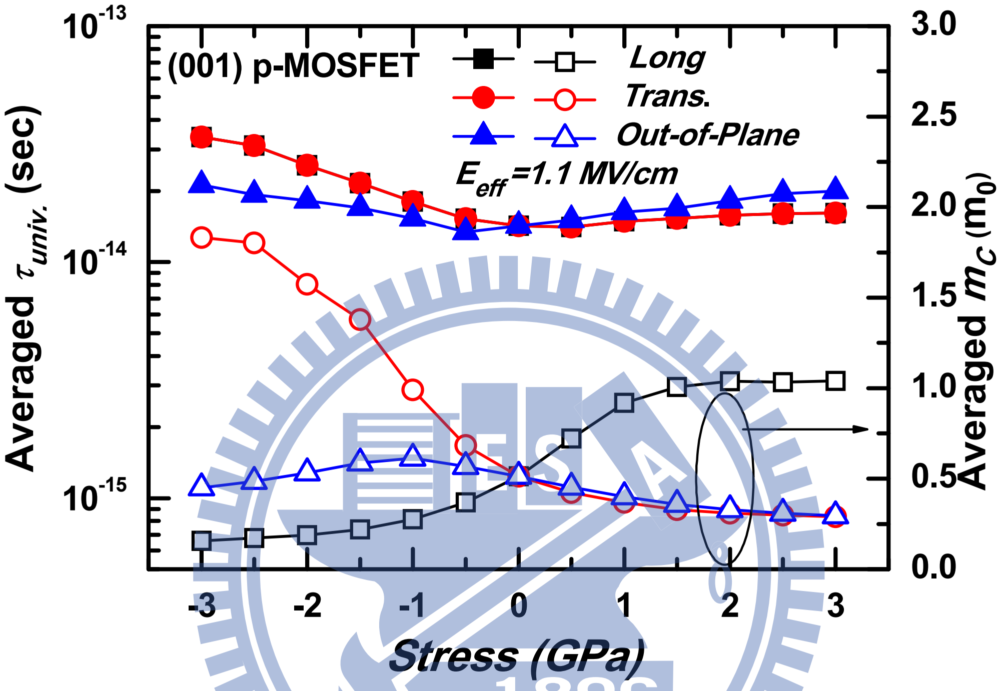

Fig. 5.12 Average scattering time and the extracted conductivity effective masses for three-dimensional uniaxial stresses in (001) p-MOSFET at E_{eff} = 1.1MV/cm.

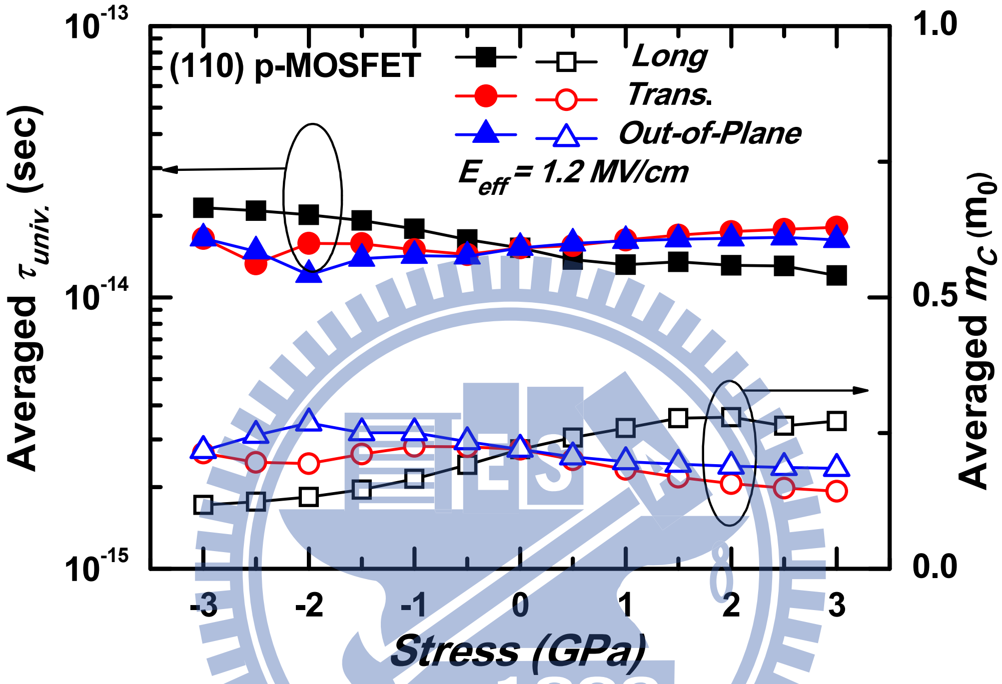

Fig. 5.13 Average scattering time and the extracted conductivity effective masses for three-dimensional uniaxial stresses in (110) p-MOSFET at E_{eff} = 1.2MV/cm.

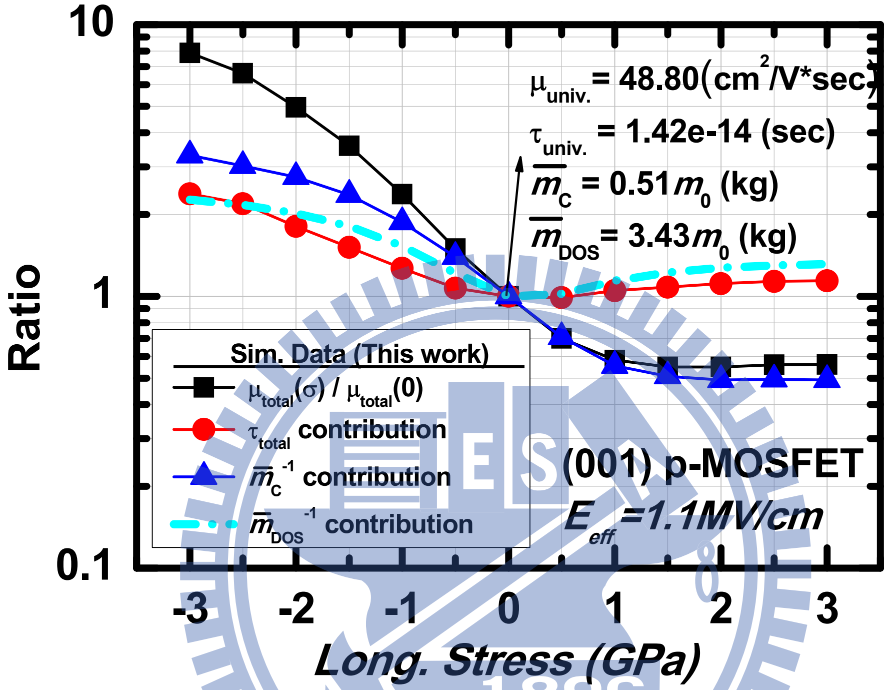

Fig. 5.14 The ratio of total mobility, average scattering time, reciprocal of conductivity effective mass and density-of-states effective mass under longitudinal stress in (001) p-MOSFET at E_{eff} = 1.1MV/cm.

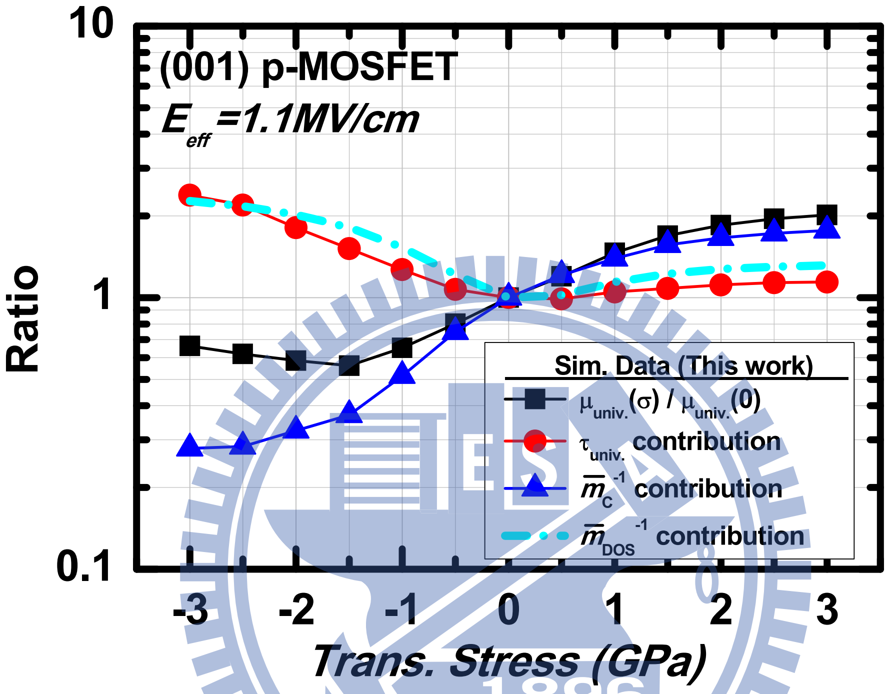

Fig. 5.15 The ratio of total mobility, average scattering time, reciprocal of conductivity effective mass and density-of-states effective mass under transverse stress in (001) p-MOSFET at $E_{eff} = 1.1$MV/cm.

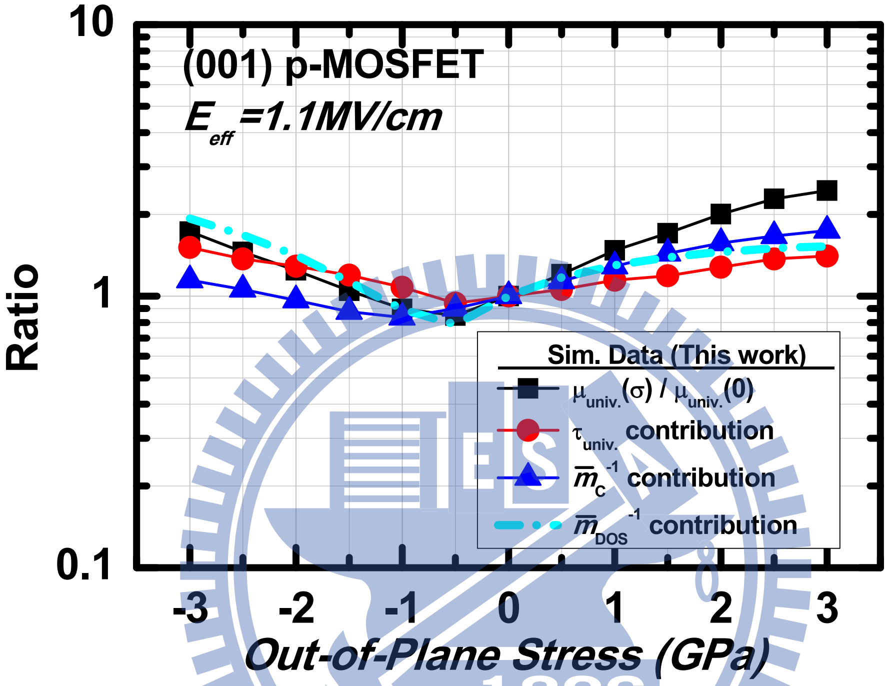

Fig. 5.16 The ratio of total mobility, average scattering time, reciprocal of conductivity effective mass and density-of-states effective mass under out-of-plane uniaxial stress in (001) p-MOSFET at E_{eff} = 1.1MV/cm.

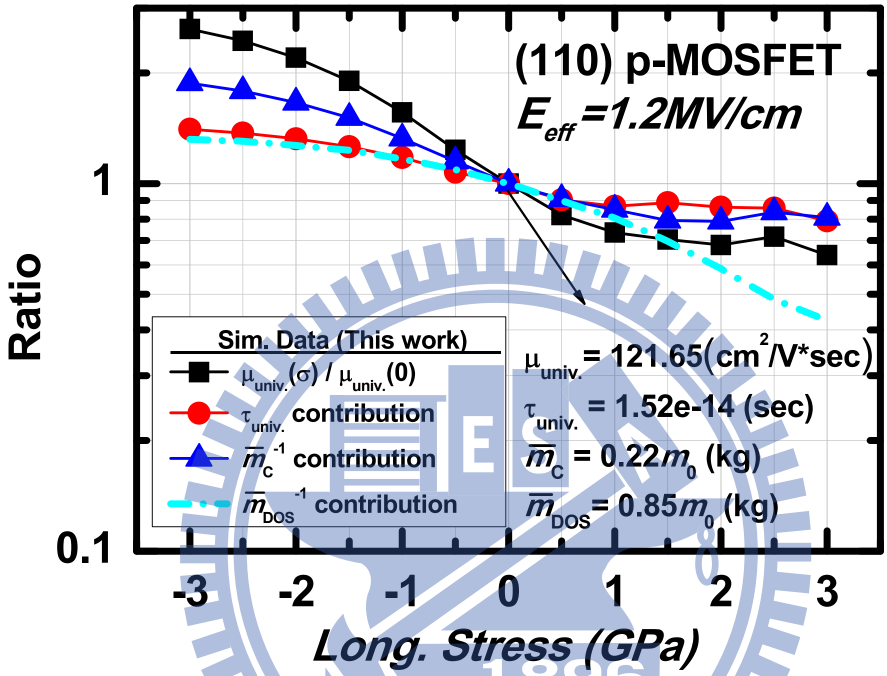

Fig. 5.17 The ratio of total mobility, average scattering time, reciprocal of conductivity effective mass and density-of-states effective mass under longitudinal uniaxial stress in (110) p-MOSFET at E_{eff} = 1.2MV/cm.

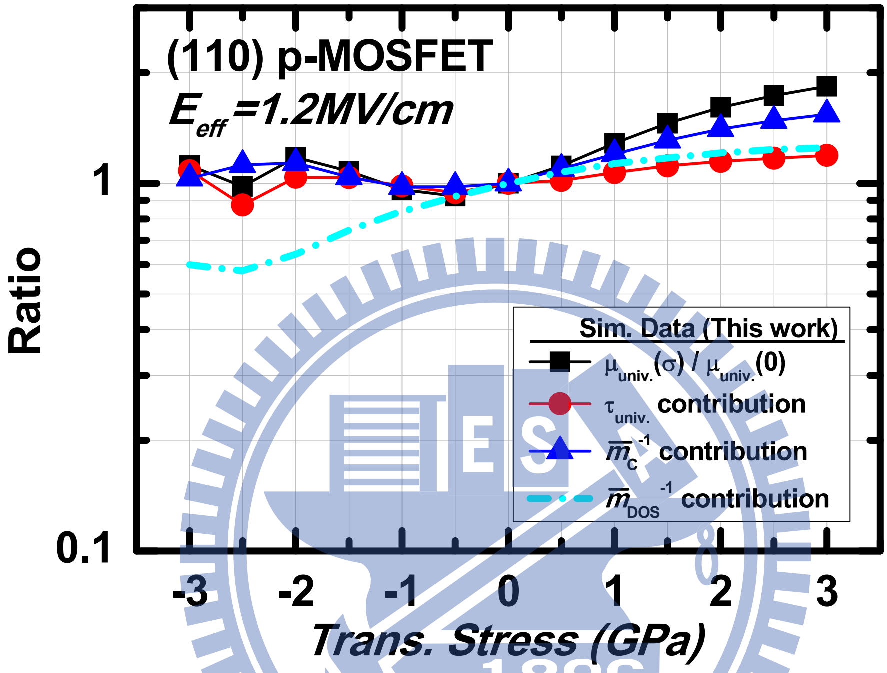

Fig. 5.18 The ratio of total mobility, average scattering time, reciprocal of conductivity effective mass and density-of-states effective mass under transverse uniaxial stress in (110) p-MOSFET at E_{eff} = 1.2MV/cm.

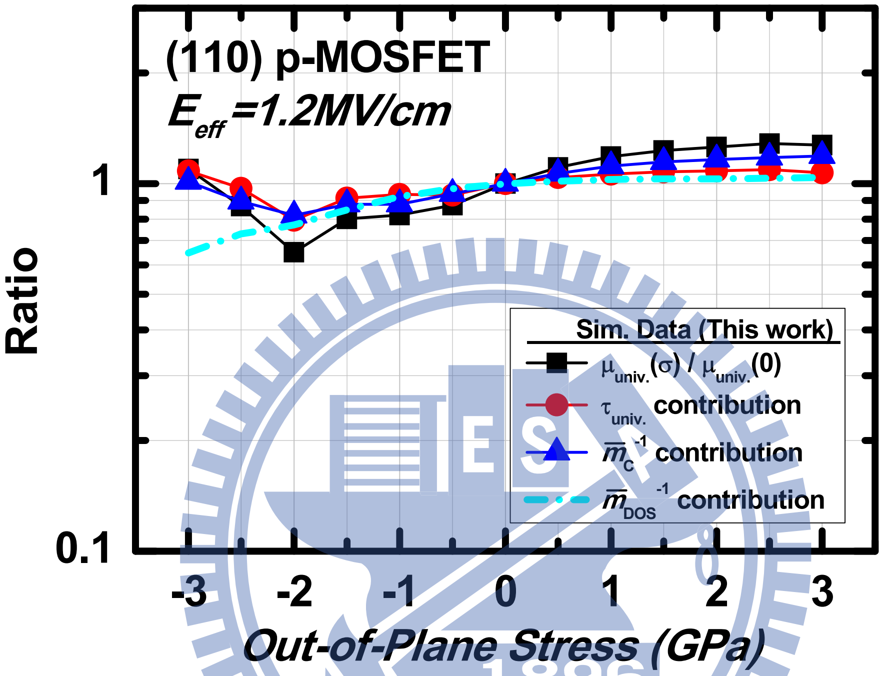

Fig. 5.19 The ratio of total mobility, average scattering time, reciprocal of conductivity effective mass and density-of-states effective mass under out-of-plane uniaxial stress in (110) p-MOSFET at E_{eff} = 1.2MV/cm.

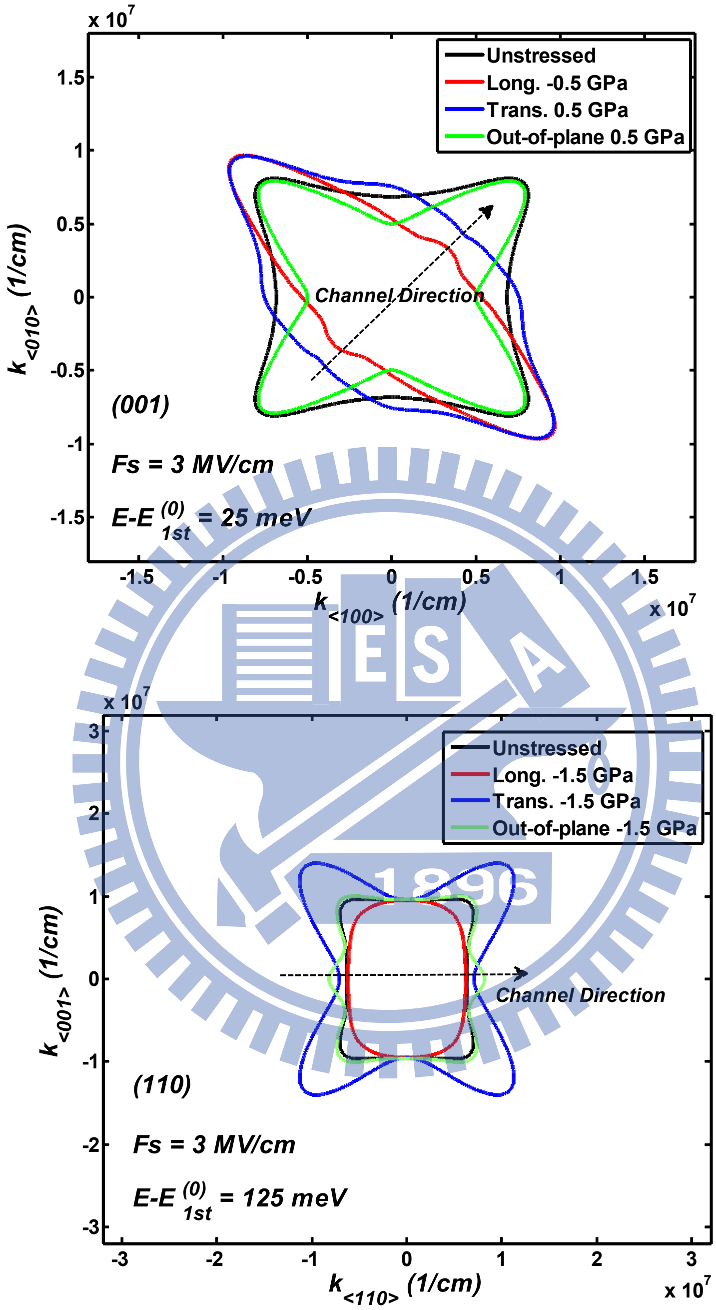

Fig. 5.20 Calculated heavy-hole-like valence subband structures under the out-of-plane quantum confinement in the presence of longitudinal, transverse, out-of-plane stresses on (001) and (110) wafer orientations.

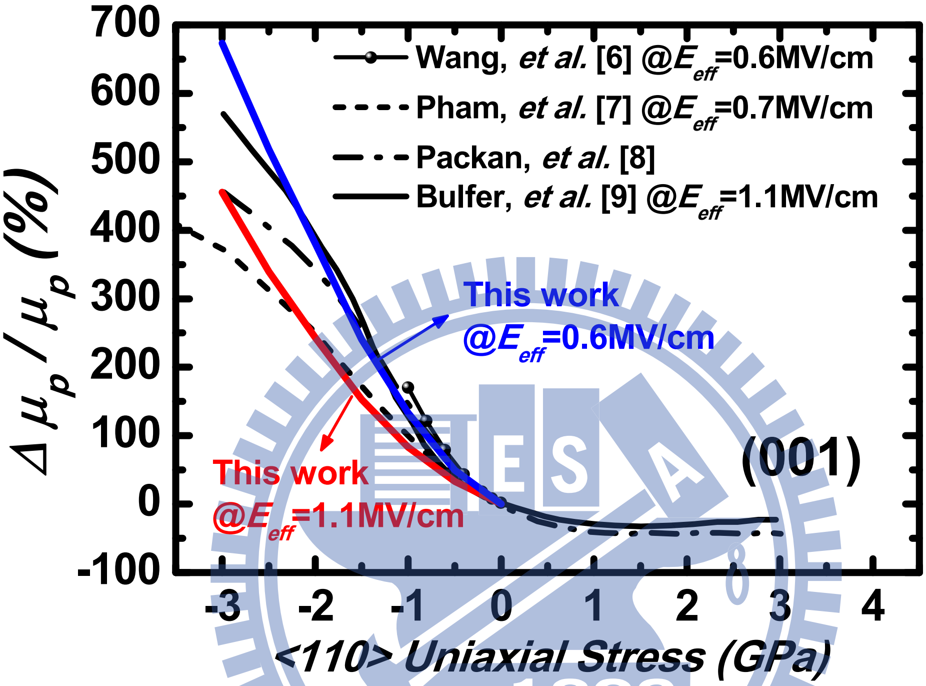

Fig. 5.21 Calculated <110> hole inversion-layer mobility change, from [6]-[9] and this work, plotted versus <110> uniaxial stress on (001) substrate.

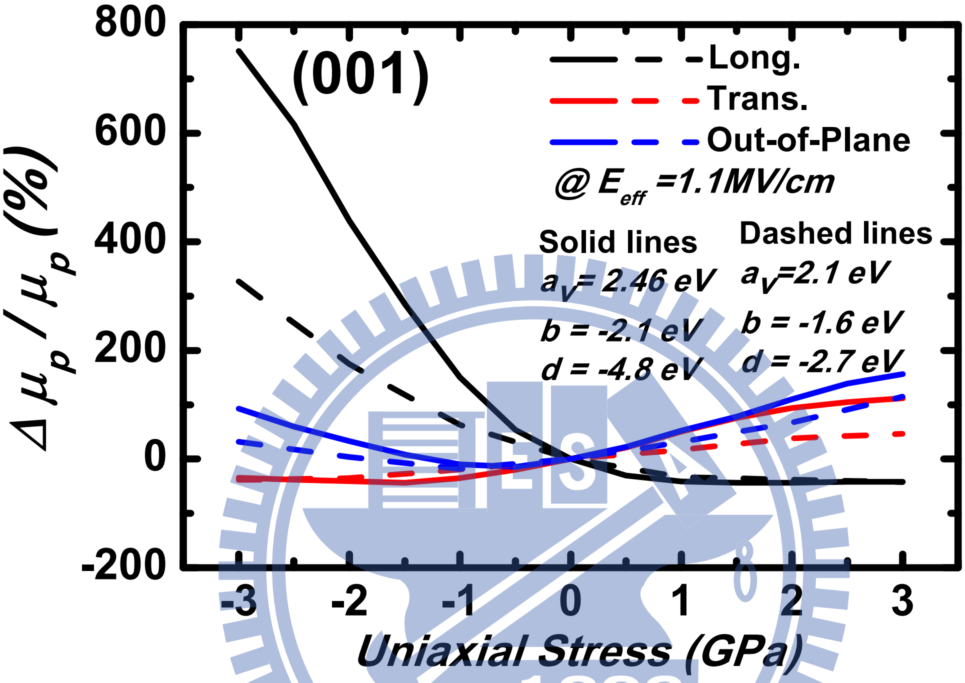

Fig. 5.22(a) Calculated 3-D uniaxial stress dependence of hole inversion-layer mobility change for (001) substrate.

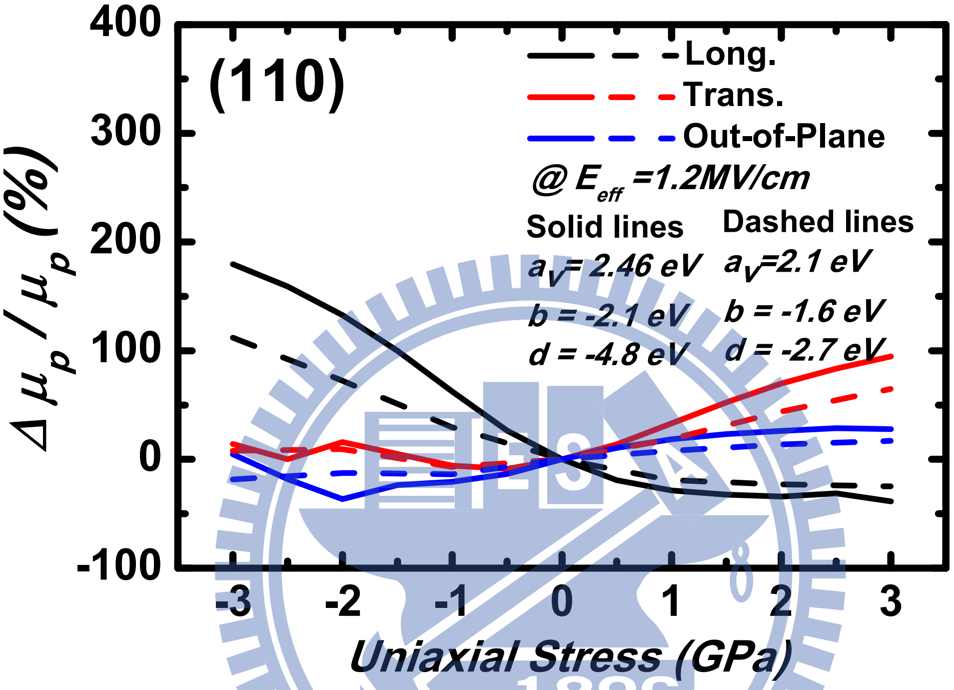

Fig. 5.22(b) Calculated 3-D uniaxial stress dependence of hole inversion-layer mobility change for (110) substrate.

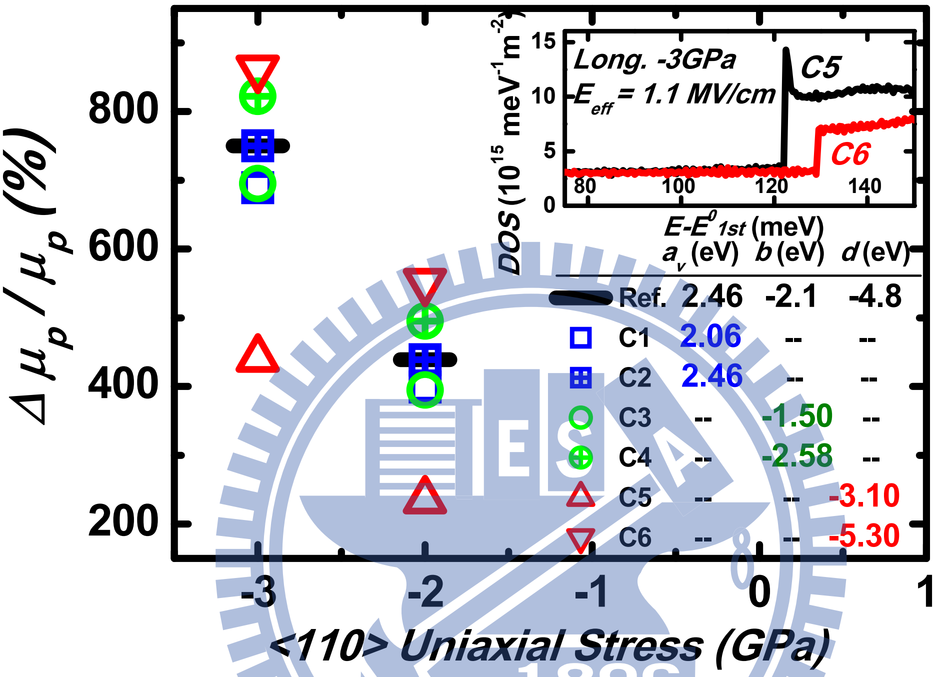

Fig. 5.23 Calculated hole inversion-layer mobility enhancement values at two uniaxial compressive stresses for the reference deformation potentials and six different conditions (C1 to C6). The inset shows calculated DOS of 2 lowest subbands for C5 and C6.

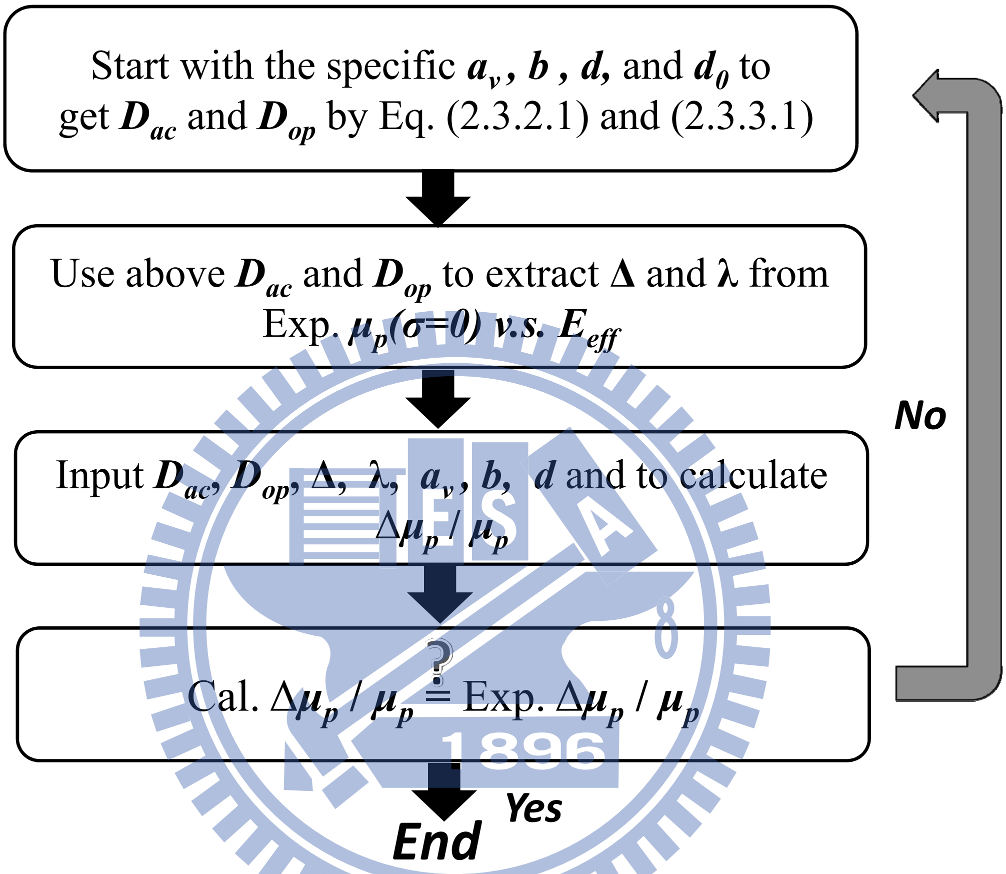

Fig. 5.24 Flowchart showing the establishment of the guidelines with the mutual coupling between the Bir-Pikus deform potentials and D_{ac} taken into account.

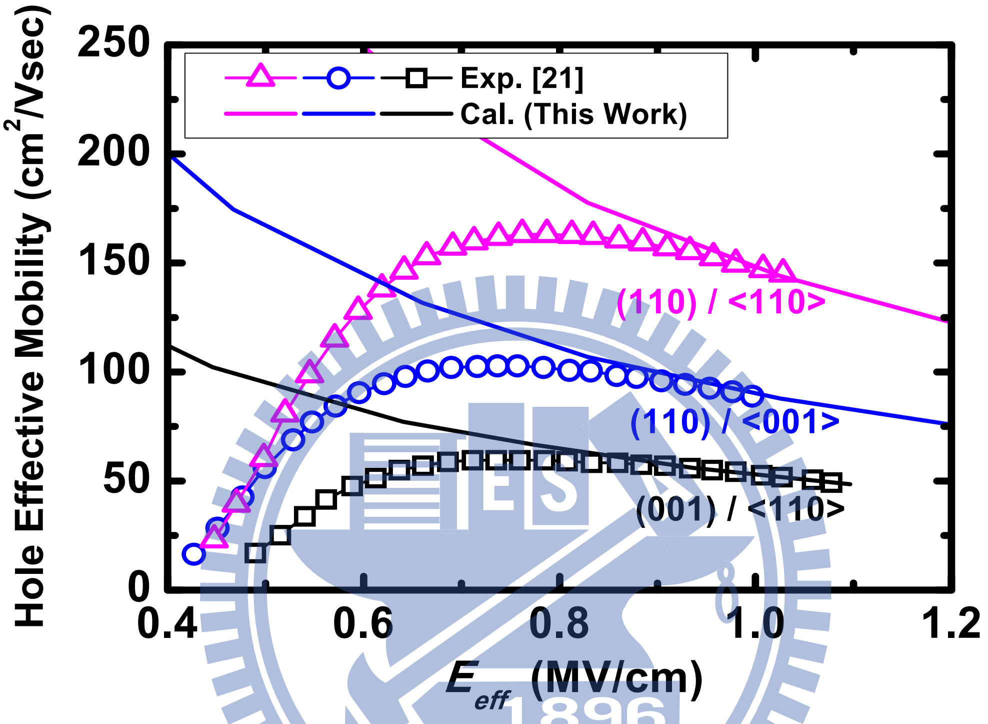

Fig. 5.25 Comparison of experimental hole inversion-layer effective mobility (symbols) [21] and calculated hole universal mobility (lines) versus vertical effective electric field. The scattering parameters used are listed in Table 5.2 and apply to both (001) and (110) substrates.

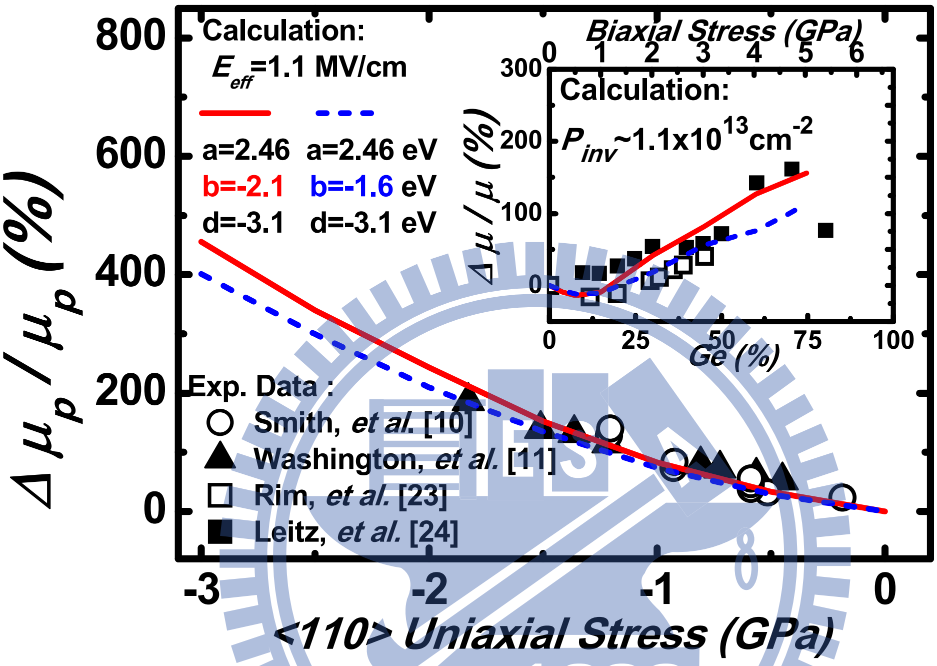

Fig. 5.26 Experimental (symbols) <110> hole inversion-layer mobility enhancement [10],[11] versus <110> uniaxial compressive stress on (001) substrate. Calculation results in this work (lines) are shown for comparison. The inset depicts the case of biaxial stress with the experimental data from [23],[24].

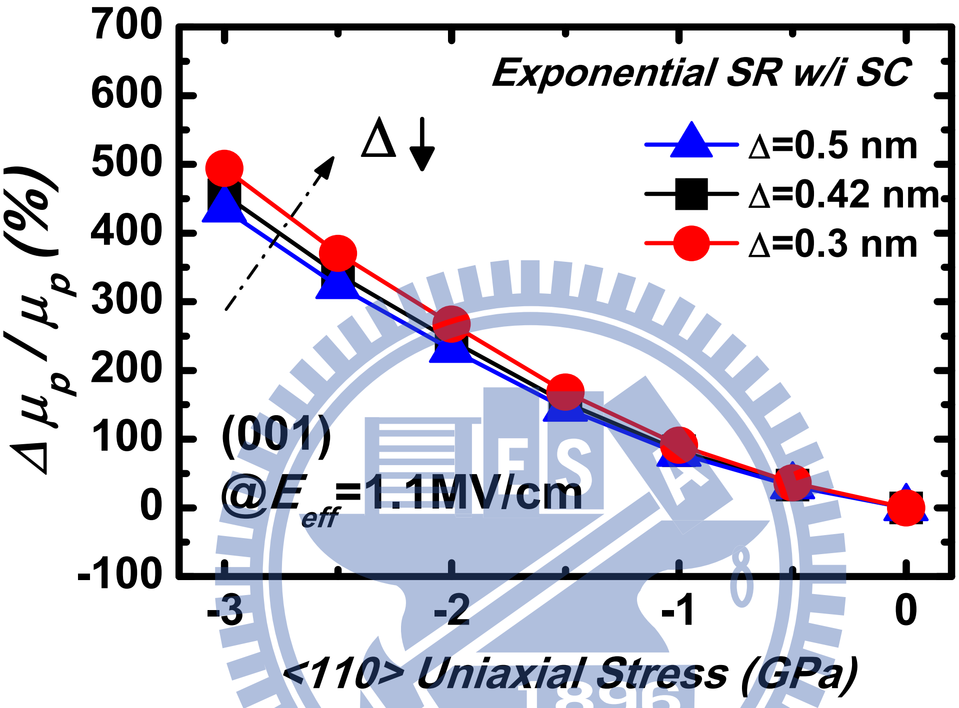

Fig. 5.27 Comparisons of the calculated hole inversion-layer mobility change between the varying range of rms height of the surface roughness from 0.3 to 0.5 nm on (001) substrate with the interesting longitudinal compressive stress.

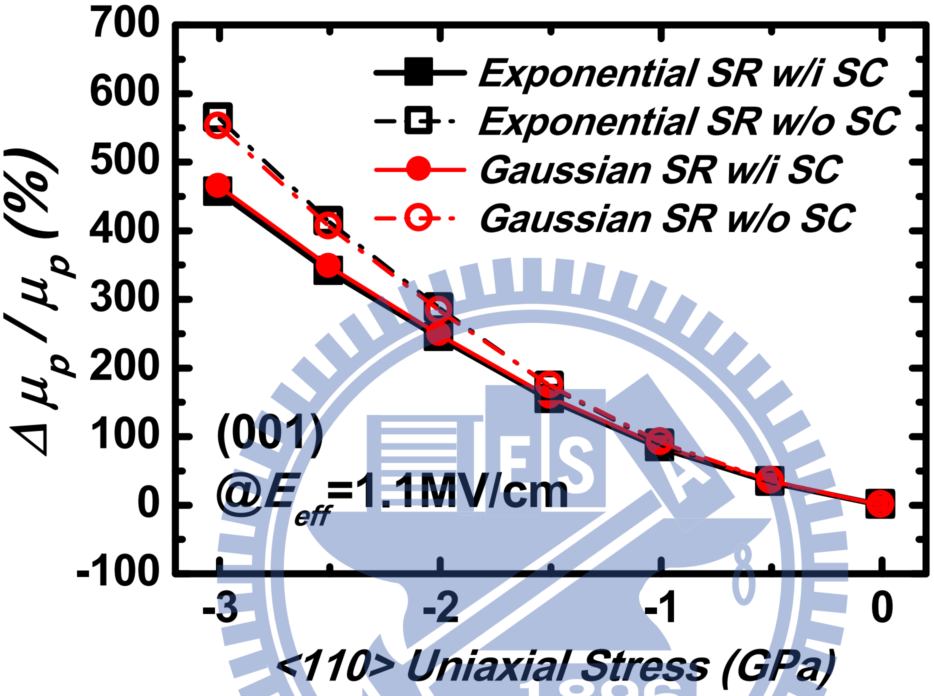

Fig. 5.28 Comparisons of the calculated hole inversion-layer mobility change between the exponential and Gaussian autocovariance function with and without the screening effect on (001) substrate with the interesting longitudinal compressive stress.

Chapter 6

Demonstration of *p*-NEP

6.1 User Interface (UI) and Simulation Process

The numerical techniques and physical models of *p*-NEP have already been introduced in Chapter 2. In this chapter, the user interface and simulation process of *p*-NEP which is written using the well-known software, MatLab, are discussed. In addition, the simulation results are demonstrated as well.

Firstly, the basic structure of the simulator *p*-NEP is shown in Fig. 6.1. It can be seen that the code of *p*-NEP is comprised of four parts: (i) a main program of *p*-NEP which can yield the hole subband structures, Fermi level, confining electrostatic potential profile, and so on in the *p*-type inversion layer; (ii) a hole mobility program which can evaluate the group velocity over all *k*-plane, scattering rates based on the momentum relaxation mechanism, and hole mobility; (iii) a hole gate direct tunneling program which can calculate the hole gate direct tunneling current with the WKB approximation; and (iv) a threshold voltage and capacitance program which can compute the threshold voltage using the linear extrapolation of inversion hole density and the capacitance versus gate voltage using the formula dQ/dV_G.

To the part one, Fig. 6.2 demonstrates the UI for the main program. First of all, we run the m-file named *NEP4.m* in the window of the current folder. Then, the setting parameters are keyed in the command window of MatLab one by one. After completing the input procedure, the popup window for saving path will appear. All simulation results of p-NEP are saved as the type of MatLab data and the data size of one bias point is of around three hundred megabyte. To the part two, the UI for the hole mobility program is displayed in Fig. 6.3. We start by dropping the wanted MatLab data into the same folder and running the m-file named *Sub_Program_Head.m* in the window of current folder. Then, we select the loaded MatLab data and press OK in the popup window. When completing the next popup window for the scattering parameters setting, the hole mobility program will be executed. To the part three, the UI for the gate direct tunneling program is illustrated in Fig. 6.4. The operational procedure is basically the same as that shown in Fig. 6.3, beside the running m-file named *Program_Head.m* and without the second popup window.

To the part four, the UI for the threshold voltage and capacitance programs is in Fig. 6.5. The operational procedure here is divided into two steps: the first step represents the threshold voltage calculation and the second step represents the capacitance calculation. We start by dropping the wanted MatLab data into the same folder and running the m-file named *Program_Head.m* in the window of current folder. Then, select the loaded MatLab data and press OK in the popup window. When the first step is done, the popup figure of the hole inversion density versus gate voltage and the second popup window which should be keyed with the range of the linear extrapolation are shown. After that, the results of the second step will appear in the popup figure as well.

6.2 Demonstration Results

6.2.1 Hole Subband Structure

The simulation results from the part one of *p*-NEP in Fig. 6.1 are shown as follows. Firstly, the triangular potential based hole subband levels, occupancies, and structures in the stressed p-type silicon inversion layer are shown in Fig. 6.6, 6.7 and 6.8, respectively. In Fig. 6.9, 6.10, and 6.11, the fully-iterated (by the six-band $k \cdot p$ Schrödinger-Poisson self-consistent method) energy contours of the first subband with the different materials, silicon, germanium, and gallium arsenide, are illustrated.

6.2.2 Hole Inversion-Layer Mobility

About the part two of *p*-NEP in Fig. 6.1, the hole group velocity of the first subband over all *k*-plane on both (001) and (110) are shown in Fig. 6.12 and 6.13. The corresponding scattering rates versus energy at a specific angle $\theta=0\,^{o}$are shown in Fig. 6.14 and 6.15. In order to see the screening effect as depicted in Eq. (2.3.4.1), Fig. 6.16 shows the (001) and (110) hole inversion-layer mobility with and without screening effect. It is reasonable for the larger screening effect to appear in the stronger inversion layer.

6.2.3 Hole Gate Direct Tunneling and Capacitance

As to the part three and four of *p*-NEP in Fig. 6.1, the simulation results of the hole gate direct tunneling current and capacitance are shown as follows. In Fig. 6.17, the calculated unstressed hole gate direct tunneling current density are found in the satisfactory agreements with the experimental data from [1]. Then, the unstressed and stressed capacitance versus gate voltage can also be satisfactorily compared with the experimental data from [2] where the stressor originated from the selective fully silicided (FUSI) gate, in Fig. 6.18 and Fig. 6.19. More practically, the hole gate direct tunneling current density and capacitance are drawn simultaneously with the varying poly-gate doping concentrations, stress conditions, and metal-gate work functions in Fig. 6.20, 6.21, and 6.22.

References

[1] K. N. Yang, H. T. Huang, M. C. Chang, C. M. Chu, Y. S. Chen, M. J. Chen, Y. M. Lin, M. C. Yu, S. M. Jang, D. C. H. Yu, and M. S. Liang, “A physical model for hole direct tunneling current in p+ poly-gate pMOSFETs with ultrathin gate oxides,” *IEEE Trans. Electron Devices*, vol. **47**, no. 11, pp. 2161-2166, Nov. 2000.

[2] D. W. Lin, M. Wang, M. L. Cheng, Y. M. Sheu, B. Tarng, C. M. Chu, C. W. Nieh, C. P. Lo, W. C. Tsai, R. Lin, S. W. Wang, K. L. Cheng, C. M. Wu, M. T. Lei, C. C. Wu, C. H. Diaz, and M. J. Chen, “A millisecond-anneal-assisted selective fully silicided (FUSI) gate process,” *IEEE Electron Device Lett.*, vol. 29, no. 9, pp. 998–1000, Sept. 2008.

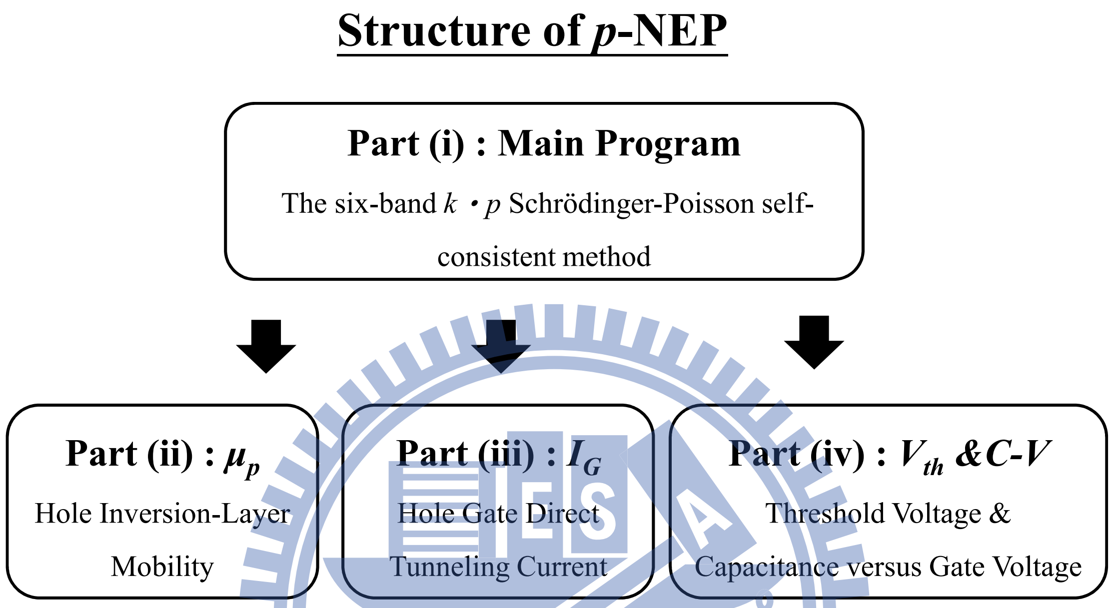

Fig. 6.1 The basic structure of the simulator p-NEP.

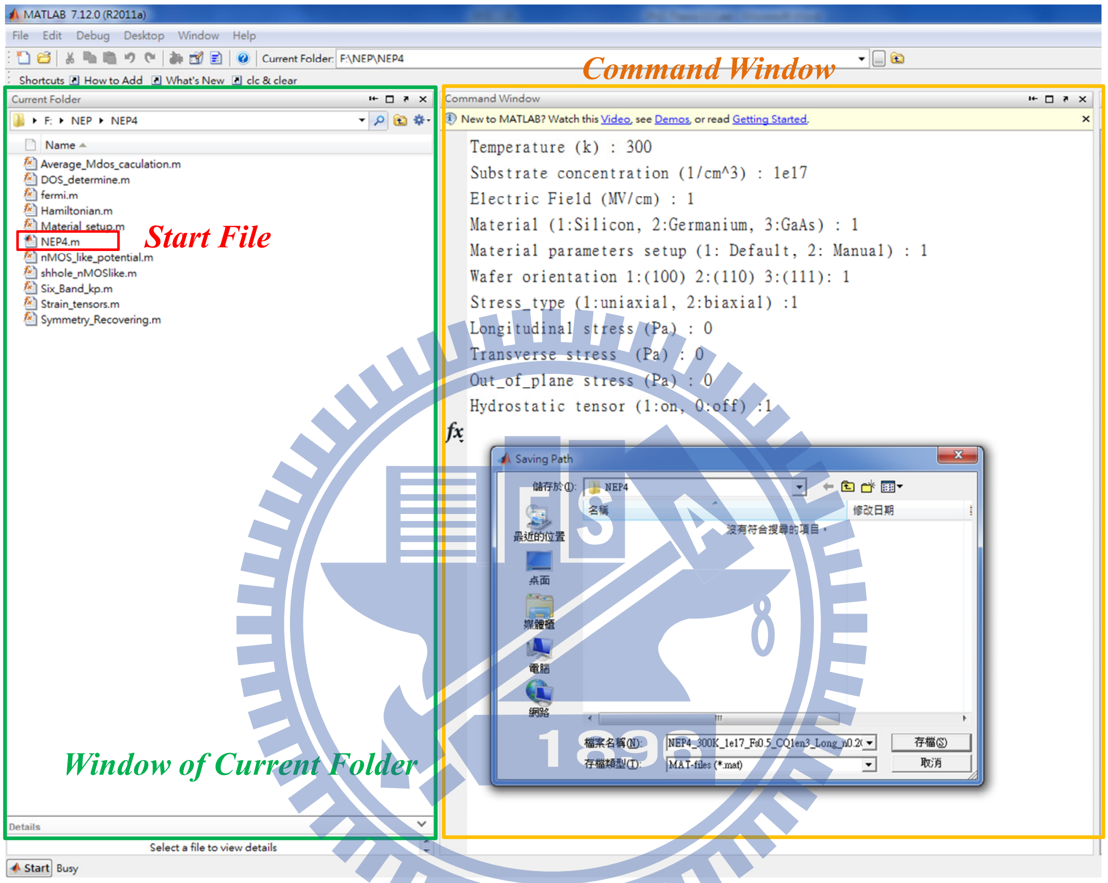

Current Folder: F:\NEP\NEP4

- Average_Mdos_caculation.m
- DOS_determine.m
- fermi.m
- Hamiltonian.m
- Material_setup.m
- NEP4.m
- nMOS_like_potential.m
- shhole_nMOSlike.m
- Six_Band_kp.m
- Strain_tensors.m
- Symmetry_Recovering.m

Select a file to view details

New to MATLAB? Watch this Video, see Demos, or read Getting Started.

```
Temperature (k) : 300
Substrate concentration (1/cm^3) : 1e17
Electric Field (MV/cm) : 1
Material (1:Silicon, 2:Germanium, 3:GaAs) : 1
Material parameters setup (1: Default, 2: Manual) : 1
Wafer orientation 1:(100) 2:(110) 3:(111): 1
Stress_type (1:uniaxial, 2:biaxial) :1
Longitudinal stress (Pa) : 0
Transverse stress  (Pa) : 0
Out_of_plane stress (Pa) : 0
Hydrostatic tensor (1:on, 0:off) :1
```

儲存於(I): NEP4

沒有符合搜尋的項目。

檔案名稱(N): NEP4_300K_1e17_F0.5_CQlen3_Long_n0.2(

存檔類型(T): MAT-files (*.mat)

Fig. 6.2 The UI for the main program of *p*-NEP in Fig. 6.1.

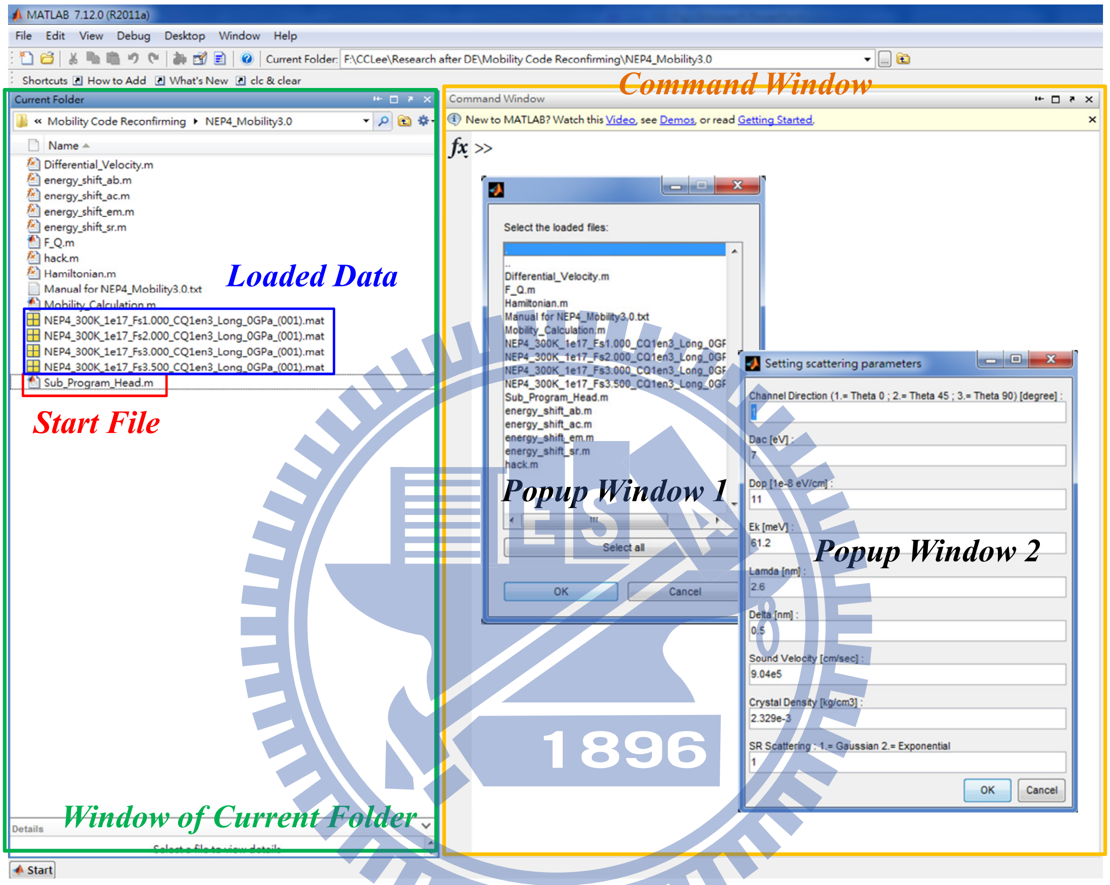

Current Folder: F:\CCLee\Research after DE\Mobility Code Reconfirming\NEP4_Mobility3.0

« Mobility Code Reconfirming ▸ NEP4_Mobility3.0

Name
Differential_Velocity.m
energy_shift_ab.m
energy_shift_ac.m
energy_shift_em.m
energy_shift_sr.m
F_Q.m
hack.m
Hamiltonian.m
Manual for NEP4_Mobility3.0.txt
Mobility_Calculation.m
NEP4_300K_1e17_Fs1.000_CQ1en3_Long_0GPa_(001).mat
NEP4_300K_1e17_Fs2.000_CQ1en3_Long_0GPa_(001).mat
NEP4_300K_1e17_Fs3.000_CQ1en3_Long_0GPa_(001).mat
NEP4_300K_1e17_Fs3.500_CQ1en3_Long_0GPa_(001).mat
Sub_Program_Head.m

New to MATLAB? Watch this Video, see Demos, or read Getting Started.

```
fx >>
```

Select the loaded files:
.
..
Differential_Velocity.m
F_Q.m
Hamiltonian.m
Manual for NEP4_Mobility3.0.txt
Mobility_Calculation.m
NEP4_300K_1e17_Fs1.000_CQ1en3_Long_0GF
NEP4_300K_1e17_Fs2.000_CQ1en3_Long_0GF
NEP4_300K_1e17_Fs3.000_CQ1en3_Long_0GF
NEP4_300K_1e17_Fs3.500_CQ1en3_Long_0GF
Sub_Program_Head.m
energy_shift_ab.m
energy_shift_ac.m
energy_shift_em.m
energy_shift_sr.m
hack.m

Setting scattering parameters

Channel Direction (1.= Theta 0 ; 2.= Theta 45 ; 3.= Theta 90) [degree] : 1
Dac [eV] : 7
Dop [1e-8 eV/cm] : 11
Ek [meV] : 61.2
Lamda [nm] : 2.6
Delta [nm] : 0.5
Sound Velocity [cm/sec] : 9.04e5
Crystal Density [kg/cm3] : 2.329e-3
SR Scattering : 1.= Gaussian 2.= Exponential 1

Fig. 6.3 The UI for the hole inversion-layer mobility program of *p*-NEP in Fig. 6.1.

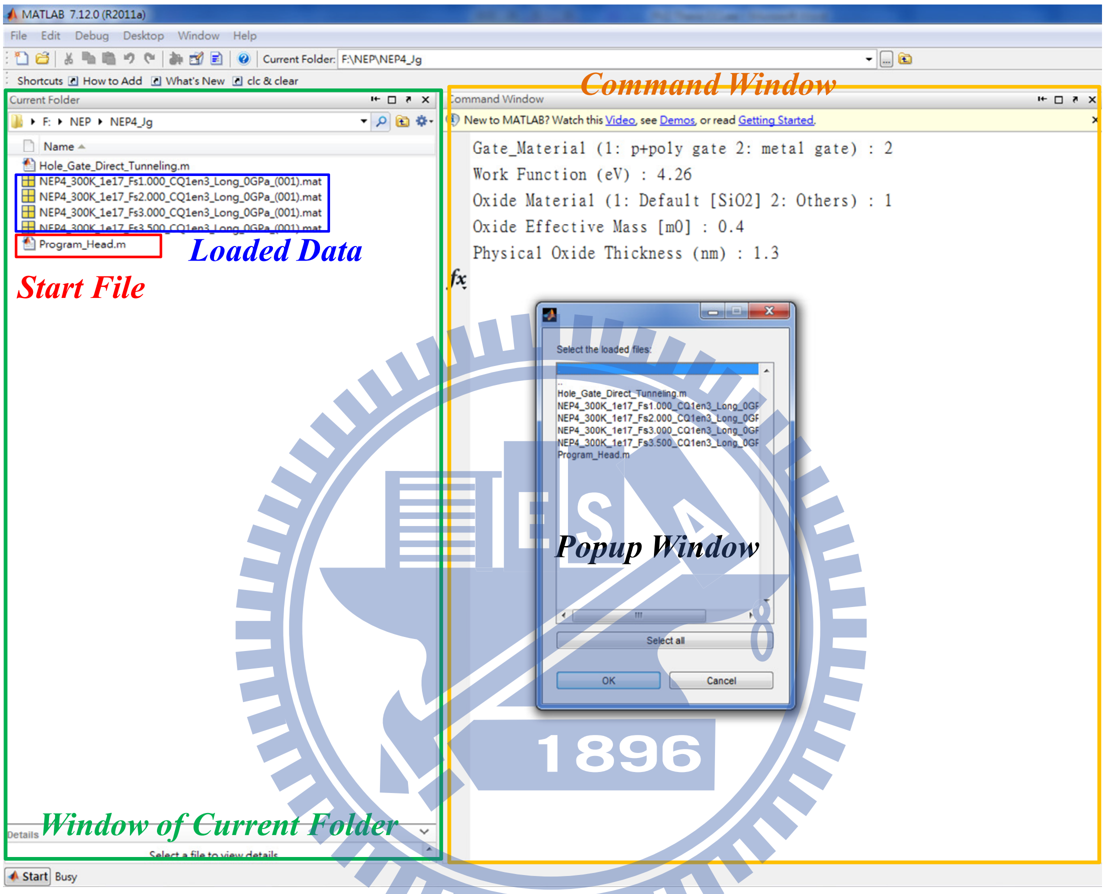

```
Gate_Material (1: p+poly gate 2: metal gate) : 2
Work Function (eV) : 4.26
Oxide Material (1: Default [SiO2] 2: Others) : 1
Oxide Effective Mass [m0] : 0.4
Physical Oxide Thickness (nm) : 1.3
```

Fig. 6.4 The UI for the hole gate direct tunneling program of *p*-NEP in Fig. 6.1.

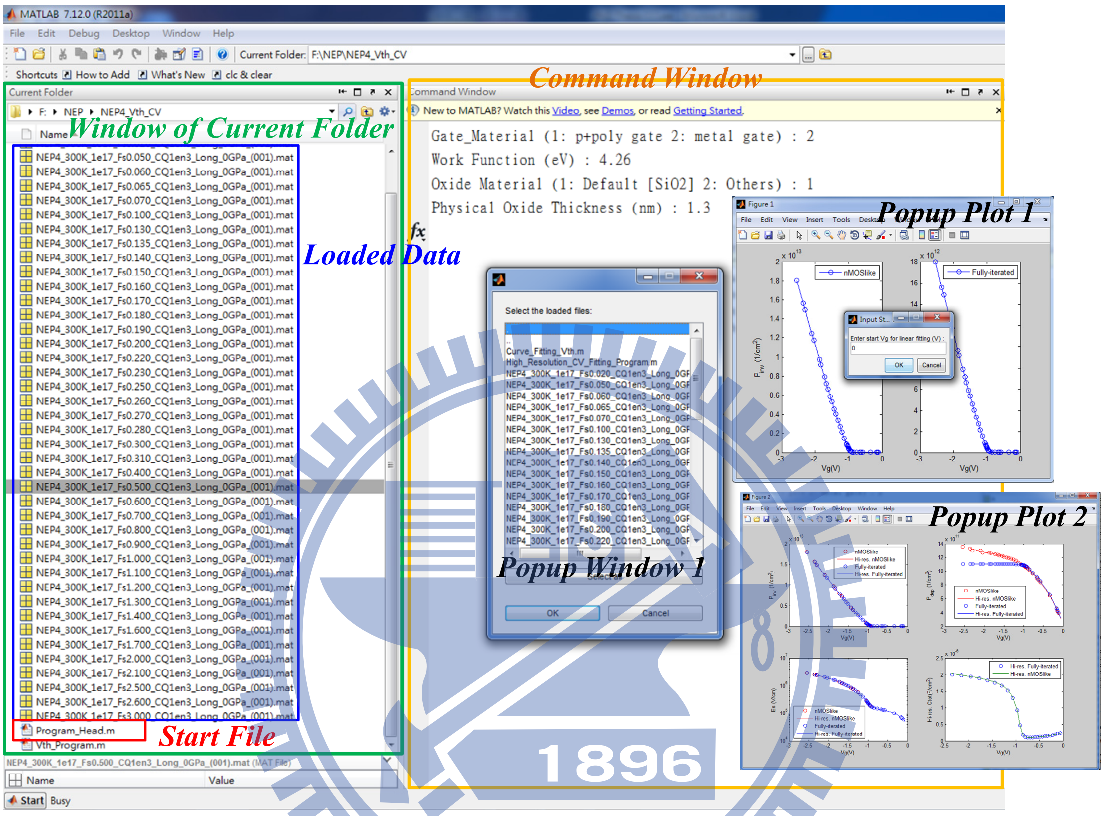

Current Folder: F:\NEP\NEP4_Vth_CV

```
NEP4_300K_1e17_Fs0.050_CQ1en3_Long_0GPa_(001).mat
NEP4_300K_1e17_Fs0.060_CQ1en3_Long_0GPa_(001).mat
NEP4_300K_1e17_Fs0.065_CQ1en3_Long_0GPa_(001).mat
NEP4_300K_1e17_Fs0.070_CQ1en3_Long_0GPa_(001).mat
NEP4_300K_1e17_Fs0.100_CQ1en3_Long_0GPa_(001).mat
NEP4_300K_1e17_Fs0.130_CQ1en3_Long_0GPa_(001).mat
NEP4_300K_1e17_Fs0.135_CQ1en3_Long_0GPa_(001).mat
NEP4_300K_1e17_Fs0.140_CQ1en3_Long_0GPa_(001).mat
NEP4_300K_1e17_Fs0.150_CQ1en3_Long_0GPa_(001).mat
NEP4_300K_1e17_Fs0.160_CQ1en3_Long_0GPa_(001).mat
NEP4_300K_1e17_Fs0.170_CQ1en3_Long_0GPa_(001).mat
NEP4_300K_1e17_Fs0.180_CQ1en3_Long_0GPa_(001).mat
NEP4_300K_1e17_Fs0.190_CQ1en3_Long_0GPa_(001).mat
NEP4_300K_1e17_Fs0.200_CQ1en3_Long_0GPa_(001).mat
NEP4_300K_1e17_Fs0.220_CQ1en3_Long_0GPa_(001).mat
NEP4_300K_1e17_Fs0.230_CQ1en3_Long_0GPa_(001).mat
NEP4_300K_1e17_Fs0.250_CQ1en3_Long_0GPa_(001).mat
NEP4_300K_1e17_Fs0.260_CQ1en3_Long_0GPa_(001).mat
NEP4_300K_1e17_Fs0.270_CQ1en3_Long_0GPa_(001).mat
NEP4_300K_1e17_Fs0.280_CQ1en3_Long_0GPa_(001).mat
NEP4_300K_1e17_Fs0.300_CQ1en3_Long_0GPa_(001).mat
NEP4_300K_1e17_Fs0.310_CQ1en3_Long_0GPa_(001).mat
NEP4_300K_1e17_Fs0.400_CQ1en3_Long_0GPa_(001).mat
NEP4_300K_1e17_Fs0.500_CQ1en3_Long_0GPa_(001).mat
NEP4_300K_1e17_Fs0.600_CQ1en3_Long_0GPa_(001).mat
NEP4_300K_1e17_Fs0.700_CQ1en3_Long_0GPa_(001).mat
NEP4_300K_1e17_Fs0.800_CQ1en3_Long_0GPa_(001).mat
NEP4_300K_1e17_Fs0.900_CQ1en3_Long_0GPa_(001).mat
NEP4_300K_1e17_Fs1.000_CQ1en3_Long_0GPa_(001).mat
NEP4_300K_1e17_Fs1.100_CQ1en3_Long_0GPa_(001).mat
NEP4_300K_1e17_Fs1.200_CQ1en3_Long_0GPa_(001).mat
NEP4_300K_1e17_Fs1.300_CQ1en3_Long_0GPa_(001).mat
NEP4_300K_1e17_Fs1.400_CQ1en3_Long_0GPa_(001).mat
NEP4_300K_1e17_Fs1.600_CQ1en3_Long_0GPa_(001).mat
NEP4_300K_1e17_Fs1.700_CQ1en3_Long_0GPa_(001).mat
NEP4_300K_1e17_Fs2.000_CQ1en3_Long_0GPa_(001).mat
NEP4_300K_1e17_Fs2.100_CQ1en3_Long_0GPa_(001).mat
NEP4_300K_1e17_Fs2.500_CQ1en3_Long_0GPa_(001).mat
NEP4_300K_1e17_Fs2.600_CQ1en3_Long_0GPa_(001).mat
NEP4_300K_1e17_Fs3.000_CQ1en3_Long_0GPa_(001).mat
Program_Head.m
Vth_Program.m
```

NEP4_300K_1e17_Fs0.500_CQ1en3_Long_0GPa_(001).mat (MAT File)

New to MATLAB? Watch this Video, see Demos, or read Getting Started.

```
Gate_Material (1: p+poly gate 2: metal gate) : 2
Work Function (eV) : 4.26
Oxide Material (1: Default [SiO2] 2: Others) : 1
Physical Oxide Thickness (nm) : 1.3
```

Select the loaded files:

```
.
..
Curve_Fitting_Vth.m
High_Resolution_CV_Fitting_Program.m
NEP4_300K_1e17_Fs0.020_CQ1en3_Long_0GF
NEP4_300K_1e17_Fs0.050_CQ1en3_Long_0GF
NEP4_300K_1e17_Fs0.060_CQ1en3_Long_0GF
NEP4_300K_1e17_Fs0.065_CQ1en3_Long_0GF
NEP4_300K_1e17_Fs0.070_CQ1en3_Long_0GF
NEP4_300K_1e17_Fs0.100_CQ1en3_Long_0GF
NEP4_300K_1e17_Fs0.130_CQ1en3_Long_0GF
NEP4_300K_1e17_Fs0.135_CQ1en3_Long_0GF
NEP4_300K_1e17_Fs0.140_CQ1en3_Long_0GF
NEP4_300K_1e17_Fs0.150_CQ1en3_Long_0GF
NEP4_300K_1e17_Fs0.160_CQ1en3_Long_0GF
NEP4_300K_1e17_Fs0.170_CQ1en3_Long_0GF
NEP4_300K_1e17_Fs0.180_CQ1en3_Long_0GF
NEP4_300K_1e17_Fs0.190_CQ1en3_Long_0GF
NEP4_300K_1e17_Fs0.200_CQ1en3_Long_0GF
NEP4_300K_1e17_Fs0.220_CQ1en3_Long_0GF
```

Enter start Vg for linear fitting (V) : 0

Fig. 6.5 The UI for the threshold voltage and capacitance programs of *p*-NEP in Fig. 6.1.

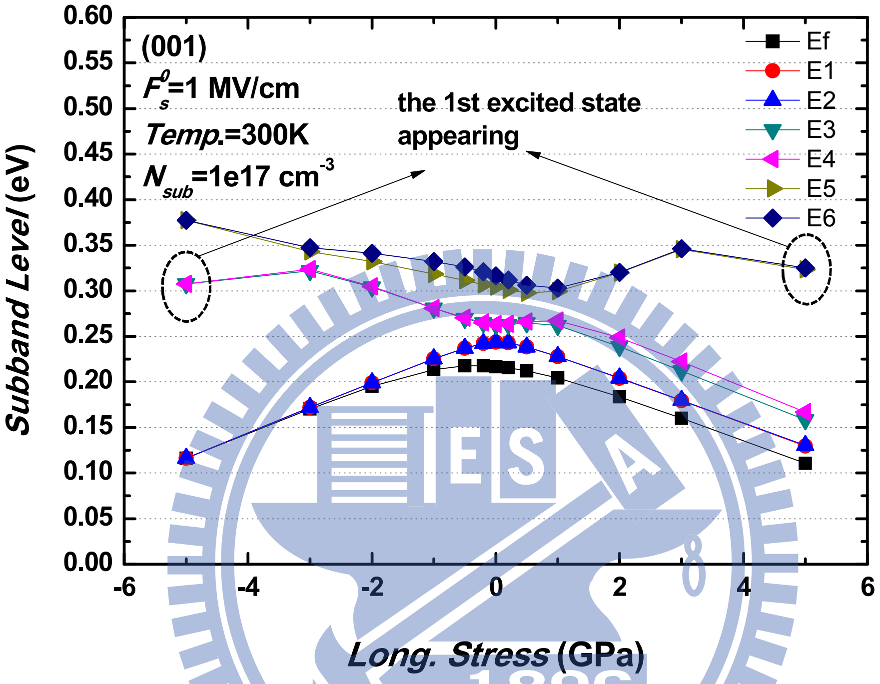

Fig. 6.6 The calculated subband levels based on the the six-band $k \cdot p$ triangular potential approximation versus the longitudinal stress in the (001) *p*-type silicon inversion layer.

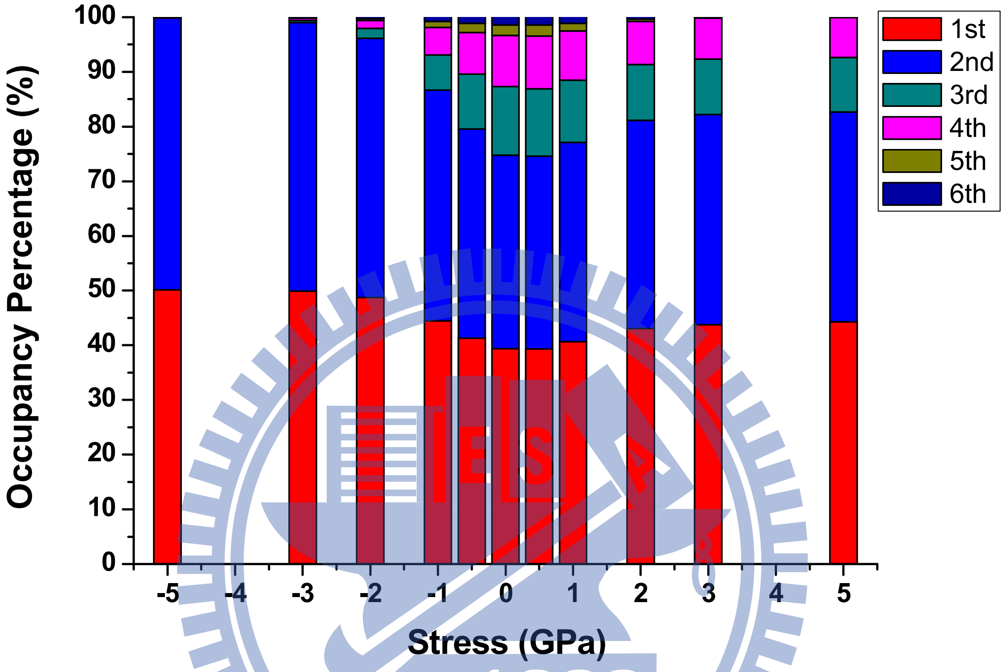

Fig. 6.7 The calculated subband occupancy based on the the six-band $k \cdot p$ triangular potential approximation versus the longitudinal stress in the (001) *p*-type silicon inversion layer. The calculation conditions are the same as in Fig. 6.6.

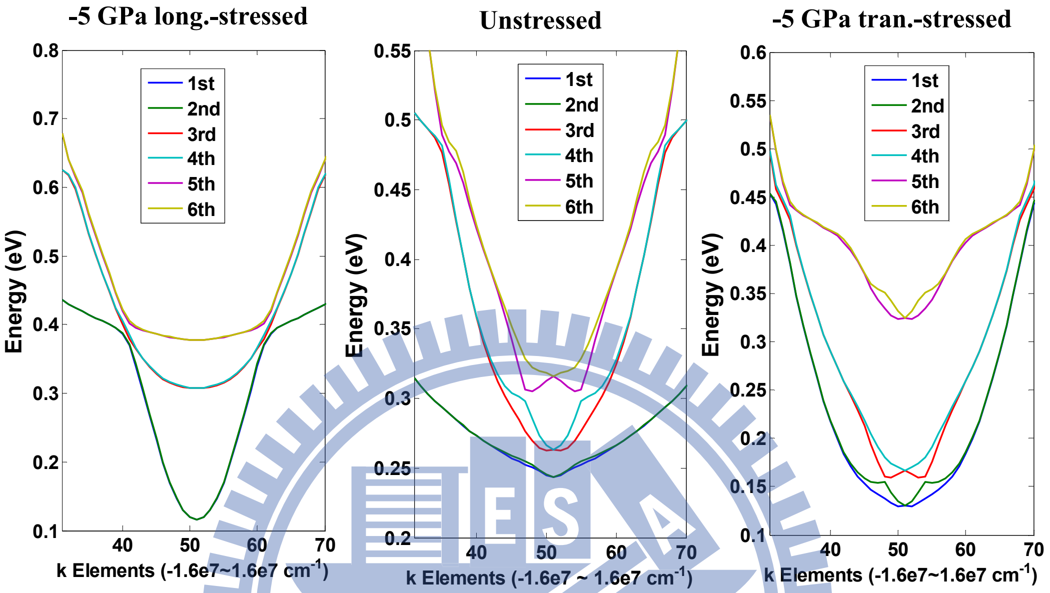

Fig. 6.8 The calculated subband structures along $k_{<110>}$ based on the the six-band $k \cdot p$ triangular potential approximation versus the longitudinal stress in the (001) *p*-type silicon inversion layer. The calculation conditions are as in Fig. 6.6.

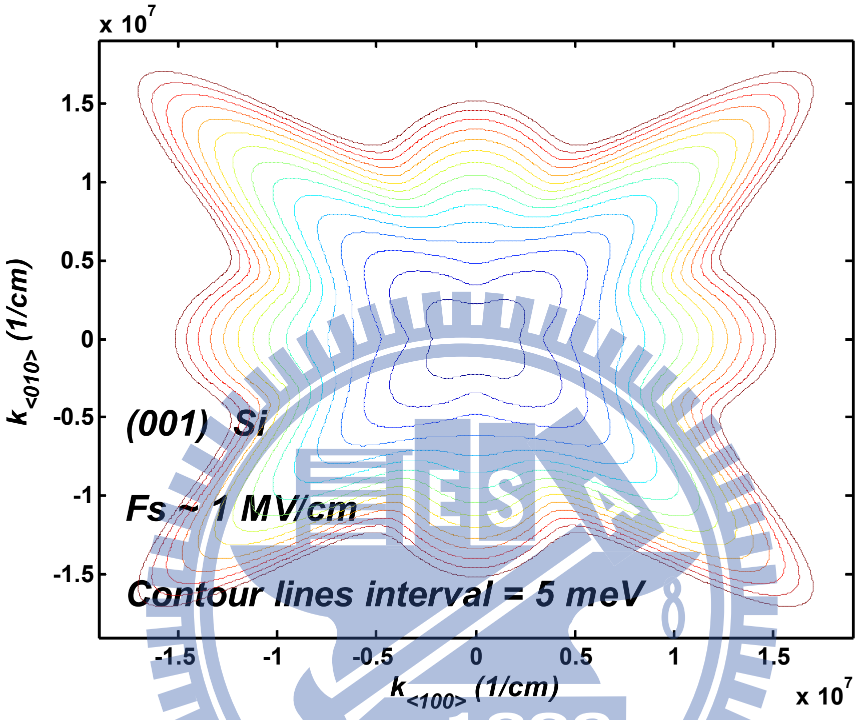

Fig. 6.9 The fully-iterated (by the six-band $k \bullet p$ Schrödinger-Poisson self-consistent method) energy contours of the first subband in (001) silicon *p*-type inversion layer.

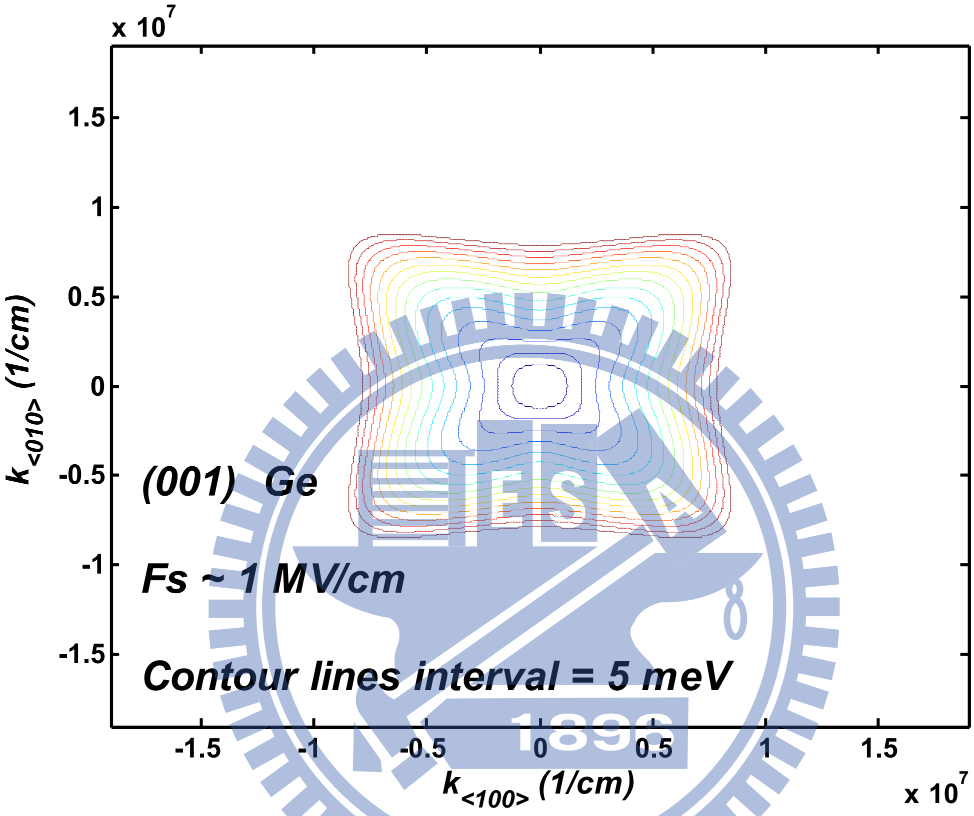

Fig. 6.10 The fully-iterated (by the six-band $k \cdot p$ Schrödinger-Poisson self-consistent method) energy contours of the first subband in (001) germanium p-type inversion layer.

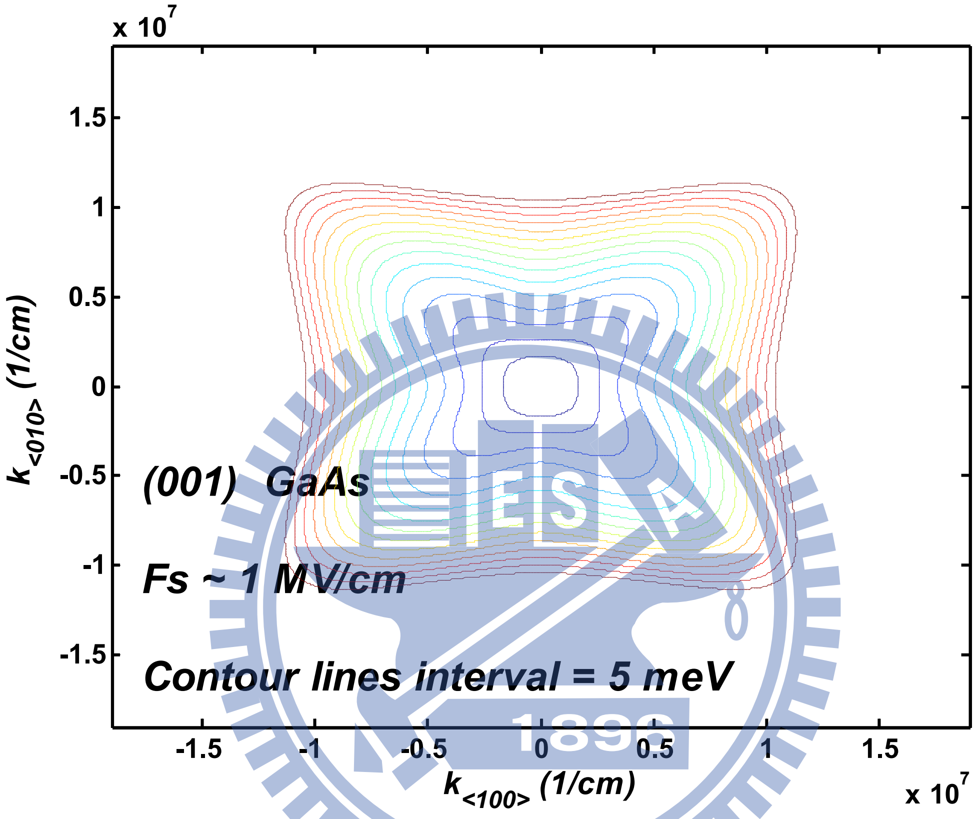

Fig. 6.11 The fully-iterated (by the six-band $k \cdot p$ Schrödinger-Poisson self-consistent method) energy contours of the first subband in (001) gallium arsenide *p*-type inversion layer.

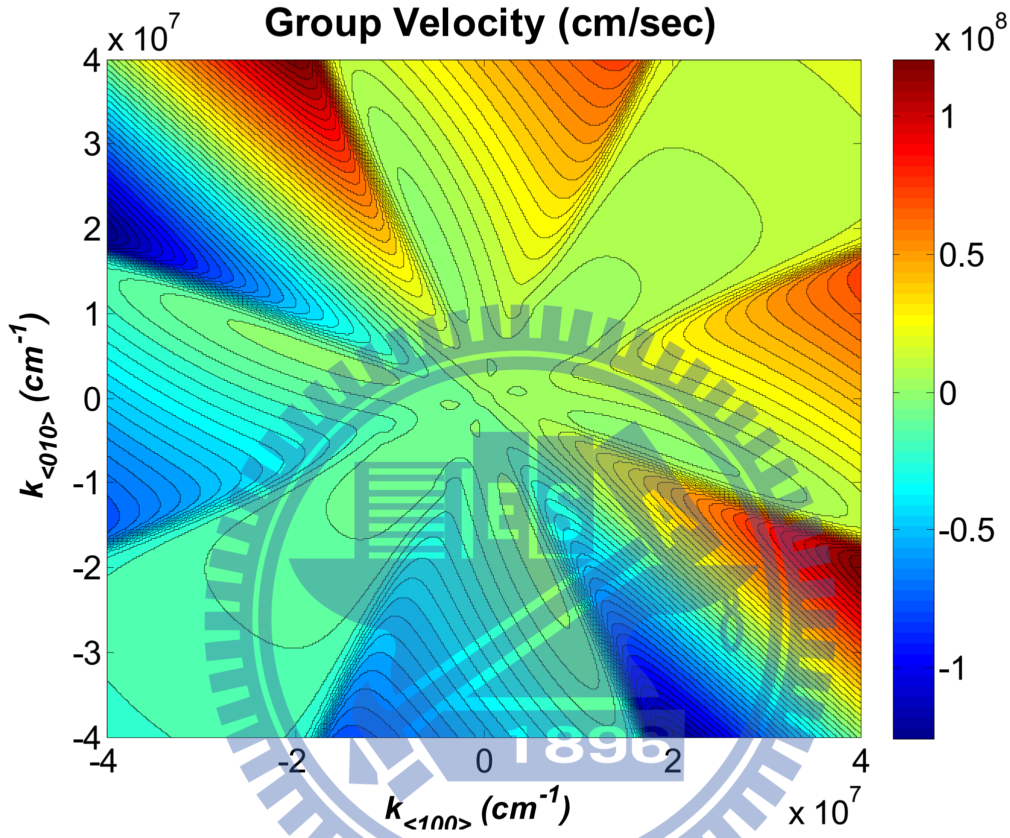

Fig. 6.12 The fully-iterated (by the six-band $k \cdot p$ Schrödinger-Poisson self-consistent method) group velocity along $k_{<110>}$ overall k-plane of the first subband in (001) silicon p-type inversion layer.

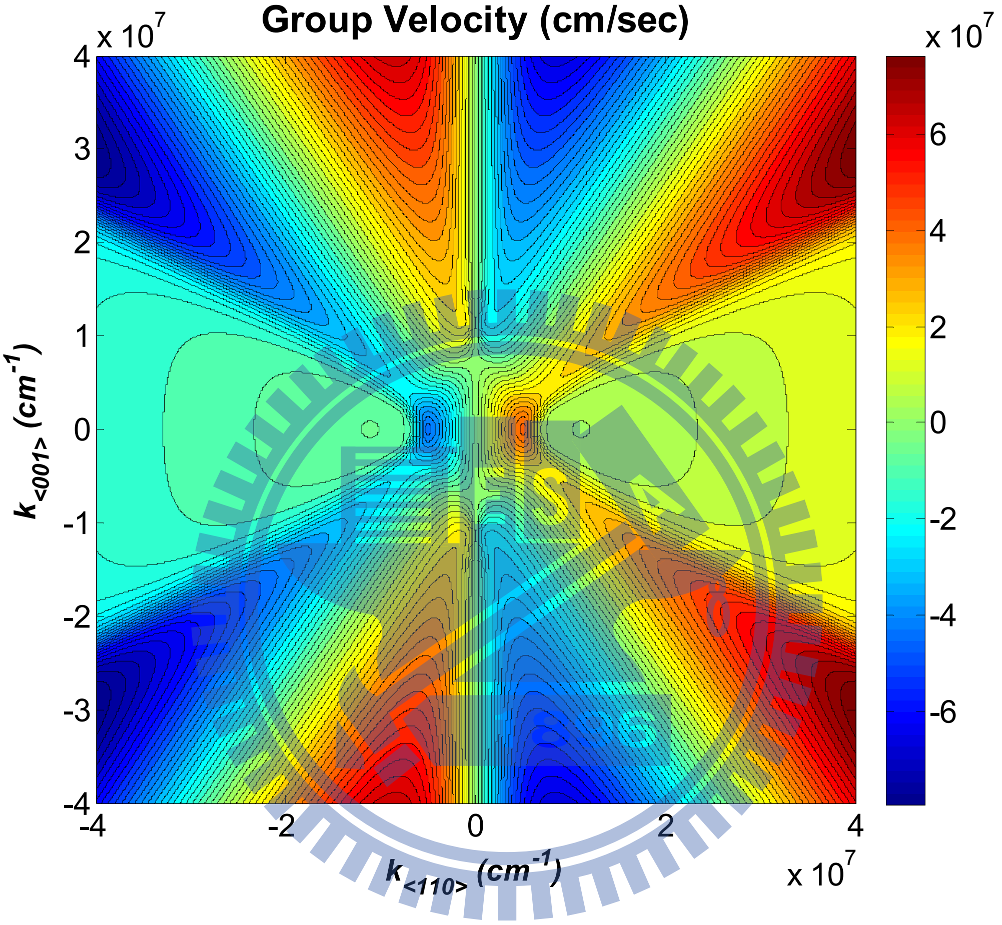

Fig. 6.13 The fully-iterated (by the six-band $k \cdot p$ Schrödinger-Poisson self-consistent method) group velocity along $k_{<110>}$ overall k-plane of the first subband in (110) silicon p-type inversion layer.

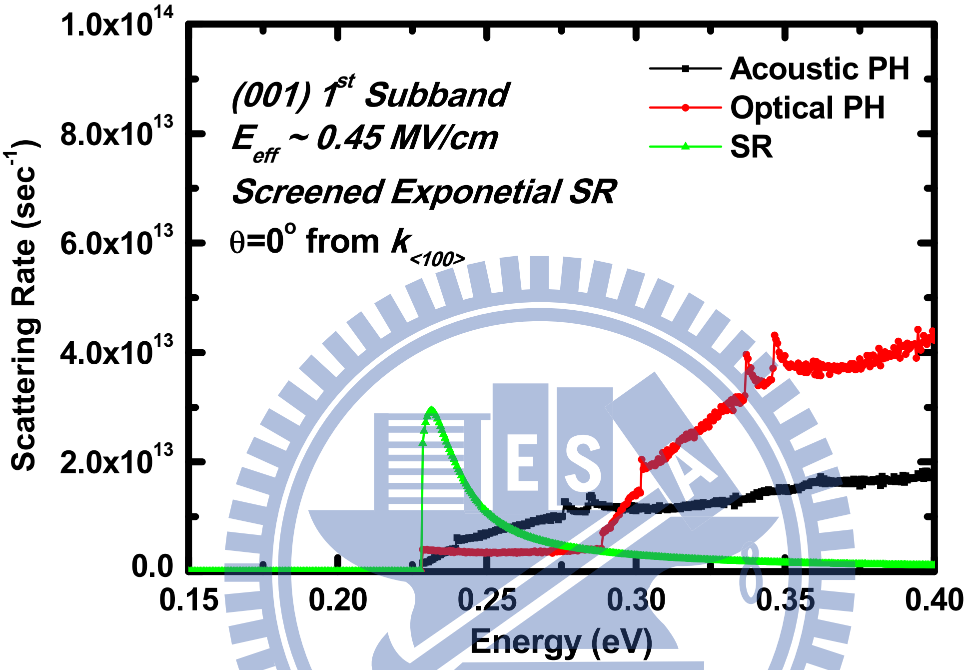

Fig. 6.14 The fully-iterated (by the six-band $k \cdot p$ Schrödinger-Poisson self-consistent method) acoustic phonon, optical phonon, and surface roughness scattering rate of the first subband in (001) silicon *p*-type inversion layer.

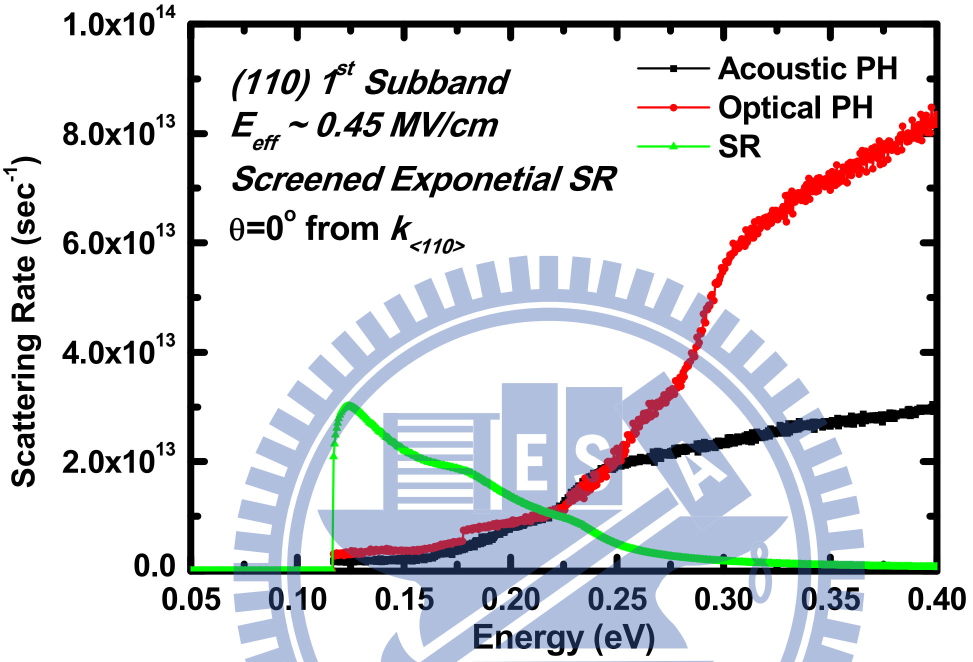

Fig. 6.15 The fully-iterated (by the six-band $k \cdot p$ Schrödinger-Poisson self-consistent method) acoustic phonon, optical phonon, and surface roughness scattering rate of the first subband in (110) silicon *p*-type inversion layer.

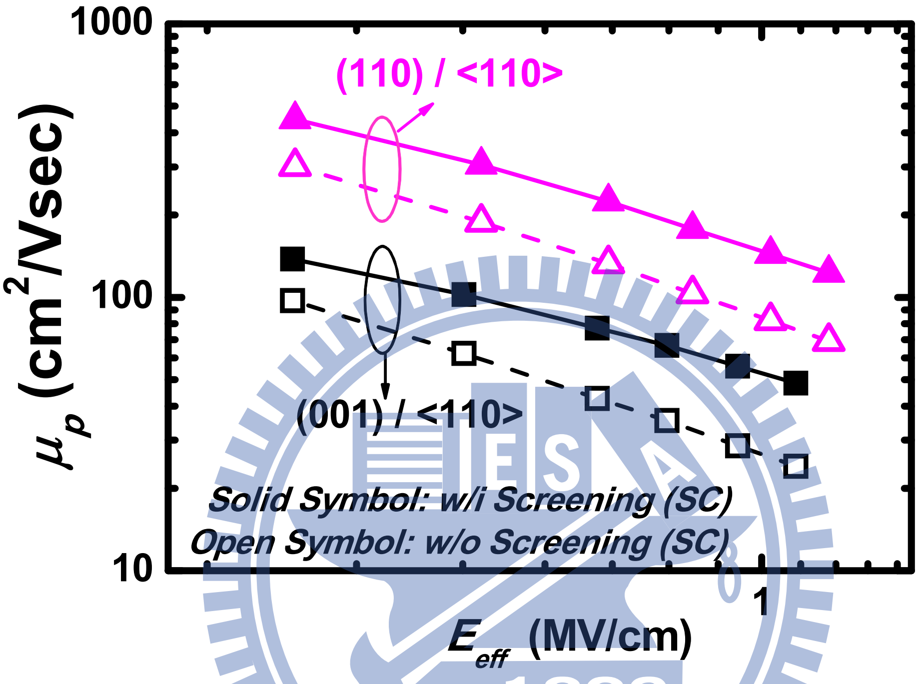

Fig. 6.16 The unstressed (001) and (110) hole inversion-layer mobility with and without screening effect with N_{sub}=1e17 cm^{-3} at Temp. =300 K.

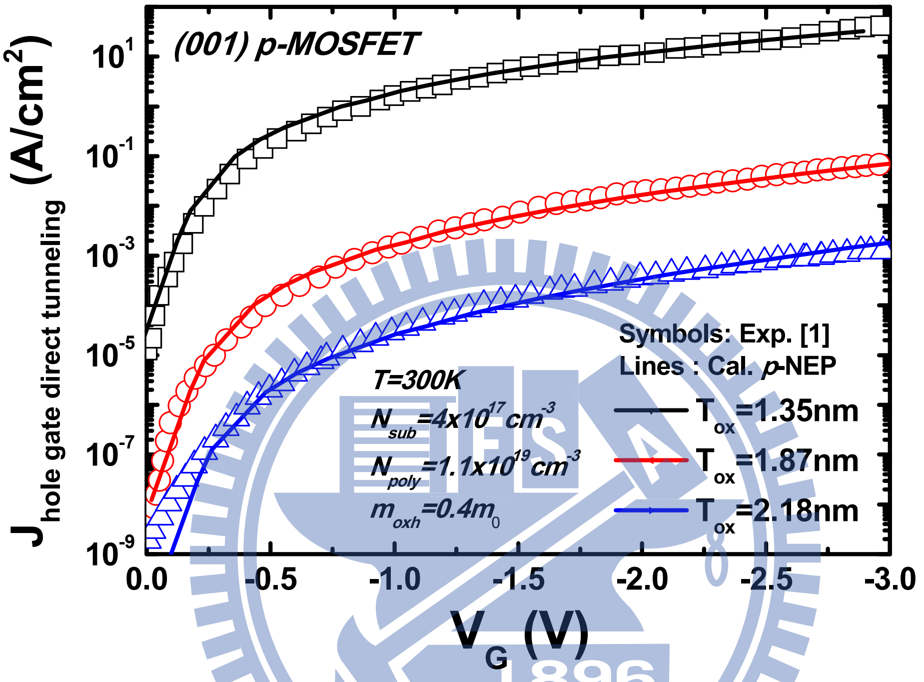

Fig. 6.17 The calculated unstressed hole gate direct tunneling current density are found in the satisfactory agreements with the experimental data of the different oxide thicknesses [1].

NO stress on the large-size poly- and FUSI-gate devices

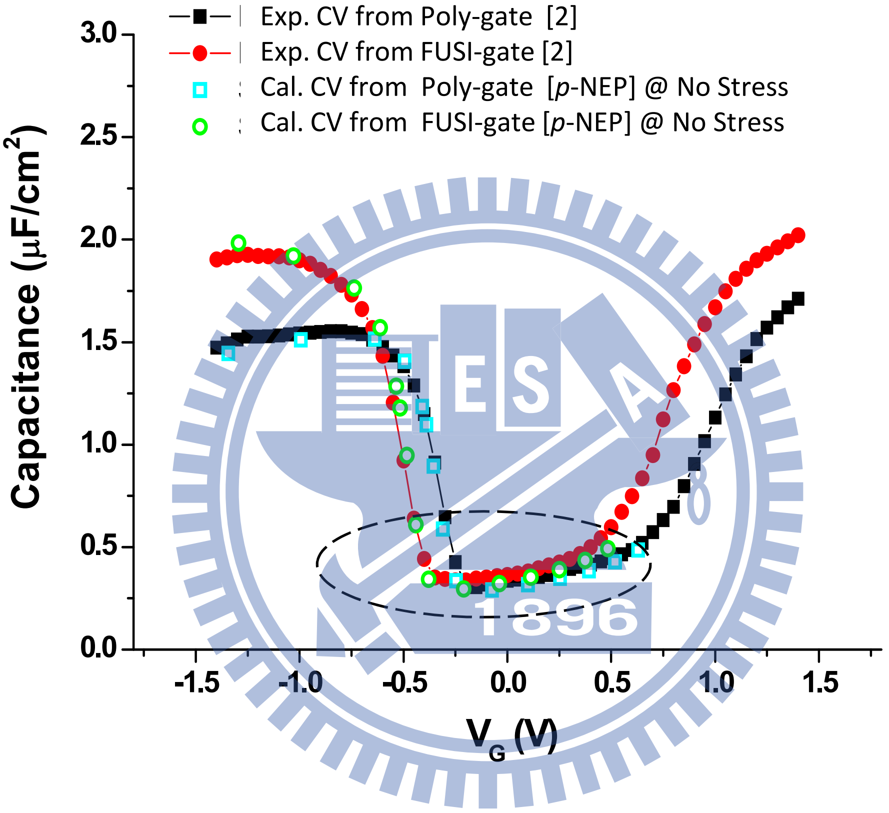

	N_{sub} (cm-3)	EOT (nm)	m_{SiON} (m0)	Barrier Height (eV)	ε_{SiON}	N_{poly} (cm-3)	Work Fuction (eV)
Poly-gate	1.6e18	1.32	0.27	3.8	5	6.5e19	5.17
FUSI-gate	1.6e18	1.32	0.27	3.8	5	na	5.013

Fig. 6.18 The unstressed capacitance versus gate voltage are compared with the experimental data from [2] where the stressor originated from the selective fully silicided (FUSI) gate.

-460 MPa stress on the large-size FUSI-gate device

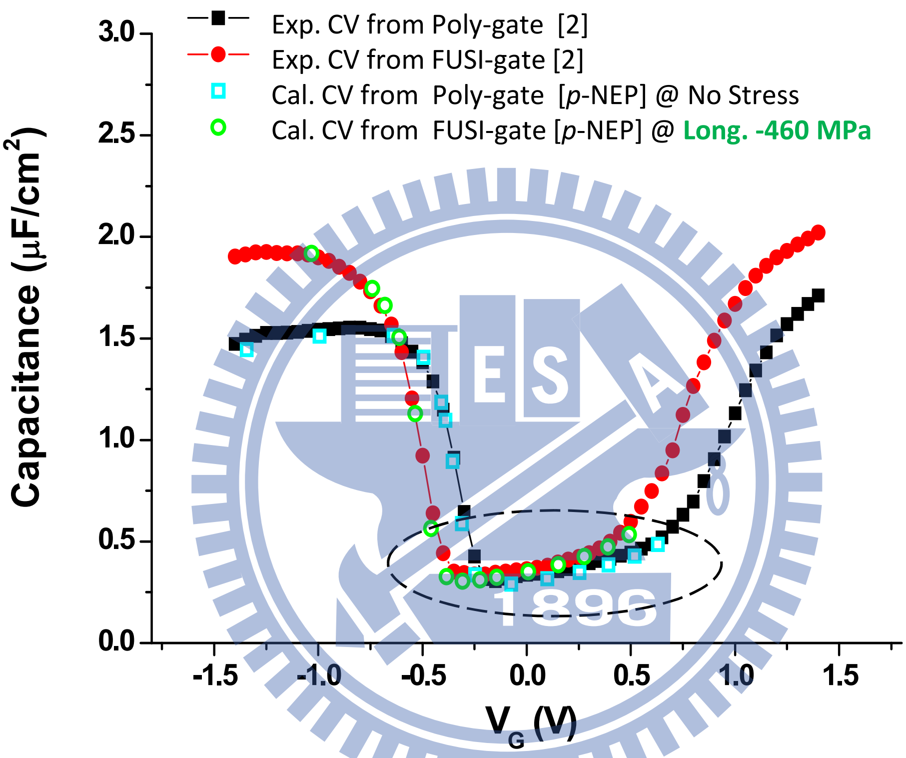

	N_{sub} (cm-3)	EOT (nm)	m_{SiON} (m0)	Barrier Height (eV)	ε_{SiON}	N_{poly} (cm-3)	Work Fuction (eV)
Poly-gate	1.6e18	1.32	0.27	3.8	5	6.5e19	5.17
FUSI-gate	1.6e18	1.32	0.27	3.8	5	na	5.013

Fig. 6.19 The stressed capacitance versus gate voltage are compared with the experimental data from [2] where the stressor originated from the selective fully silicided (FUSI) gate.

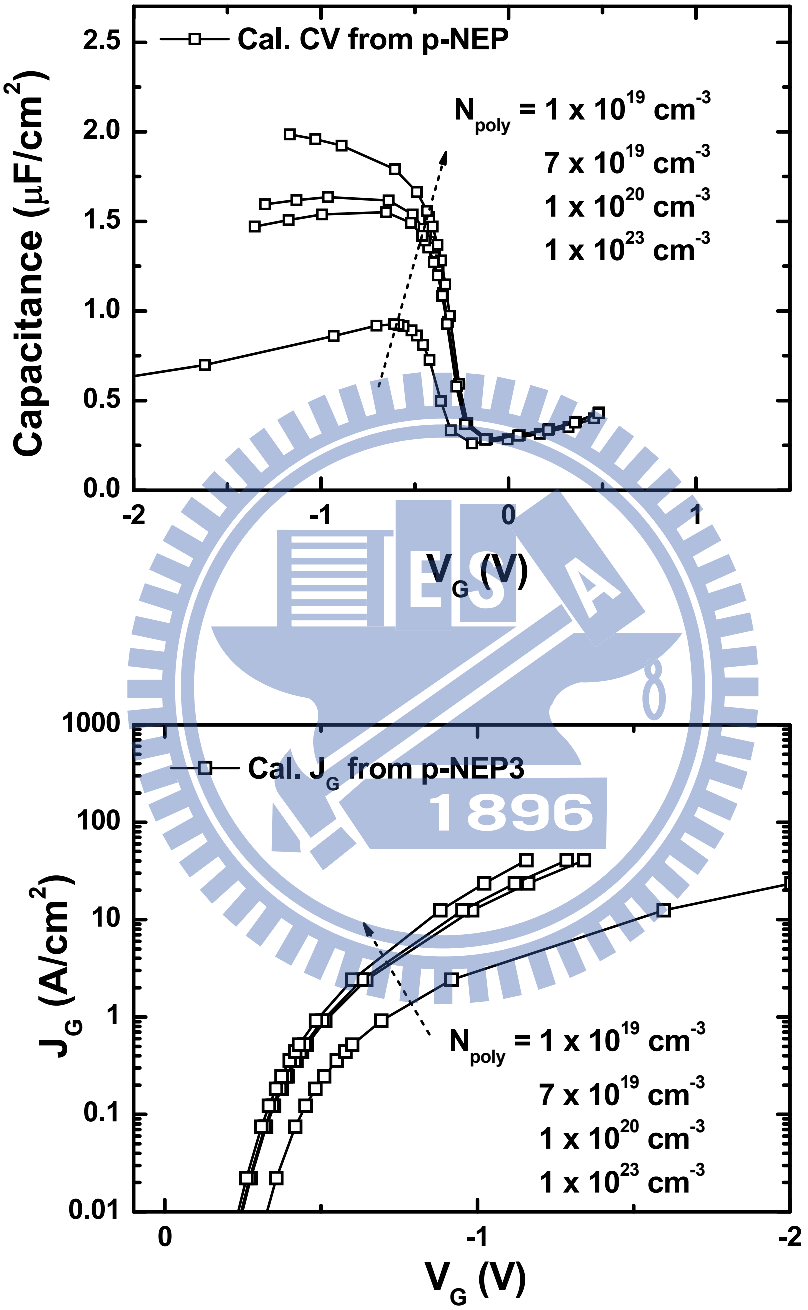

Fig. 6.20 The calculated hole gate direct tunneling current density and capacitance are drawn simultaneously with the varying poly-gate doping concentrations. The other parameters came from the table (poly-gate) in Fig. 6.19.

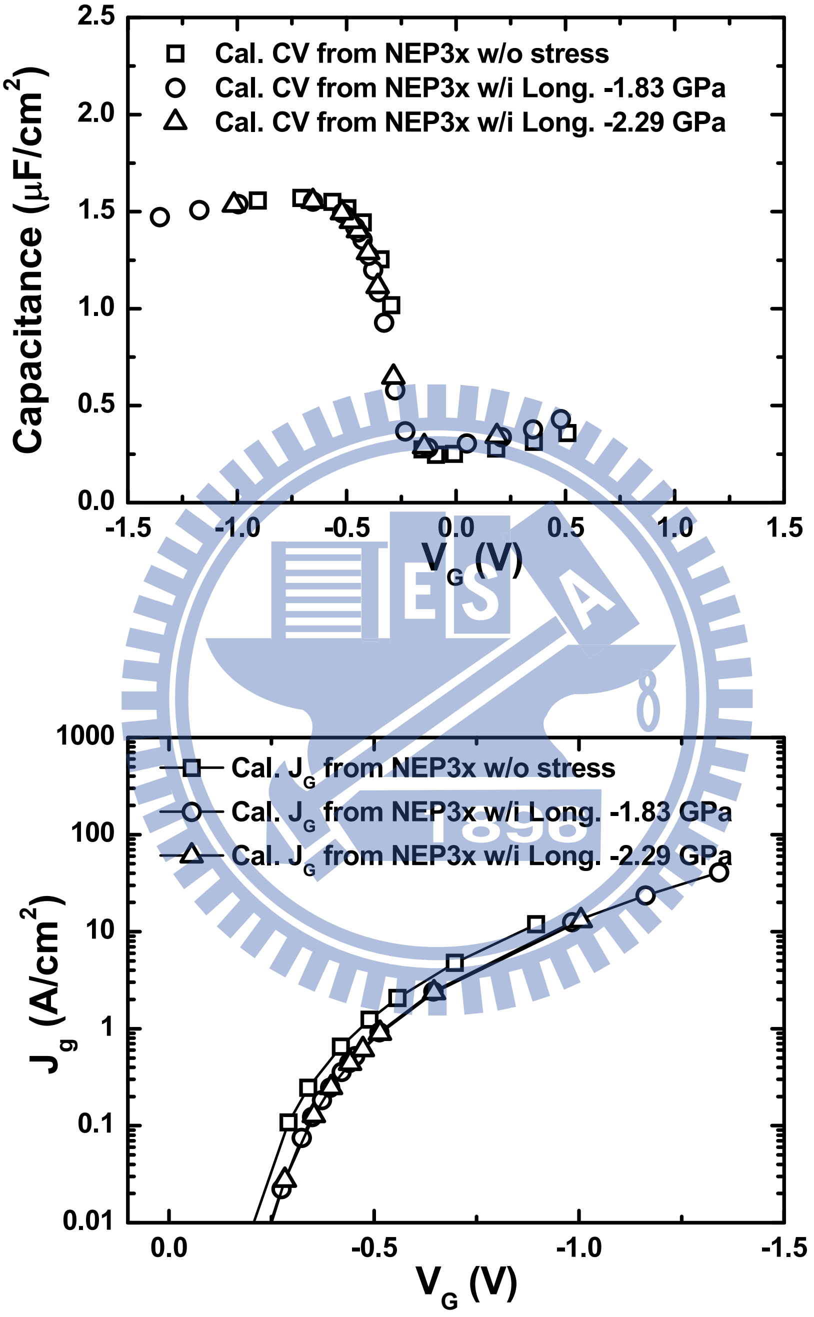

Fig. 6.21 The calculated hole gate direct tunneling current density and capacitance are drawn simultaneously with the varying stress conditions. The other parameters came from the table (poly-gate) in Fig. 6.19.

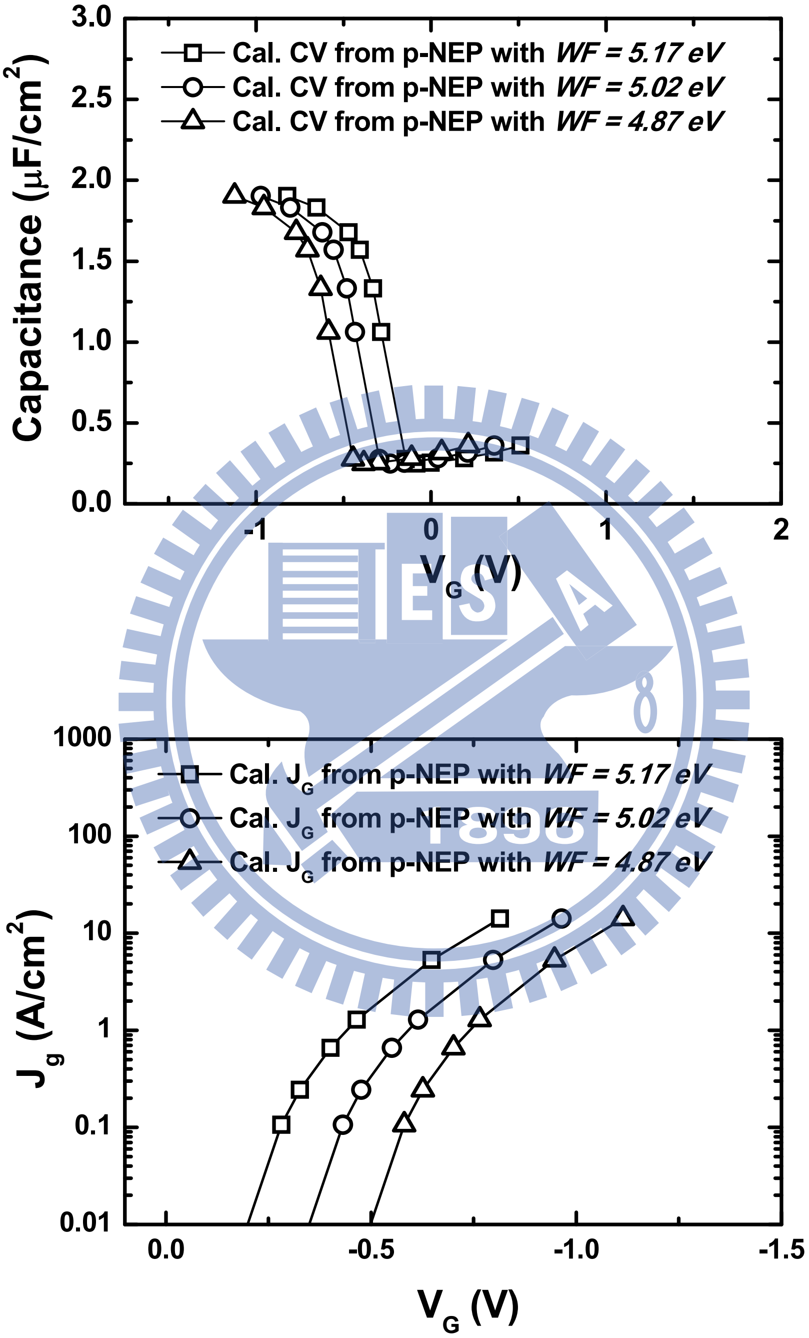

Fig. 6.22 The calculated hole gate direct tunneling current density and capacitance are drawn simultaneously with the varying metal-gate work functions. The other parameters came from the table (FUSI-gate) in Fig. 6.19.

Chapter 7

Conclusions

The dissertation demonstrates the study of the hole electrical properties in silicon inversion layer in presence of both the the significant quantum confinement and the complicated mechanical stresses. Conclusions of this work are described as below:

- We have successfully constructed the simulator *p*-NEP which can deal with the hole electrical properties in silicon inversion layer beneath in the presence of the significant quantum confinement and the complicated mechanical stresses. It is also a flexible simulator covering the alternative materials (silicon, germanium, gallium arsenide), the alternative wafer orientations ((001), (110), (111)), the alternative temperature conditions (2K~400K), the alternative stress conditions (GPa-level uniaxial, biaxial stresses), and the alternative substrate doping concentrations (1e15~6e18 cm^{-3}).

- We have constructed a new computational accelerator based on a hole effective mass approximation with aim to intrinsically boost a self-consistent six-band $k \cdot p$ simulation. First of all, a triangular potential based six-band $k \cdot p$

simulation has been performed to produce hole quantization and density-of-states effective masses. Then with those hole effective masses as input, an *EMA oriented Schrödinger-Poisson iterative solving in pMOSFETs* has been executed as rapidly as the electron counterparts. The resulting confining electrostatic potential profile has been proved to match the realistic one, thus ensuring a fast convergence in the subsequent self-consistent six-band $k \cdot p$ simulation. This remains valid for different temperatures, different substrate doping concentrations, different inversion hole densities, and different surface orientations. We have found that the overall CPU time is substantially reduced down to around 8% to 17% of that without the use of the proposed accelerator. The validity of the chosen convergence criteria has been verified. The simulated results have been validated by the published ones obtained from the conventional self-consistent six-band $k \cdot p$ method alone. The application of the proposed accelerator to more general applications has been projected.

- Three published sets of bulk oriented Luttinger parameters have been successfully examined by finding out the possible agreements with the direct experimental results of Takahashi, et al. The *realistic* subband structures have been constructed by the these results. The comparisons Hole mobility and DOS effective masses have been clearly demonstrated in (110) p-MOSFETs at 2 K.

- It has been found that the phonon-limited mobility change is more stress-sensitive than the surface-roughness-limited one, and the mobility change ratio can be reversely proportional to the conductivity effective mass and density-of-states effective mass only in the absence of the surface roughness-limited mobility change. Individual contributions of hole mobility change have all be quantified. Calculated hole mobility change due to varying a_υ, b, and d has been created and has accounted for 3-D uniaxial stress conditions. The primary factor d and the secondary factor b have been drawn. Guidelines have been established, followed by the experimental determination of a_υ, b, and d. The literature errors of the Bir-Pikus deformation potentials have therefore been improved.

博士候選人學經歷表

Personal Data:

Name: Chien-Chih Lee
Date of birth: 21th November, 1981
Nationality: Taiwan, ROC
Affiliation: Department of Electronics Engineering, National Chiao Tung University
Address: Engineering Building 4, 1001 University Road, Hsinchu, Taiwan 300, ROC
Phone: 886-3-571-2121#54217
E-mail: cclee.ee93g@g2.nctu.edu.tw

Education:

- *2006-now* Ph.D student, Department of Electronics Engineering, National Chiao Tung University, Hsinchu, Taiwan, ROC (advisor: Prof. Ming-Jer Chen)
- *2004-2006* M.S., Department of Electronics Engineering, National Chiao Tung University, Hsinchu, Taiwan, ROC (advisor: Prof. Ming-Jer Chen)
- *2000-2004* B.S., Department of Physics, National Chung Hsin University, Taichung, Taiwan, ROC

Teaching and Researching Experiences:

1. Research on graphene fabrication in Friedrich-Alexander Universität Erlangen-Nürnberg, Germany (*2010-2011 DAAD Sandwich Program*).
2. Taiwan Semiconductor Manufacturing Company (TSMC) 2010 University JDP Program: *A Fast Quantum Strain Simulator to Enable Engineering Applications in Bulk Planar MOSFETs and Multi-gate Vertical MOSFETs*
3. Taiwan Semiconductor Manufacturing Company (TSMC) 2009 University JDP Program: *Examination of 3-D Stress Effect on p-MOSFET Hole Transport by a Six-Band k・p Method*
4. Taiwan Semiconductor Manufacturing Company (TSMC) 2007 University JDP Program: *Examination of Three Key Issues in Nano-CMOS Strain Engineering: Anisotropic Diffusion, Lattice Mismatch, and Oxide Thinning*
5. T.A. of "Low-Dimension Nanodevice Transport Theory and Computational Tools", 2009

6. T.A. of “Noise and Fluctuations”, *2007-now*
7. T.A. of “Semiconductor Device Physics”, *2004-2006*

Publication List

1. Ming-Jer Chen, **Chien-Chih Lee**, and Ming-Pei Lu, “Probing a nonuniform two-dimensional electron gas with random telegraph signals,” *Journal of Applied Physics*, vol. **103**, p. 034511, February 2008.

2. Chih-Yu Hsu, **Chien-Chih Lee**, Yi-Tang Lin, Chen-Yu Hsieh, and M. J. Chen, “Enhanced hole gate direct tunneling current in process-induced uniaxial compressive stress p-MOSFETs,” *IEEE Trans. Electron Devices*, vol. **56**, pp. 1667-1673, August 2009.

3. Chih-Yu Hsu, Hua-Gang Chang, Shin-Jiun Kuang, Wei-Han Lee, Yu-Cheng Chen, **Chien-Chih Lee**, and Ming-Jer Chen, “Enhanced hole mobility in non-(001) oriented sidewall corner of Si pMOSFETs formed on (001) substrate,” *IEEE Silicon Nanoelectronics Workshop*, pp. 67-68, June 2010 (Honolulu).

4. Ming-Jer Chen, **Chien-Chih Lee**, and Kuan-Hao Cheng, “Hole effective masses as a booster of self-consistent six-band k • p simulation in inversion layers of pMOSFETs,” *IEEE Trans. Electron Devices*, vol. **58**, pp. 931-937, Apr. 2011.

5. Ming-Jer Chen, Sou-Chi Chang, Shin-Jiun Kuang, **Chien-Chih Lee**, Wei-Han Lee, Kuan-Hao Cheng, Yi-Hsien Zhan, “Temperature dependent remote-Coulomb-limited electron mobility in n$^+$-polysilicon ultrathin gate oxide nMOSFETs” *IEEE Trans. Electron Devices*, vol. **58**, pp. 1038-1044, Apr. 2011.

6. Ming-Jer Chen, Li-Ming Chang, Shin-Jiun Kuang, Chih-Wei Lee, Shang-Hsun Hsieh, Chi-An Wang, Sou-Chi Chang, and **Chien-Chih Lee**, “Temperature-oriented mobility measurement and simulation to assess surface roughness in ultrathin-gate-oxide (1 nm) nMOSFETs and its TEM evidence” *IEEE Trans. Electron Devices*, vol. **59**, pp. 949-955, Apr. 2012.

7. Ming-Jer Chen, **Chien-Chih Lee**, and Wan-Li Chen, “Effect of Strained k • p

Deformation Potentials on Hole Inversion-Layer Mobility," *IEEE Trans. Electron Devices*, submitted.